Achieving Sub-10-nm Resolution using Scanning Electron Beam Lithography

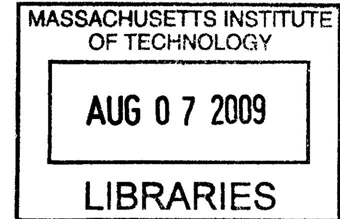
MASSACHUSETTS INSTITUTE OF TECHNOLOGY
AUG 0 7 2009
LIBRARIES

by

Bryan M. Cord

Submitted to the Department of Electrical Engineering and Computer Science

in partial fulfillment of the requirements for the degree of

Doctor of Philosophy in Electrical Engineering and Computer Science

at the

MASSACHUSETTS INSTITUTE OF TECHNOLOGY

June 2009

© Massachusetts Institute of Technology 2009. All rights reserved.

ARCHIVES

Author ....
Bryan M. Cord
Department of Electrical Engineering and Computer Science
May, 2009

Certified by ....
Karl K. Berggren
Associate Professor of Electrical Engineering and Computer Science
Thesis Supervisor

Accepted by ....
Terry P. Orlando
Chair, Department Committee on Graduate Students

Abstract

Achieving the highest possible resolution using scanning-electron-beam lithography (SEBL) has become an increasingly urgent problem in recent years, as advances in various nanotechnology applications have driven demand for feature sizes well into the sub-10-nm domain. While SEBL has the highest resolution of nearly any conventional patterning technique available, reliably defining features at these length scales has been a challenge, as well as an interesting scientific problem.

In this work I have investigated, both theoretically and experimentally, many of the factors that limit SEBL resolution and attempted to understand and minimize their influence on the process. This includes resist development, where we have thoroughly characterized the temperature dependence of poly(methylmethacrylate) (PMMA) resist contrast and used the results to create transferable patterns smaller than nearly any published results to date with this resist chemistry. We have also examined the process of electron-beam exposure and attempted to characterize the various factors that affect the way energy is distributed in the resist by the beam, using theoretical arguments, Monte Carlo simulations, and experimental data. We have used the results of these investigations to create some of the smallest structures reported to date, using hydrogen silsesquioxane (HSQ) resist. Finally, we have applied some of the previously-gained knowledge to the design of a unique bilayer process for patterning high-resolution metal structures using evaporation and liftoff, while simultaneously developing a broadly-useful new model for the kinetics of resist development.

Acknowledgements

This thesis never would have happened without the contributions of the following people, all of whom I feel extremely lucky to have had the opportunity to work with:

Professor Karl Berggren, for supervising my thesis work for the last five years and providing me with much-needed direction and motivation.

Professors Caroline A. Ross and Henry I. Smith, for agreeing to serve on my thesis committee and taking the time to read and give me very constructive feedback on this document.

Dr. Joel Yang, for his endless insights on how to make very small things, his ability to work miracles with an electron beam, and for being a great friend and labmate.

Dr. Huigao Duan, for his transmission electron microscopy expertise and willingness to help me out on very short notice.

Dr. Jodie Lutkenhaus, for always being a phone call or email away when I had a question about polymer or resist chemistry.

Dr. Chris Dames, for his help with constructing the resist-development model in chapter 4.

Dr. José Aumentado for designing, and then sharing with me, the original process that led to the work in chapter 4.

Professor David C. Joy, for his insights and assistance in programming the Monte Carlo simulation used in chapter 3, as well as providing the original code it was based on.

Jim Daley, for keeping the NanoStructures Lab running as well as it does, and for helping me fix countless processing problems.

Mark Mondol, for keeping MIT's scanning electron beam lithography facility running smoothly against impossible odds, and also for helping me with all kinds of SEBL work over the years.

Tiffany Kuhn, for being an excellent secretary and for putting up with my frequent and varied last-minute emergencies.

All the other students and staff in the Nanostructures Laboratory, who have always been willing to help me out with random fabrication problems or questions.

Last but obviously not least Kathleen, both for not strangling me at any point while I was writing this thing and agreeing to marry me next month.

Table of Contents

1 Introduction 1

1.1 Scanning-Electron-Beam Lithography 1

1.1.1 Description 2

1.1.2 Background and History 2

1.2 Motivation for This Work 5

1.3 Thesis Overview 8

2 Optimizing PMMA Contrast via Control of Development Temperature 9

2.1 Resist Contrast 9

2.1.1 Contrast Enhancement 12

2.2 Cold Development 17

2.2.1 History 18

2.2.2 Mechanism 18

2.3 Contrast Experiments 22

2.3.1 Description 23

2.3.2 Results 28

2.3.3 Discussion 34

2.3.3.1 Scission 34

2.3.3.2 Crosslinking 38

2.4 Resolution Experiments 41

2.4.1 Description 41

2.4.2 Results 43

2.5 Conclusion 45

3 Control and Optimization of SEBL Exposure 47

3.1 Motivation 47

3.1.1 Effect of Exposure Parameters on Resolution 47

3.1.2 Limits of Contrast Enhancement 50

3.2 The Point-Spread Function 52

3.2.1 Primary Beam Scattering 52

3.2.2 Beam Diameter and Secondary Electrons 56

3.3 Monte Carlo Simulation 59

3.3.1 Description 59

3.3.2 Results 63

3.4 Experimental Verification 70

3.4.1 Description 70

3.4.2 Results 72

3.5 Beam Diameter Measurement 77

3.5.1 Procedure 77

3.5.2 Results 79

3.6 Imaging Limitations 81

3.6.1 TEM Analysis 83

3.6.1.1 Sample Preparation 83

3.6.1.2 Results 86

3.7 HSQ Development 88

3.7.1 Development Rate 88

3.7.2 Diffusion-Limited Development....90
3.7.3 Experimental Verification....94
3.8 Conclusion and Further Work....97
4 High-Resolution Liftoff Patterning with a Lithographically-Defined Bilayer....101
4.1 Electron-Beam Evaporation....101
4.2 Suspended Shadow-Mask Evaporation....103
4.2.1 Process Overview....103
4.2.2 Bilayer Fabrication....105
4.2.2.1 Overview....105
4.2.2.2 Copolymer Method....105
4.2.2.3 Poly(methylglutarimide) (PMGI) Method....108
4.2.3 Lithographic Undercut Control....109
4.3 Exposure Modeling....113
4.3.1 Description....113
4.3.2 Results....115
4.4 Experimental Verification....117
4.4.1 Procedure....117
4.4.2 Results....117
4.4.3 Undercut Saturation....119
4.5 Development Modeling....120
4.5.1 Model Description....121
4.5.2 Derivation of Undercut Relationship....123
4.5.3 Model Results....127

4.6 Applications and Conclusion 129

5 Conclusion 134

5.1 Resist Processing Limitations 134

5.1.1 PMMA 135

5.1.2 HSQ 136

5.2 Metrology Limitations 138

5.3 Summary 138

5.4 Further Work 140

Appendix A Monte Carlo Source Code 141

A.1 Interface 141

A.2 Source Code 145

A.2.1 Global Variable Declaration 146

A.2.2 The XYZ Data Type 148

A.2.3 Main Program Loop 149

A.2.4 Secondary Electron Tracking 158

References 165

Chapter 1: Introduction and Overview

Since its inception, the semiconductor industry has been marked by a constant demand for better, more high-resolution ways of patterning devices. Moore's Law, which states that the number of transistors that can be practically placed on an integrated circuit will double every two years,[1] has driven decades of relentless improvement of lithographic technologies. As resolution demands begin to approach the scale of atoms and molecules, long-dominant technologies such as optical projection lithography are proving increasingly difficult to improve further. Scanning-electron-beam lithography (SEBL), a low-throughput technology capable of much higher resolution than any current photon-based scheme, may hold the key to enabling the next generation of mainstream lithographic technologies. In this work, we seek to understand the capabilities and limits of modern SEBL processing, from both a theoretical, scientific point of view and in the context of several different applications.

1.1 Scanning Electron Beam Lithography

Scanning-electron-beam lithography has existed nearly as long as the semiconductor industry itself. Its extremely high resolution (the highest of any practical lithographic technology) has made it invaluable for photomask manufacture, research work, and other applications, but its inherently low throughput has kept it from replacing lower-resolution optical projection lithography in large-scale manufacturing settings. Still, SEBL may represent the key bridge between current and next-generation lithographic technologies.

1.1.1 Description

Scanning-electron-beam lithography is a process that, since its invention nearly four decades ago,[2-10] remains one of the highest-resolution methods of top-down nanopatterning available. Steady improvement of SEBL tools and processes over the years has led to current state-of-the-art systems capable of producing structures on the order of 10 nm wide[11-16]—more than a factor of four better than even the most cutting-edge photon-based lithography. While throughput limitations have kept SEBL from being used in high-volume manufacturing by the semiconductor industry, it remains a key technology for mask-making, research, application-specific integrated circuit (ASIC) manufacture, and other applications where resolution is critical and throughput is not a major issue.

1.1.2 Background and History

SEBL is a relatively self-explanatory technology—a tightly focused beam of electrons is scanned across a sample coated with some type of electron-sensitive material. By switching the beam on and off and controlling its speed and direction, patterns can be formed in the material. The technology has its roots in scanning electron microscopy (SEM), and was inspired by the fact that a SEM 1) is capable of much higher resolution than any optical microscope, and 2) can damage certain types of samples under inspection if the beam is focused on them for too long. The first SEBL systems were

simply electron microscopes, reprogrammed to generate simple shapes, like lines, instead of the standard raster-scan display used for imaging.[7,8]

The results of these early SEBL experiments were extremely promising, and dedicated SEBL systems with hardware-based beam controllers eventually took the place of the software-controlled, "hacked SEM" systems used in the earliest experiments, as shown in figure 1-1.[17-19] At the same time, considerable effort was being expended toward discovering high-resolution electron resists to complement the new technology.[3-5,9,10,20-23] While many types of resist were investigated, poly(methylmethacrylate) (PMMA), quickly became (and remains today) the most commonly-used due to its high resolution, chemical stability, and versatility.[24-26] Being the dominant resist, PMMA was extensively characterized, and its exposure and development mechanisms remain among the most well-understood of any high-resolution resist currently available.[27-33]

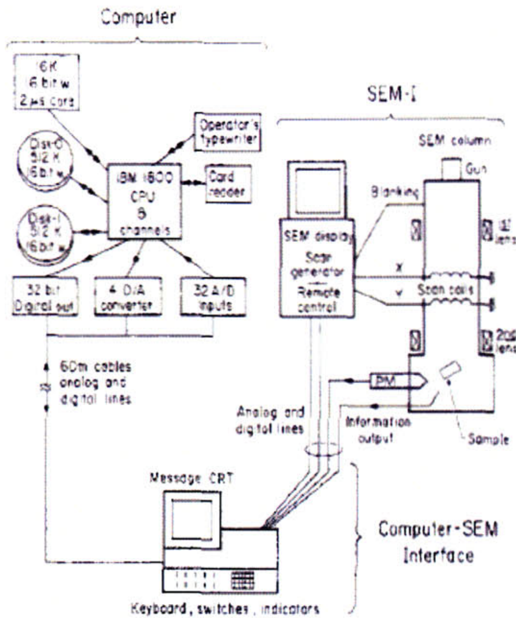

Figure 1-1: The evolution of scanning electron beam lithography tools. Left: Block diagram of an early custom-built SEBL system used by Herzog et al in their 1971 paper.[7] Right: The Vistec VB300, a modern, production-grade dedicated SEBL tool. (Photo courtesy Vistec, Inc.)

As the scanning electron microscopy state of the art improved through the years, SEBL improved along with it. Better tools, with more tightly-focused beams, faster and more accurate pattern generators, and higher acceleration voltages became available, and the resolution of the technology improved accordingly. At the same time, theoretical and experimental work was being done to try to fully understand the fundamentals of electron-resist interaction[4-6,21,23,28,30,34-41] and, in the process, determine whether this progress would continue indefinitely or if some ultimate factor would set a final resolution limit for SEBL.[32,42,43]

1.2 Motivation for This Work

Modern, state-of-the-art SEBL systems are capable of fabricating structures on the order of 10 nanometers wide. While this length scale is extremely small and far beyond what any practical top-down lithographic process can achieve, recent applications demand even better patterning capability.

Nanoimprint lithography, schematically diagrammed in figure 1-2, is a promising next-generation technology for large-scale semiconductor fabrication, as patterning structures smaller than about 25 nm using conventional optical projection lithography (OPL) has proven increasingly difficult. The logical technology to fabricate the imprint masters is SEBL—by quickly replicating a single SEBL-fabricated master mold many times, imprint lithography retains the key strength (high resolution) of SEBL while avoiding the throughput issues that are its key weakness in large-scale production applications.

While the semiconductor industry has been using SEBL-generated photomasks for optical projection lithography in much the same way for decades, the analogy between optical projection and nanoimprint lithography is imperfect for several reasons. Unlike conventional optical projection lithography systems, which typically use a lens to reduce the pattern on the photomask by ~4× before printing the final pattern, nanoimprint lithography requires the features on the master mold to be the same size as the features on the final pattern. This means that the success of nanoimprint lithography is directly tied to the resolution capabilities of electron-beam lithography—if nanoimprint is going to be

proven to be demonstrably better than optical projection lithography, it requires SEBL technology capable of manufacturing master patterns with critical dimensions of 10 nm and smaller.

Figure 1-2: Schematic illustration of nanoimprint lithography. A master mold is stamped into some type of soft material, transferring the pattern on the mold into the material. For obvious reasons, the image-reduction methods that simplify mask-making in optical projection lithography are inapplicable here..

A less immediately practical, though potentially more far-reaching, application of high-resolution SEBL is templated self-assembly. As nanotechological applications call for complex structures with smaller and smaller critical dimensions, it makes increasing sense to fabricate structures "from the bottom up"—that is, by co-opting natural self-organization and self-assembly processes to assemble structures from their component parts—rather than with "top down" technologies such as lithography. Templated self-assembly—the process of using physical and/or chemical "templates" to force very small structures into useful, orderly patterns—is a fundamental first step in this direction. Our group and others have had some recent success, some results of which are shown in

figure 1-3, in templating block copolymers (BCPs)[44-48] and sub-10-nm semiconducting quantum dots, to name just two examples.

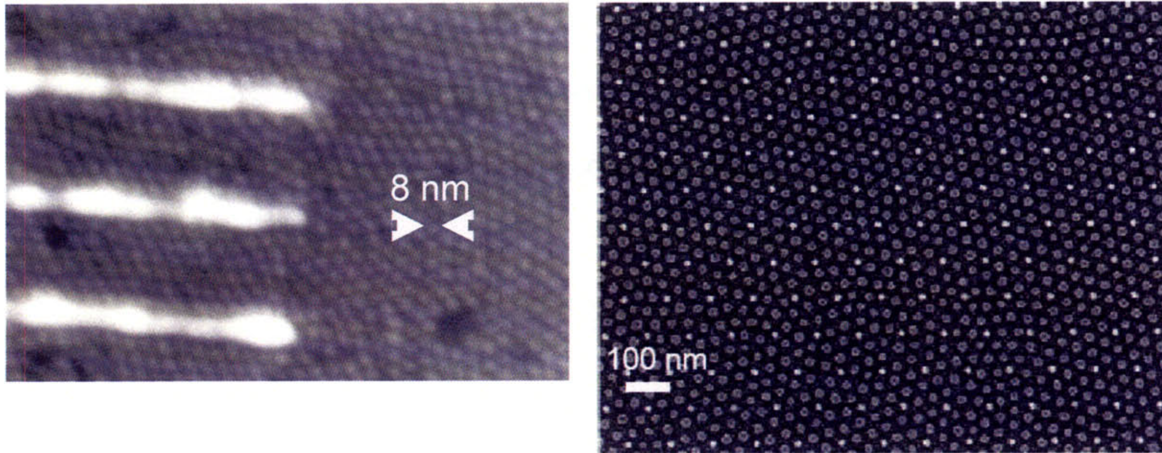

Figure 1-3: Left*: 8-nm-wide CdSe quantum dots forced into a hexagonal lattice by 10-nm-wide Ti-Au lines fabricated using SEBL.* Right*: Block copolymers organized into a lattice using 12-nm-wide hydrogen silsesquioxane (HSQ) posts (bright points) as guide structures (micrograph courtesy J. Yang).*

The question of SEBL resolution arises in templated self-assembly because SEBL, by enabling fabrication of the templates, provides the "bridge" between top-down and bottom-up fabrication. Since the top-down process has to be able to pattern template structures on the order of the size of the materials being templated, the resolution of the top-down process is currently a limiting factor in templated self-assembly. With groups successfully manufacturing quantum dots that are only 2 nm in diameter,[49] there is virtually unlimited demand for better SEBL resolution in this area.

From a purely scientific standpoint, understanding the resolution limit of SEBL, and the factors behind it, is extremely interesting. Quite a bit of work has been done over the years in this regard,[32,42,43] but the predicted resolution limits have been repeatedly broken. As tool technology improves and better resist-processing methods are developed, more and more non-fundamental resolution barriers are removed, allowing an unprecedented opportunity to investigate the technology's possible true, fundamental resolution limit.

1.3 Thesis Overview

The thesis will begin with discussion of a technique for optimizing PMMA contrast by controlling development temperature, providing an overview of the many contrast-enhancement techniques developed over the years in the process.[12] Chapter 3 will present a thorough theoretical and experimental study of electron-solid interactions and attempt to describe the current limits of SEBL resolution and the mechanism behind it. Chapter 4 will discuss a novel process for high-resolution metal evaporation and liftoff developed in the process of fabricating high-resolution Josephson junctions.[50] This chapter will also discuss some of the concepts introduced in the previous two chapters in a more applications-based context.

Chapter 2: Optimizing PMMA Contrast via Control of Development Temperature

Many of the previously-discussed applications of nanolithography, such as templated self-assembly and nanoimprint master templates, require feature diameters on the order of or smaller than 10 nanometers. While patterning structures as small as 15 nm with SEBL is relatively trivial, getting beyond this resolution can be problematic, as factors like beam diameter, electron scattering, and resist contrast can no longer be ignored. In this section, we discuss the results of an attempt to increase the contrast of PMMA using a temperature-optimized development process, and as a result push our final process resolution into the 10-nm regime.

2.1 Resist Contrast

Resist contrast is a relatively simple metric for determining how "good" a resist is. Contrast measurements are typically performed by exposing several features on a resist-coated sample at different doses, developing for a fixed time, then measuring the amount of resist remaining post-development as a function of dose. The final "contrast curve" is usually plotted as remaining resist thickness (normalized to the initial thickness) vs. dose, although dissolution rate as a function of dose is also used and is more useful as it makes the measurement time-independent.

As figure 2-1 shows, an ideal contrast curve looks like a step function; below the threshold dose, no resist development takes place, while above the threshold dose the development rate is effectively infinite. This behavior, unfortunately, cannot be achieved with real-world materials, and experimentally-measured contrast curves generally look similar to the red curve in 2-1, with a sloped region between the dose at which the resist starts to develop (D_0) and the dose at which the resist fully develops away (D_1). Contrast is generally quantified with the following expression:

$$\gamma = \left[\log\left(\frac{D_1}{D_0} \right) \right]^{-1} \tag{2.1}$$

Where γ is defined as the contrast, essentially the slope of the region between the D_0 and D_1 doses. The higher the γ the better the resist contrast; a resist process with perfect contrast would have a γ of infinity.

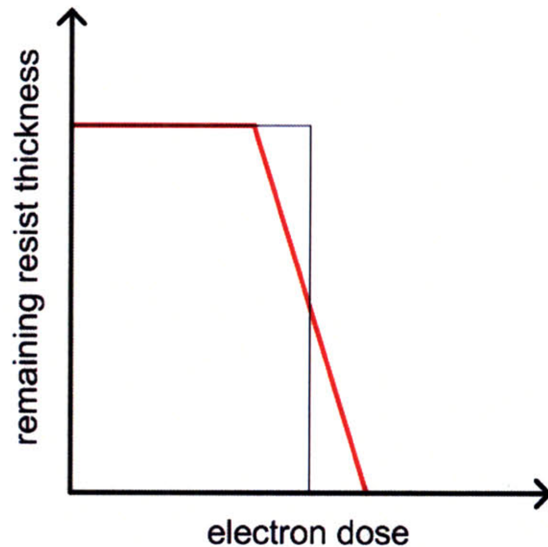

Figure 2-1: Schematic illustration of infinite (black line) and finite (red line) contrast, plotted as remaining resist thickness as a function of electron dose. In the infinite case, the transition from no development to full development happens at a single critical dose, while in the more realistic finite case the transition occurs more gradually.

It is important to mention that resist contrast is an extremely non-fundamental measurement. Resist thickness, developer type, development time and temperature, and any number of other external parameters are convolved into contrast measurements along with resist "quality." As a result, using resist contrast to make blanket statements about the fundamental capabilities of a resist (e.g. "PMMA is a better resist than HSQ because it has a higher contrast") is inappropriate; resist contrast should only be used to directly compare different resist *processes*, in which all of the previously-mentioned parameters are clearly specified. While this would seem to limit the usefulness of resist contrast as a metric, its ease of measurement and ability to evaluate the effect of a single parameter on

a resist process (as we will see in the following sections) make it an important, if limited, tool for the study of resist behavior.

2.1.1 Contrast Enhancement

All other things being equal, an increase in contrast translates directly into an increase in process resolution. To illustrate this, consider the idealized dose profile in figure 2-2.

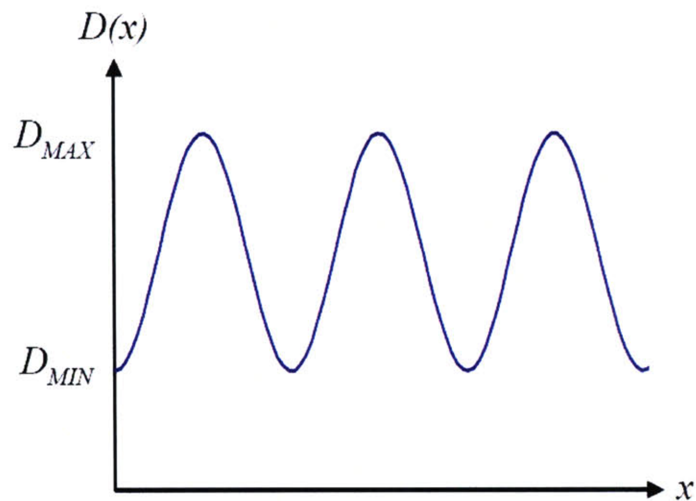

Figure 2-2: 1D dose profile of an idealized sinusoidal grating structure. The doses D_{MAX} *and* D_{MIN} *define the dose modulation of the grating.*

The *dose modulation function* for the grating structure in figure 2-2 can be defined as:

$$M_D \equiv \frac{D_{MAX} - D_{MIN}}{D_{MAX} + D_{MIN}} \tag{2.2}$$

The modulation in the dose profile of a grating structure is inversely proportional to its pitch, which will be discussed in more detail in chapter 3.

We now consider two schematic contrast curves, one with high contrast and one with low contrast as defined by eqn. (2.1).

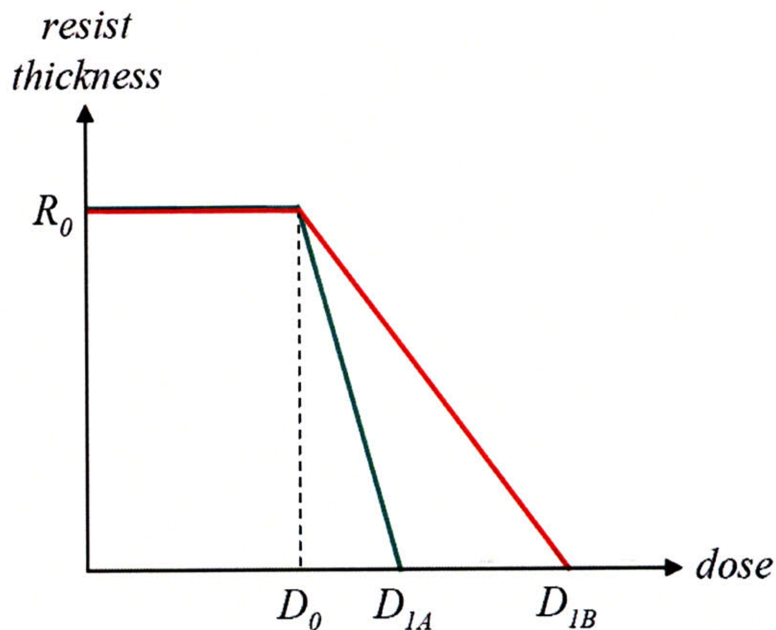

Figure 2-3: Schematic contrast curves (in remaining resist thickness vs. dose format) for two hypothetical resist processes, one with high contrast (green curve) and one with low contrast (red curve). R_0 *is the initial resist thickness;* D_0 *is defined as the minimum dose at which resist development occurs and* D_1 *is defined as the minimum dose at which the resist fully develops away after a set development time. The difference between the two defines the contrast according to equation (2.1).*

The curve shows how much of the initial resist thickness R_0 remains as a function of dose, after a set development time t_D. The dose D_O is defined as the minimum dose at which any resist development occurs; the dose D_I is the minimum dose at which the resist fully dissolves away after time t_D. We can define a *contrast modulation function* similar to equation (2.2) using these curves:

$$M_C \equiv \frac{D_1 - D_0}{D_1 + D_0} \qquad (2.3)$$

Superimposing the information in figure 2-3 on figure 2-1 begins to suggest the relationship between contrast and resolution.

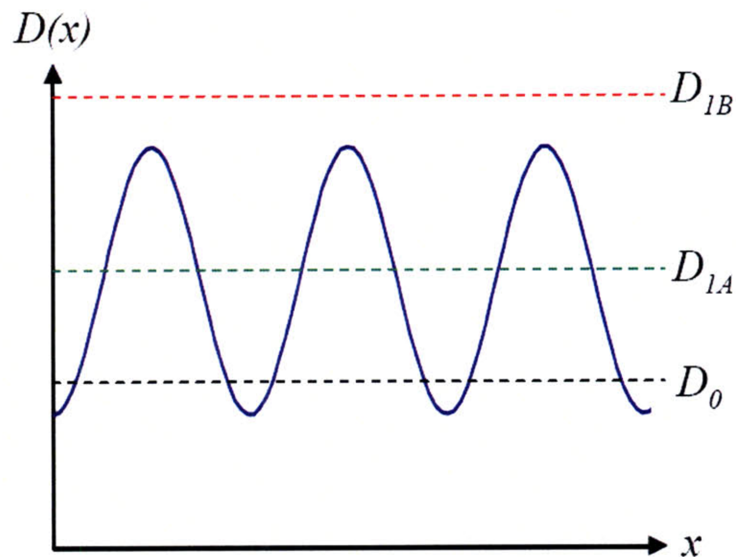

Figure 2-4: Dose profile of figure 2-2 with the relevant doses from the contrast curves in figure 2-3 superimposed. In the part of the pattern where the dose is below D_0, *no dissolution of the resist takes place during development. In the high-contrast case, full development happens when the dose is greater than* D_{1A}, *with partial development happening when the dose is between* D_0 *and* D_{1A}. *In the case of* D_{1B}, *where the contrast modulation function exceeds the dose modulation function, all of the pattern lies in this in-between regime and none of the features will fully develop.*

In the high-contrast case in figure 2-4, the resist dosed above D_{1A} will fully dissolve away, the resist dosed below D_0 will not develop at all, and any resist in the region between the two doses will undergo some partial development, which will result in the slightly sloped sidewalls shown in the final developed pattern in figure 2-5(a). In the case of the low-contrast resist process, the contrast modulation function exceeds the dose

modulation function ($M_C > M_D$), which means that none of the resist in the pattern will develop fully away, leading to the resist profile shown in figure 2-5(b). The resist contrast, then, defines the amount of dose modulation required for a pattern to yield. Since dose modulation is inversely proportional to pattern density, higher contrast enables the patterning and successful development of smaller, denser structures.

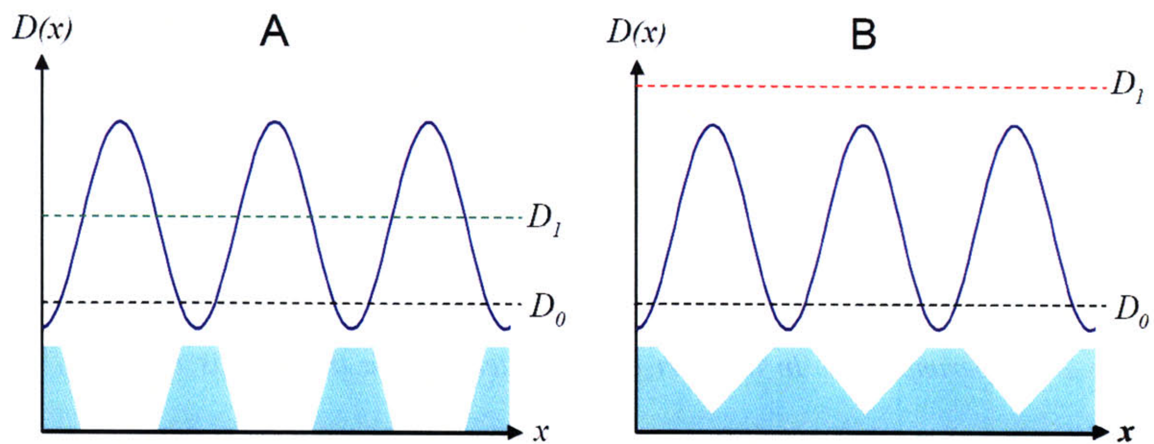

Figure 2-5: Final developed resist profiles for the dose modulation function shown in figure 2-2 and the contrast curves of figure 2-3. In case A (the high-contrast process) the resist has yielded a recognizable grating structure with only slight inward sloping of the sidewalls, which is unavoidable with any finite-contrast resist. In case B (the low-contrast process), however, none of the resist has fully cleared, creating a final structure with severely sloped sidewalls and no exposed substrate. Postprocessing on this type of resist profile is generally impossible, so the pattern in case B cannot be said to have yielded.

As our idealized example illustrates, there is at least in principle a strong correlation between resist-process contrast and lithographic resolution. As a result, many different chemical and mechanical methods have been attempted in order to improve the resist contrast in electron beam lithography processes.[30,51,52] Of these methods, one of the most successful (at least in the case of PMMA[15] and similar resists, such as ZEP520[53]) has been cold development—simply developing the resist in a developer solution cooled below room temperature.

2.2 Cold Development

The vast majority of photo- and electron resists in use today are developed in aqueous or organic solvents kept at or near room temperature (25°C). The reason for this is primarily convenience—room-temperature developers do not need bulky and costly temperature-control equipment. Coupled with the fact that development contrast is not a limiting factor in most processes, this has until recently discouraged widespread investigation of the effect of developer temperature on contrast. As electron beam lithographers have struggled to improve process resolution even marginally, though, it was inevitable that development parameters in general, and developer temperature in particular, would eventually be examined in great detail.

2.2.1 History

Cold development of PMMA was pioneered approximately a decade ago; a 1998 paper by Pantenburg et al is one of the earliest references to it in the literature.[54] As feature size was not a major concern (or was limited by factors other than resist contrast) at this time, early papers on cold development focus on its efficacy in improving resist sidewall profiles, resulting in cleaner and more robust pattern transfer.[51,54] It was not until 2004 that improving lithographic technology allowed cold development to be examined purely as a resolution-enhancing technology by Hu et al,[15] but it appeared to be a qualitative improvement in this regard as well.

Though cold development was widely adopted by the electron-beam lithography community following publication of the Hu paper, the mechanism behind its contrast enhancement was still poorly understood. This was remedied by a 2006 paper by Ocola et al, which gave a detailed, plausible explanation for the success of cold development.[53]

2.2.2 Mechanism

PMMA, as is well-known, is a chain-scission resist; that is, it is exposed when incident photons or electrons break bonds in long PMMA molecules and turn them into several shorter molecules. When exposed to organic solvents, the short PMMA chains created by scission are able to dissolve away, while the long, unexposed chains remain entangled in a matrix and stay in place. The relationship between the molecular weight of a PMMA

molecule and its solubility is extremely nonlinear, which makes it an excellent, high-contrast electron beam resist under almost all processing conditions.[21,26]

The mechanism by which cold development causes an enhancement in resolution is not widely understood. Ocola et al have suggested that the key lies in the glass transition temperature (T_g) of PMMA.[53] This theory assumes two things: that the glass transition temperature (T_g) of a PMMA molecule is proportional to its molecular weight,[55] and that PMMA molecules will dissolve away when placed in a solution with a temperature above their glass transition temperature. The theory relies on the fact that, when a feature is exposed in PMMA using an electron beam, resist around the edges of the feature is partially exposed due to scattering of the beam, secondary electron generation, and other effects, resulting in medium-length, partially-exposed molecules surrounding the short molecular chains of the exposed area.[56] When developed at room temperature, some of these partially-exposed chains will be above their T_g and thus able to develop away, resulting in a biasing of the exposed feature. When the developer is cold, however, its temperature is below the T_g of these molecules; as a result, more of the partially-exposed PMMA is "frozen" in place and the final developed feature matches the dimensions of the exposed one much more precisely. While this theory has an attractive simplicity, it contains several questionable assumptions. The suggestion that PMMA chains with $T_g<T_{developer}$ will dissolve during development while chains with $T_g>T_{developer}$ will not ignores the fact that the glass transition temperature, when applied to polymers, is not a clear delineation point at which previously stationary material begins to flow. Moreover, T_g is a bulk property and not designed to apply to single molecules; the effect of

polydispersity (the distribution of molecular weights present in both the exposed and unexposed resist) on the process, if any, is not addressed at all.

Another possible explanation of the cold-development mechanism takes some of the unaddressed issues in the Ocola theory into account. When a small feature is exposed in PMMA, the continuous nature of the deposited energy density in the resist will result in boundary region between the "exposed" and "unexposed" sections of the resist, as illustrated in figure 2-6(a). While the exposed region of the resist will consist almost entirely of soluble polymer fragments and the unexposed region of insoluble molecules, this boundary region will contain both soluble and insoluble polymer fragments, due to both the initial polydispersity of the PMMA and the random nature of chain-scission events.[57] When placed in developer, the molecular fragments in the boundary region will have a tendency to phase-separate; the soluble fragments will diffuse toward the exposed region and the insoluble fragments will diffuse toward the unexposed region, eventually resulting in a wider region of soluble polymers as shown in figure 2-6. Since phase separation can be described by diffusion, which is a temperature-dependent process,[58] developing at low temperatures will inhibit this separation, preserving the boundary region (which will be indistinguishable from unexposed resist when removed from the developer[59]) and resulting in a narrower developed feature.

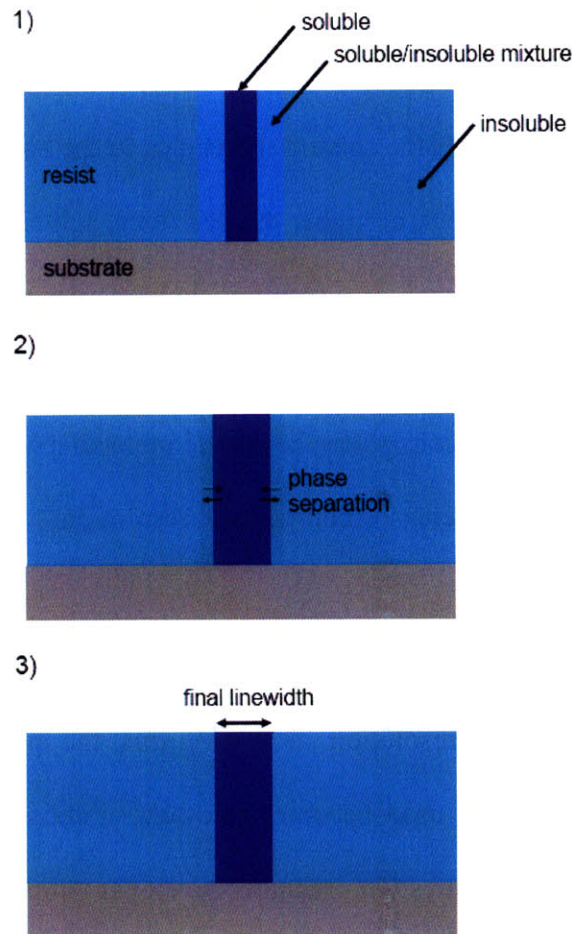

Figure 2-6: Schematic illustration of one possible explanation of the resolution-enhancing mechanism of cold development. When a feature is exposed in PMMA, the soluble resist in the exposed region is surrounded by a boundary region of resist that, due to the initial polydispersity of the PMMA and random nature of chain scission, contains both soluble and insoluble polymer chains (1). During development, this region phase-separates, with the soluble chains diffusing toward the soluble region and the insoluble chains diffusing toward the insoluble region (2). The result is a region of soluble PMMA that is larger than the initial exposed feature, resulting in a degradation in resolution (3). Cold development helps prevent this by limiting the diffusion that can occur in the boundary region, since diffusion is a thermally-dependent process.

A third possibility is that maximum size of a polymer chain that can be removed from the PMMA matrix and dissolved is a temperature-dependent parameter itself. This is a plausible theory as the motion of the solvent molecules in the solution is Brownian and, as a result, temperature-dependent; at higher temperatures, solvent molecules can exert a greater force on PMMA chains and, as a result, dislodge larger polymer molecules from the matrix. In this case, lowering the temperature decreases the maximum molecular weight that can be dissolved which, given the spatial molecular-weight distribution of an exposed feature, will result in increased contrast and resolution.

Regardless of the exact mechanism responsible, cold development indisputably has a beneficial effect on real-world resolution. Knowing this, the question of which "cold" temperature should actually be used becomes relevant. Published data shows a clear trend toward finer resolved features with reduced developer temperature,[15] but the lowest developer temperature reported in the literature is -17°C.[53] This is substantially higher than the freezing point of most PMMA developers (probably the ultimate practical lower limit to developer temperature), and suggests that even higher resolutions may be possible by developing at extremely cold temperatures.

2.3 Contrast Experiments

As previously-published cold development work had stressed the relationship between PMMA contrast and development temperature, our initial investigation of ultra-low-

temperature PMMA development focused on measuring the contrast over as wide a range of "cold" temperatures as possible.

2.3.1 Description

Commercially-available PMMA with an average molecular weight of 950K was used in all of our contrast experiments. For simplicity, our standard in-house developer (3:1 isopropanol:methyl-isobutyl-ketone), which has a freezing point of approximately -80°C, was also used in all experiments. By combining several cooling methods, we were able to measure contrast data at temperatures ranging from 15 to -60°C. For the 15 to -30°C temperature range, we used a commercially-available Ladd Research Stir-Kool thermoelectric chiller in the configuration shown in figure 2-7. This system had the advantage of being equipped with both a temperature controller and a magnetic stirrer, allowing us to control temperatures to within 0.1°C as well as keep the developer stirring continuously to ensure uniform temperature throughout the bath.

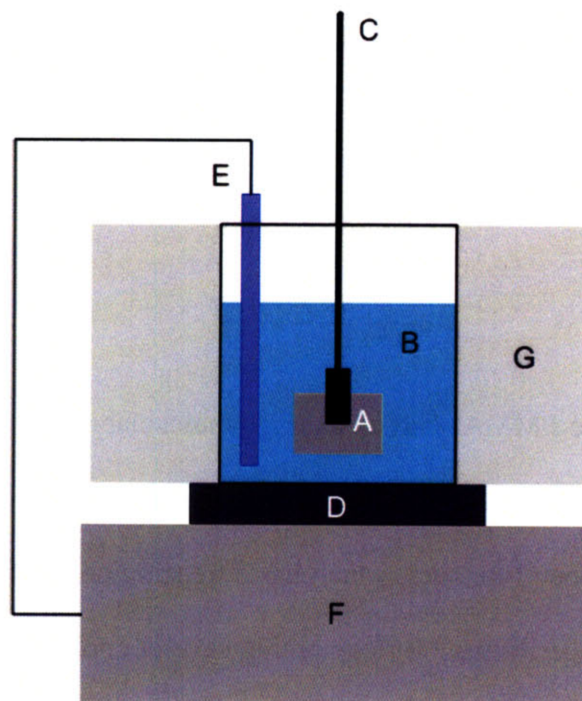

Figure 2-7: Schematic diagram of our cold-development system based on the Ladd Research Stir-Kool thermoelectric chiller. The sample to be developed (A) is immersed in a beaker of developer (B) via a dipstick with an alligator clip to hold the sample at the end (C). The beaker sits on a thermoelectric block (D), which is regulated using a thermocouple (E) connected to a temperature-control system inside the Stir-Kool unit (F). In order to get maximum efficiency from the chiller, the beaker was sheathed in foam insulator to minimize atmospheric heating of the bath (G). A magnetic stirrer (not shown) in the bath ensured temperature uniformity by keeping the developer in constant motion.

The Stir-Kool unit was not powerful enough to cool our developer below about -30°C, so for colder temperatures the dry ice bath system in figure 2-8 was used. The procedure consisted of immersing a beaker containing a large amount of developer in a larger beaker containing a mixture of dry ice and isopropanol, which would typically reach

about -75°C. The temperature of the developer was continuously monitored as the entire system was allowed to slowly warm up to room temperature. The volume of the developer was chosen so that its thermal mass would keep it from warming by more than about 1°C per minute. Temperature uniformity was maintained by manual stirring of the developer with the thermometer, and development at a given temperature was accomplished by simply waiting for the developer to reach that temperature and running the development process; for a 60-second development, this gave a temperature accuracy of ±1°C. While not as precise as the Stir-Kool-based system, the dry-ice-bath method was adequate for our purposes and produced results that were reasonably repeatable if care was taken during the processing.

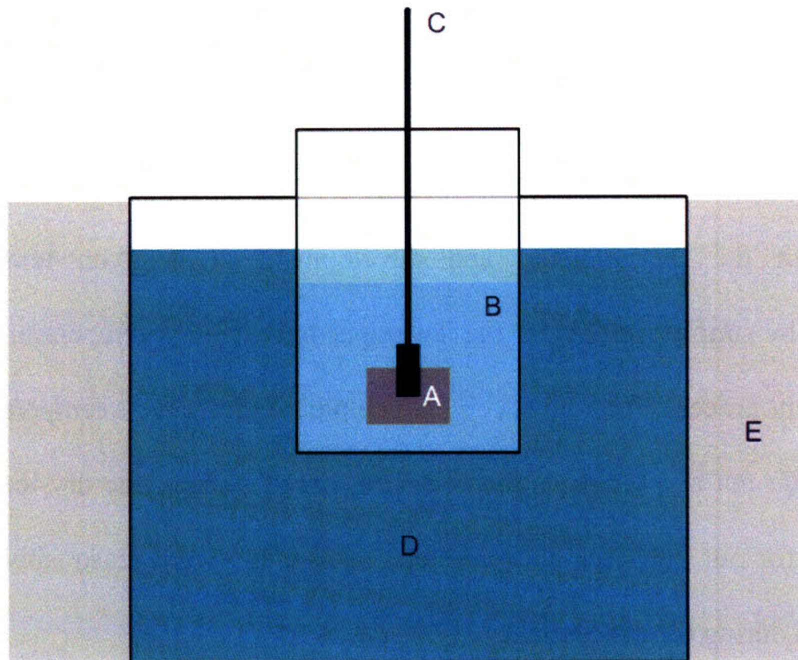

Figure 2-8: Schematic diagram of the dry ice bath used to develop PMMA at temperatures below -30°C. The sample (A) is immersed in a large beaker of developer (B) using the same alligator-clip dipstick as figure 2-7 (C). The beaker of developer is suspended in a bucket of dry ice and isopropanol with an initial temperature of ~-75°C once the developer has warmed up to the desired development temperature. To slow the warming process, the bucket was wrapped in thermal insulation (E) to help thermally isolate it from the environment.

In both cases, the development procedure was identical: the sample would be attached to a dipstick via an end-mounted alligator clip, then immersed in the developer for a given length of time (generally 60 seconds). At this point, standard procedure would be to rinse the sample in isopropanol or some similarly weak solvent to remove the developer, but any room-temperature solvent rinse will significantly degrade the resolution gain from

the cold development, so the samples are simply removed from the bath and dried. The drying step is critical; a 1 cm^2 sample must be dried under a N_2 gun for 60-90 seconds. This time is to allow the sample to return to room temperature; if it is exposed to atmosphere while still cold, water vapor will quickly condense on the sample and form a thin sheet of ice on the surface, which will generally distort and crack the PMMA film.

Contrast curves were measured by using out Raith-150 SEBL system to expose a series of large (20 × 100 μm) bars at a range of doses that increased on a logarithmic scale on a 160-nm-thick PMMA film, then developing the sample at a given temperature for a fixed period of time. The acceleration energy of the beam was 30 keV, and the areal doses varied from 100 $\mu C/cm^2$ to 3000 $\mu C/cm^2$ depending on the development temperature. The large size of the features served two purposes: it ensured that diffusion of the developer into the feature had a negligible effect on development rate (see chapter 4) and also made profilometry measurements much easier by ensuring that the features could be easily found in an optical microscope. The height of the resist remaining in each bar was measured using a Tencor P10 profilometer. Since PMMA is a soft material, it was critical to use a low profilometer stylus force to get an accurate reading here. A force of 5 mg seemed to be low enough to not distort the film; measurements taken at this stylus force were nearly identical to measurements taken on the same sample using an atomic force microscope.

2.3.2 Results

Before discussing the results of the contrast measurements, one interesting effect should be mentioned. After exposing a sample, the extremely-highly-dosed bars were visible immediately after removal from the SEBL tool; in other words, the resist was being altered even before development at high doses. The profilometry measurements in figure 2-9 showed that this was due to resist contraction and followed a logarithmic trend. The mechanism behind this resist contraction during exposure will be discussed in more detail later; for now, it is only relevant because the contraction varies the initial (pre-development) thickness of the resist; when calculating the amount of resist dissolved during development, the measurements in figure 2-9, and not simply the initial resist thickness, must be used as a baseline at high doses.

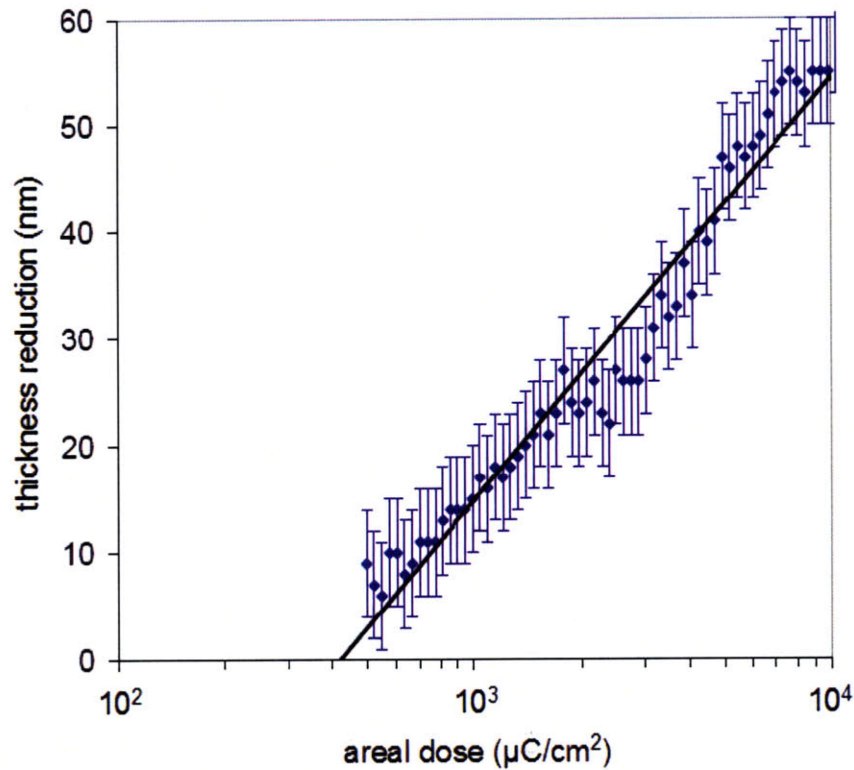

Figure 2-9: PMMA thickness reduction before development as a function of areal dose, measured via profilometry during contrast curve experiments. The error bars here were determined by repeatedly measuring a single feature with the profilometer and calculating the standard deviation of the measurements. For low doses (<1000 $\mu C/cm^2$) this contraction effect is negligible, but at higher doses the resist can contract by 50 nm or more, which must be taken into account when calculating development rates using final and initial resist thicknesses.

The measured contrast curves for temperatures ranging from 15 to -60˚C are shown in figure 2-10:

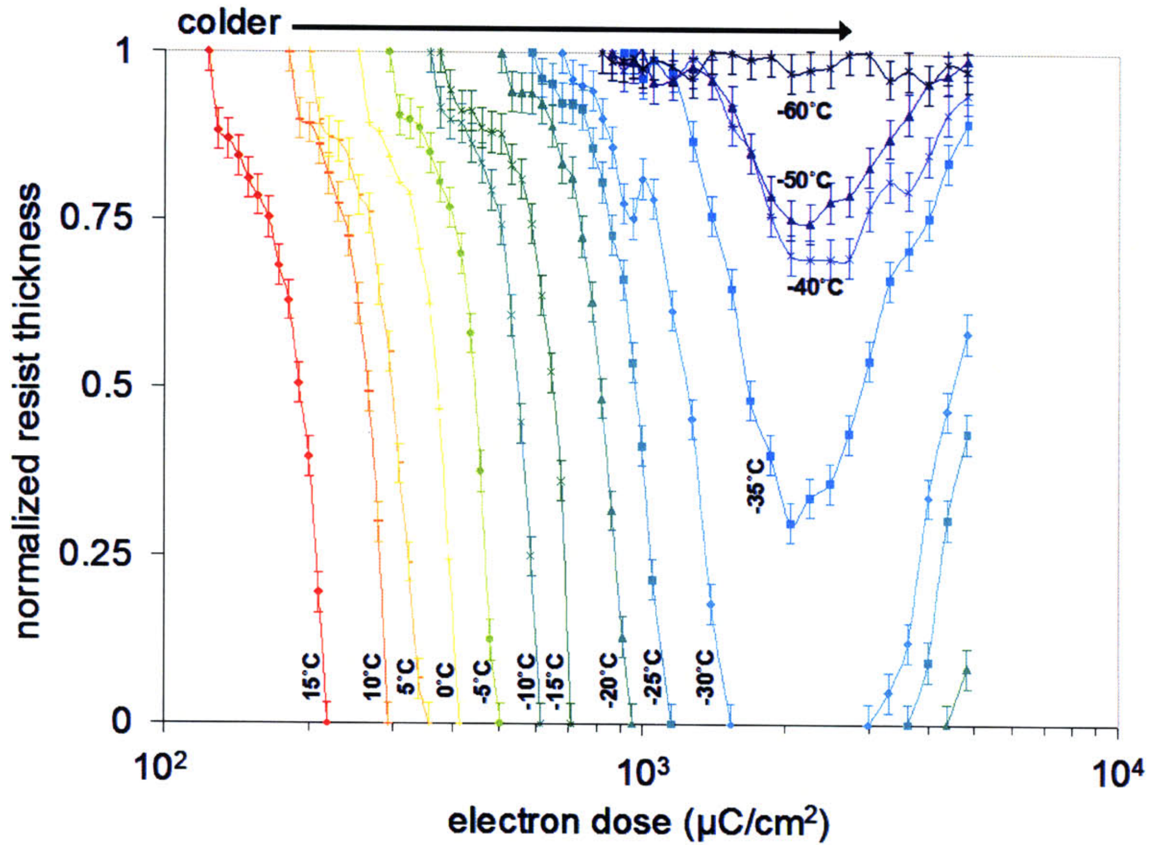

Figure 2-10: Measured contrast curves for PMMA developed in 3:1 IPA:MIBK at various temperatures. The initial resist film thickness was 160 nm and the development time was 60 seconds, except in the -40°C and -50°C cases (120 seconds) and the -60°C case (600 seconds), where longer development times were needed to show any measurable dissolution at all. The contrast (in cases where the resist fully cleared) was measured by calculating the slope of a given curve from the 0.75 (75% of initial resist remaining) dose to the dose where full development occurred. The error bars in this case represent the inherent uncertainty of the profilometer, the characterization of which is discussed in the caption of figure 2-9.

There are two immediately noticeable trends in figure 2-10. The first is the change in sensitivity—as the development temperature is reduced, the clear dose increases almost

exponentially. The second is that, at low temperatures and high doses, a "tone reversal" effect is observed—additional dosing actually causes the resist to develop more slowly, making PMMA effectively behave like a negative resist.[60,61] The tone-rehearsal behavior has a temperature dependence too; the critical doses for both full development and the onset of tone reversal are plotted in figure 2-11. At very low temperatures (-35°C and below) this tone-reversal effect occurs before the resist can develop away, resulting in a distinctive V-shaped curve. In extreme cases (-60°C) the resist is fully frozen in place, and no appreciable dissolution occurs even after 600 seconds of immersion.

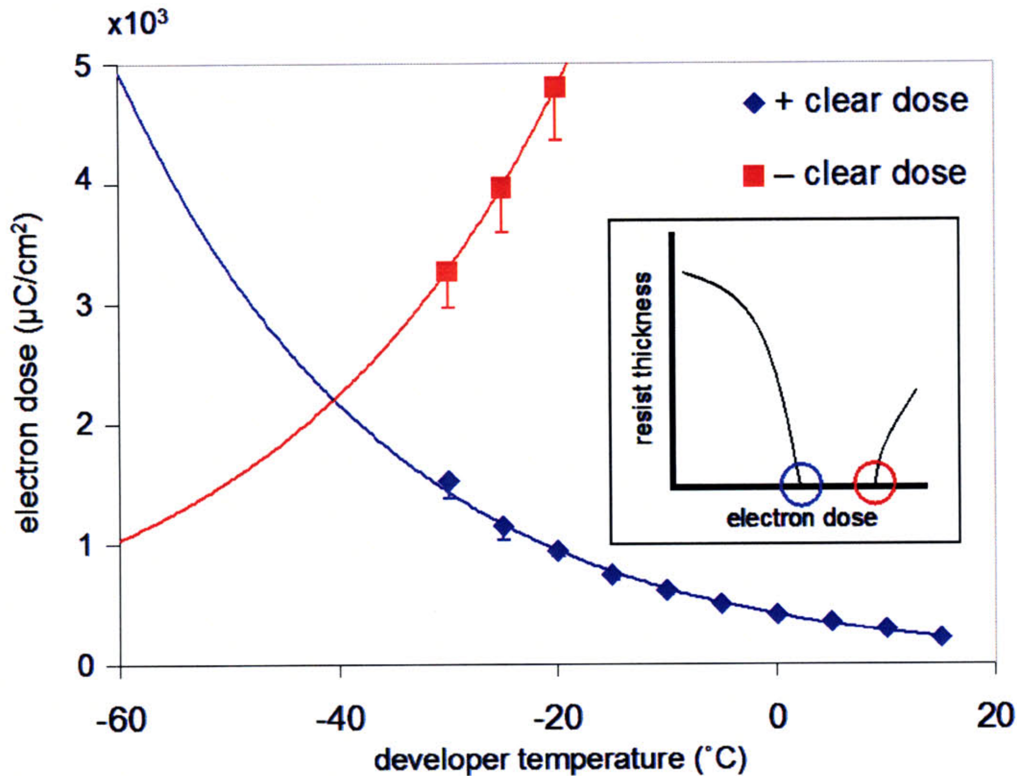

Figure 2-11: Positive clear doses (the dose at which the resist fully develops away) and negative clear doses (the dose at which tone-reversal first occurs) from figure 5-7 plotted as a function of developer temperature (inset: schematic contrast curve illustrating the two doses being plotted). The vertical error bars indicate the uncertainty of the "clear dose," which could have occurred at any point between the first "clear" (or "not clear," in the negative-tone case) feature and the previous feature in the dose array. As the developer temperature is decreased, the positive clear dose increases and the negative clear dose increases. The point at which the two trendlines intersect (approximately -40˚C) corresponds roughly to the temperature at which full development ceases to occur in figure 2-9.

Equation (2.1) was used to calculate contrast values from the data in figure 2-10, using the 0.75 point (75% of initial resist remaining) on the curves as D_0 and the clear dose as D_1. The contrast values as a function of temperature are plotted in figure 2-12.

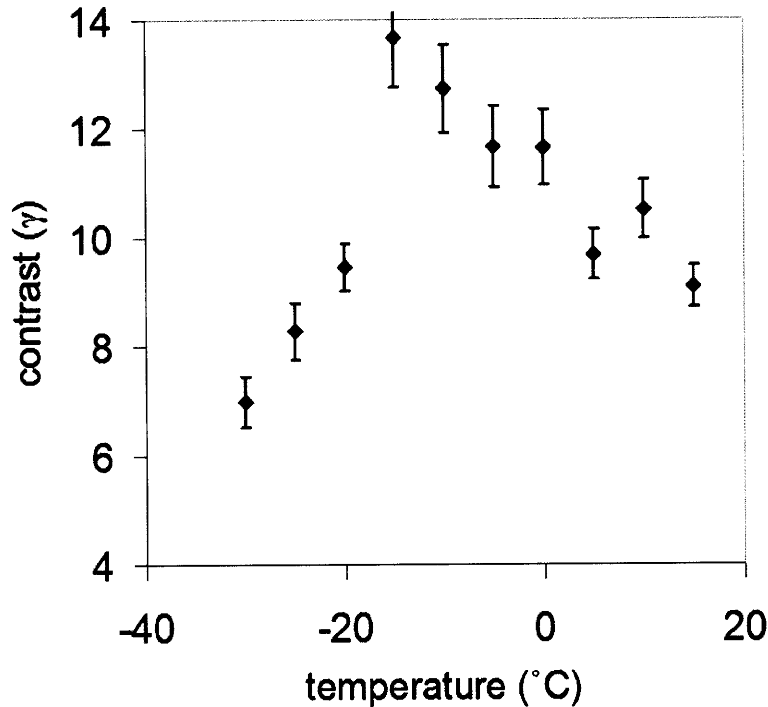

Figure 2-12: Resist contrast as a function of developer temperature, extracted from the contrast curves in figure 2-10. The error bars here were calculated by propagating the uncertainty in the two dose thresholds used in the contrast calculation. From 15°C to -15°C there is a consistent increase in contrast with decreasing temperature, but below -15°C the trend reverses and the contrast drops off sharply with any further temperature decrease.

As the temperature decreases from 15°C to -15°C, there is a nearly linear increase in contrast, with the -15°C higher than the room-temperature contrast by nearly a factor of

two. At temperatures below -15˚C though, this trend sharply reverses and further decrease in temperature leads to sharply degraded contrast; at -30˚C (the lowest dose at which full development occurred in figure 2-10) the contrast is significantly worse than at room temperature.

2.3.3 Discussion

The increase in contrast at low temperatures follows from the glass-transition model discussed earlier, but the decrease in contrast at extremely low temperatures is somewhat surprising. This effect can be explained, however, by recalling that, while polymer chain scission is the dominant exposure mechanism in PMMA, there are actually two processes occurring during exposure: scission and crosslinking.

2.3.3.1 Scission[62]

Scission, also known as degradation, is the primary process that occurs when a PMMA film is exposed to any type of ionizing radiation (in this case an electron beam). The exact mechanics of chain scission are still poorly-understood, but the general process is relatively straightforward. An electron traveling near a PMMA molecule embedded in a thin film exerts a coulombic force on it. In some cases, this force is strong enough to sever one or more bonds in the molecule, which can cause the molecule to become unstable and "split" along the carbon backbone. The result is two smaller PMMA chains with one or more dangling bonds on the monomer at the severed end, which are then

neutralized as the damaged monomer quickly rearranges itself.[62] As the bonds in the carbon backbone of PMMA are weakened by the repulsion of the radicals in their sidechains,[62] they are the most likely bonds to be broken in irradiation events; as a result, chain scission is the dominant process in a PMMA film under most irradiation conditions.

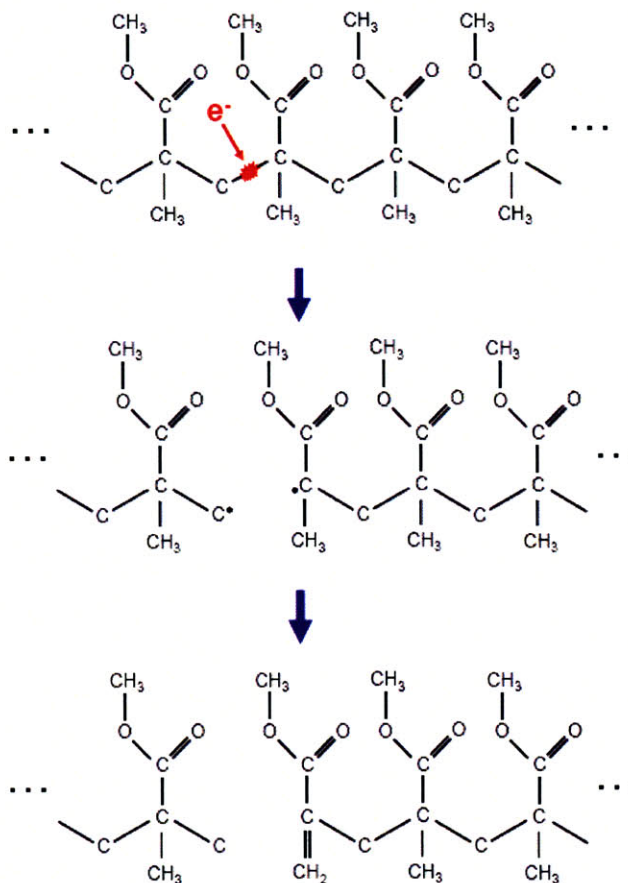

Figure 2-13: Schematic illustration of a possible mechanism for PMMA scission suggested by Alexander et al.[63,64] *The carbon-backbone bond is first broken by an incident electron, generating two PMMA chains with free radicals at their ends. The damaged monomers then rearrange themselves to neutralize the dangling bonds, resulting in two stable chains of PMMA. Note that this is an extremely simplified picture; the specifics of the bond-breaking and recombination are not well-understood and the subject of some debate.*[62-68]

Under most normal (i.e. room temperature) processing conditions, scission events dominate crosslinking events to such a degree that the latter can be entirely ignored. Greeneich derives the following semi-empirical expression for the post-exposure molecular weight of the resist due to chain scission:[25]

$$M_f = \frac{M_i}{1 + \frac{g_e M_i}{\rho A_o}} \tag{2.4}$$

Where M_i is the initial molecular weight, M_f is the final molecular weight, ρ is the resist density, A_o is Avogadro's number, and g_e is the efficiency factor" of the scission process, relating the number of scission events to the energy deposited in the resist (empirically determined to be 0.019 events/eV in PMMA). The equation (in terms of average number of monomers in a PMMA chain as a function of areal electron dose) is plotted in figure 2-13, using the industry-standard initial molecular weight of 950K.

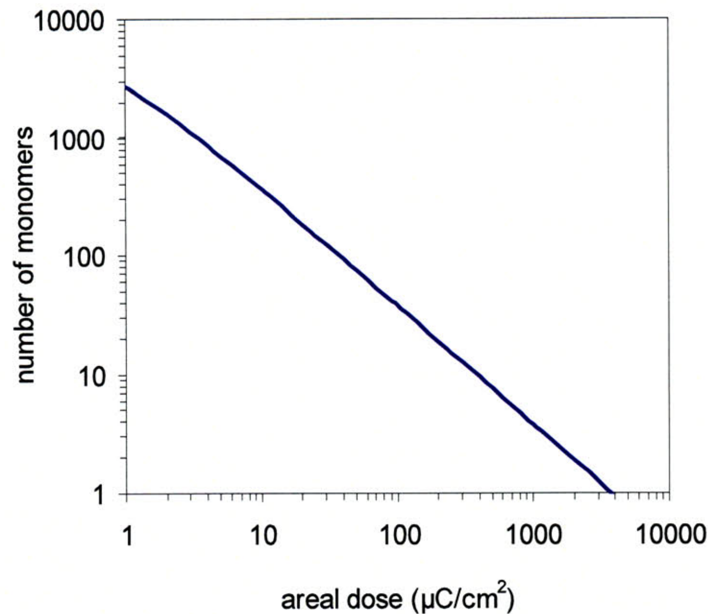

Figure 2-13: Average number of monomers in a PMMA chain as a function of areal electron dose, derived from equation (2.4). Note that at a dose of ~3500 μC/cm² there are no uncut polymer chains left in the resist, meaning no more scission can take place.

At extremely high doses (>3000 μC/cm²) the average number of monomers in a "chain" is one; that is, all chain scission that can occur has occurred.

2.3.3.2 Crosslinking[62]

The chemical specifics of PMMA crosslinking are even less well-understood than those of scission, but it is well-established that, above a certain dose of irradiation, crosslinking events start to dominate scission events in PMMA.[25] One possible explanation for this is that, when enough scission has occurred, the PMMA film is mostly made up of monomers and oligomers (chains of <10 monomers).[27] Ordinarily the weak carbon-

backbone bond is the most likely to be broken under irradiation, but in this case few, if any of these bonds still exist. With no carbon-backbone bonds to break, incident electrons will increasingly damage the bonds in the sidechains of the monomers and oligomers present in the film. The radicals created by these interactions do not neutralize as quickly as the dangling bonds created by scission, instead randomly combining with the dangling bonds in other molecules. The result of this is increasingly large branched and networked PMMA molecules. As hydrogen gas has been observed to evolve from PMMA during crosslinking,[65] it can also be assumed that the film becomes increasingly carbonaceous during crosslinking as carbon-hydrogen bonds are broken.

The thickness-reduction behavior observed in figure 2-6 can most likely be explained by the crosslinking of PMMA at high doses. Heavily crosslinked PMMA contains, by definition, a larger number of chemical bonds than uncrosslinked PMMA. This results in an increase in local density, which causes the exposed resist to contract.[60,61] Profilometry measurements observe this contraction as a reduction in thickness.

The eventual result of the crosslinking process is an increase in the average molecular weight of the PMMA, as monomers are "put back together" by crosslinking. This increase in molecular weight explains the reduction in development rate that causes the tone-reversal behavior seen in figure 2-10; past a certain dose threshold (which in figure 2-10 appears to be ~2500 $\mu C/cm^2$), no more scission can take place and further electron dosing will simply cause more crosslinking, causing the molecular weight to increase and the development rate to drop accordingly. The tone-reversal dose in figure 2-10 is

consistent with the dose at which the average number of monomers in a PMMA chain is less than 10 in figure 2-13.

The reduction in positive-tone contrast as lower development temperatures increase the necessary electron dose can also be explained by crosslinking. At doses of ~1000 $\mu C/cm^2$ (the dose at which contrast starts to degrade per figure 2-10), the PMMA chains are still long enough for some scission to take place, but enough carbon-backbone bonds have been broken that crosslinking, usually insignificant, starts to occur as well. This results in the presence of branched and networked PMMA molecules in the exposed resist. When placed in the organic solvents typically used for development, the dissolution rate of exposed PMMA has a very strong dependence on its molecular weight.[56] The presence of branched and networked material, however, hinders the dissolution of all exposed resist regardless of molecular weight, weakening this dependence and lowering the resist contrast as a result.

Optimizing PMMA contrast, then, is a matter of balancing two effects: the dissolution of partially-exposed molecules at high development temperatures and the excess of crosslinked PMMA produced during exposure when using low development temperatures. As figure 2-12 shows, the development temperature at which both of these effects are minimized when using 3:1 developer is -15°C; for other developers, this temperature will vary.

2.4 Resolution Experiments

While contrast is a useful metric for evaluating resists, it also has some inherent limitations. Its convolution of many variables (development time, developer type, resist thickness, etc.) into a single measurement makes comparing different contrast measurements a dangerous proposition. While evaluating how varying a single parameter (temperature, in our case) affects contrast across an otherwise identical process is appropriate, more general comparisons of contrast data (e.g. comparing the contrast of two types of resist) have little practical meaning, simply because so many variables are not taken into account. As a result, any claim of enhanced contrast needs to be backed up by corresponding evidence of real-world resolution improvement.

2.4.1 Description

PMMA is notoriously difficult to directly examine in a scanning electron microscope, as it charges and warps before any meaningful measurement can be taken, so any process for measuring PMMA resolution must include a pattern transfer step. Our process, diagrammed in figure 2-14, used PMMA with a molecular weight of 950K to pattern a film of SiO_x, which was then used as a hard mask to plasma etch directly into the Si substrate. 30 nm of oxide were evaporated onto a Si substrate, which was then coated with 80 nm of PMMA. The PMMA was patterned with gratings of various pitches and linewidths, then developed for 30 s in 3:1 IPA:MIBK at various temperatures. The PMMA pattern was then transferred into the oxide using a CF_4 plasma etch. The

patterned oxide, in turn, was then used as a mask to transfer the original pattern approximately 100 nm into the Si substrate using a Cl_2 plasma etch. The result, after stripping the oxide, was trenches in a Si substrate that were extremely easy to accurately measure in an electron microscope.

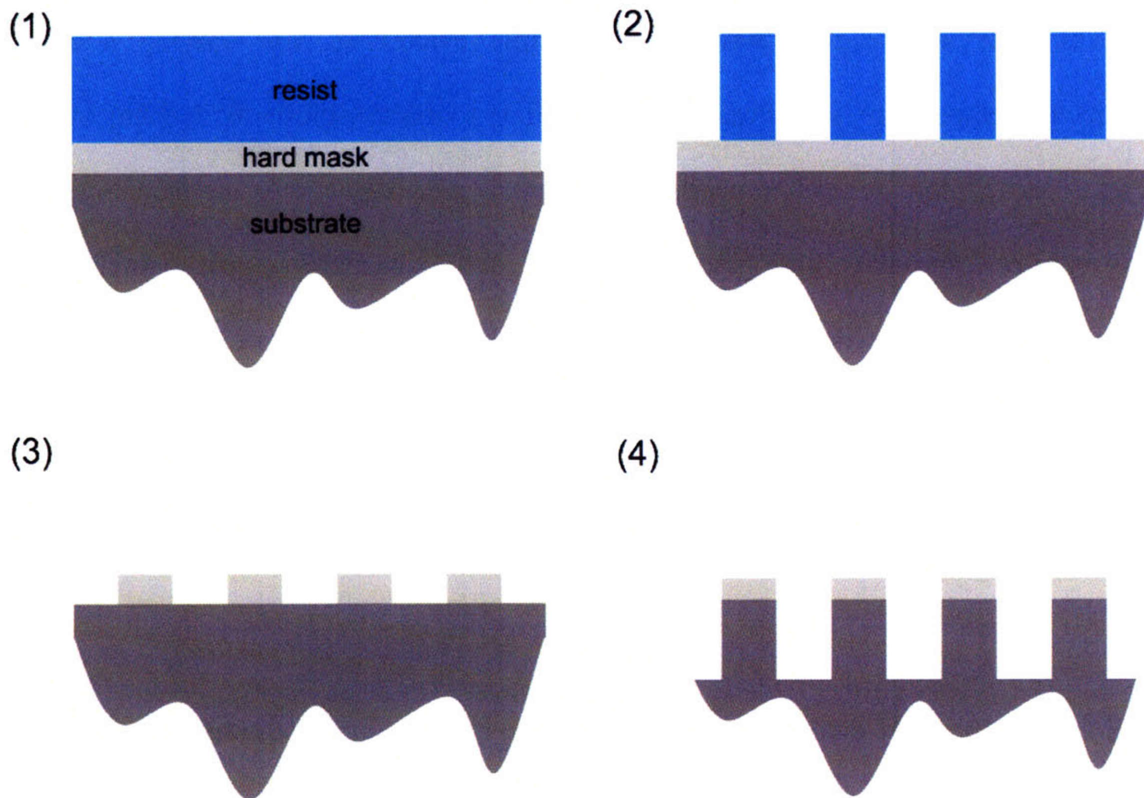

Figure 2-14: Schematic illustration of the two-step etch process used to transfer the PMMA pattern for SEM analysis. The PMMA is spun onto a Si substrate coated with a 30 nm SiO_x hard mask (1). The PMMA is exposed and developed (2), and the developed pattern is transferred into the SiO_x via CF_4 plasma etching (3). The hard mask is then used to transfer the pattern into the silicon via a Cl_2 plasma etch (4). The resulting pattern is much more easily measured with an electron microscope than the developed PMMA itself.

2.4.2 Results

As figure 2-15 shows, the linewidths obtained with this process at various development temperatures closely matched the contrast data in figure 2-12. At 15˚C, dissolution of partially-exposed material limited resolution and the minimum achievable linewidth was ~15 nm. As the temperature was reduced the minimum linewidth decreasee, with the best result (~8 nm) occurring at -15˚C. Below -15˚C, as with the contrast, the resolution fell off sharply; at -30˚C the minimum linewidth was ~27 nm, with noticeable sloped sidewalls and footing. It should be mentioned that the minimum pitch achieved in all cases was 60 nm, suggesting that factors besides developer contrast (most likely the mechanical stability of the PMMA during development and etching) limit the minimum achievable pitch in PMMA-based processes.

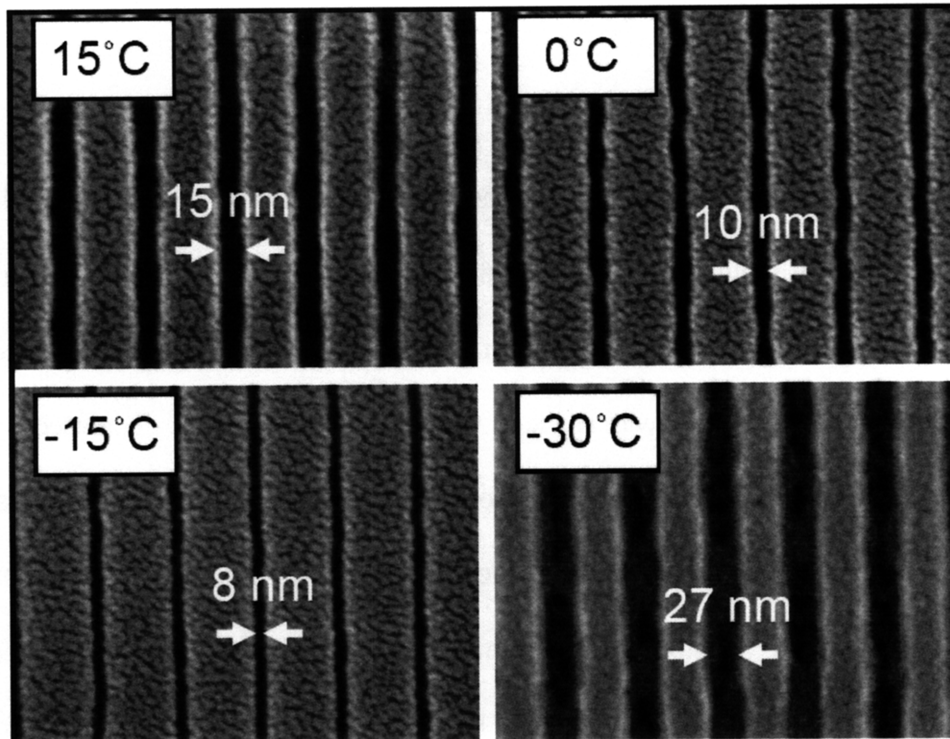

Figure 2-15: SEM images of 60-nm-pitch gratings developed at 15°C, 0°C, -15°C, and -30°C and etched into a Si substrate, showing the minimum achievable linewidth at each development temperature. As predicted by the contrast data in figure 5-7, the resolution improvee as the temperature was reduced, peaked at -15°C, then dropped sharply at -30°C. The poor line-edge definition and bridging in the -30°C micrograph are characteristic of sloped resist sidewalls, a symptom of poor resist contrast. The "scaly" coating on the Si in all four micrographs is a 2-nm-thick Au-Pd layer deposited just before SEM analysis to help reduce charging and had no effect on the process itself.

2.5 Conclusion

Selecting the optimal temperature for PMMA development is a matter of balancing two competing effects. The dissolution of partially-exposed molecular fragments at the edges of features can be reduced by cooling the developer below the fragments' glass transition temperature, but at the cost of reducing the resist sensitivity. If resist sensitivity is reduced too much, the doses required to expose the PMMA will create a large amount of crosslinked material in the exposed region. The presence of these oddly-shaped branched polymers will inhibit the dissolution of the exposed PMMA, resulting in substantial degradation in the contrast. The optimum contrast, then, comes at the temperature where these two effects are minimized; in the case of 3:1 IPA:MIBK developer, this temperature was approximately -15°C. Since different developers change the sensitivity of PMMA quite a bit, this temperature "sweet spot" will vary correspondingly; a naturally insensitive developer (for example, pure IPA) will have a much higher optimum temperature than we observe for 3:1, which is a useful property if the capability to cool liquid to -15°C is not readily available.

We have demonstrated that there is a strong link between resist contrast and real-world lithographic resolution, and that techniques that enhance one will also help the other. By reducing the development temperature of PMMA from 15°C to -15°C, we increased the resist's contrast by nearly a factor of two, and achieved pattern-transferred features as narrow as 8 nm. This latter result is comparable to any result achieved to date using

PMMA, including features patterned using much more expensive and sophisticated tools than our Raith-150.

Chapter 3: Control and Optimization of SEBL Exposure Parameters

Having investigated one particular example of SEBL resolution improvement via contrast enhancement during the resist development process, we now turn our attention to the actual process of electron-beam exposure—what actually happens to a resist film when energy is transferred into it by an incident electron beam.

3.1 Motivation

There are three major parameters and processes that affect resolution to consider here; effective beam diameter, beam scattering in the resist, and secondary electron generation. A full understanding of all three, as well as how they depend on user-controllable exposure parameters, is essential to finding the true resolution limit of SEBL.

3.1.1 Effect of Exposure Parameters on Resolution

While we have seen in chapter 2 that increasing the contrast of resist can have a marked effect on final resolution, we have not yet considered the contribution of the electron-beam exposure process itself. This is an important oversight, because calculations show that when resist contrast is sufficiently high the point-spread function (PSF) of the electron beam, and not the contrast of the resist, is the limiting factor of resolution, at

least when patterning the complex, arbitrary structures that are involved in most real-world lithographic applications. The limitation of resist contrast when determining final resolution is illustrated in figure 3-1.

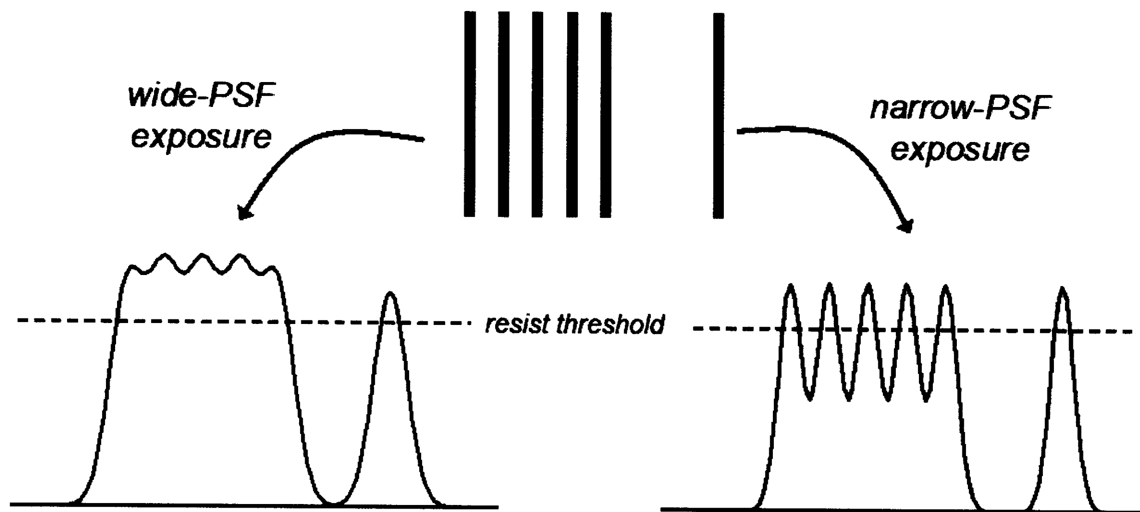

Figure 3-1: Energy-deposition profiles for a pattern containing both dense and isolated features exposed in resist using a wide-PSF beam (left) and a narrow-PSF beam. The resist contrast here is assumed to be infinite, represented by the "resist threshold" line (anything above the threshold will develop, anything below it will not). In the narrow-PSF case, both the dense and isolated features are clearly defined and should all resolve post-development. In the wide-PSF case, however, the dense features are blurred into a single wide line at the dose needed to expose the isolated feature. Decreasing the dose (and thus increasing the resist threshold) in order to capture the modulation of the dense features will raise the resist threshold too high to develop the isolated feature, making it effectively impossible to simultaneously yield dense and isolated features with this PSF.

In order to quantify the relative effect of resist contrast and beam PSF on resolution, we can combine the definition of contrast from chapter 2 with the above energy-deposition profile, as figure 3-2 illustrates.

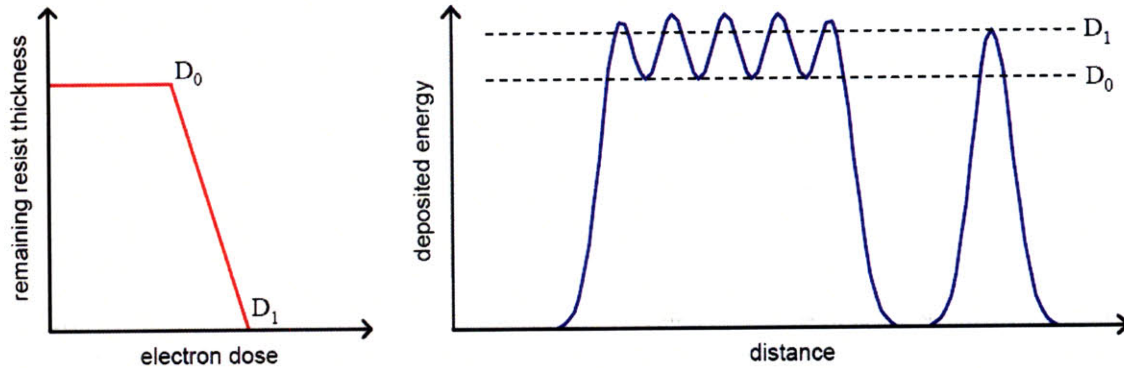

Figure 3-2: Left*: Schematic illustration of a resist contrast curve with the* D_0 *and* D_1 *doses labeled (see Chapter 2 for more details on contrast curves).* Right*: Deposited energy profile for a pattern consisting of both dense and isolated features, with the contrast requirements required for the pattern to yield superimposed. In the dense region, the top of the isolated feature must be* $\geq D_1$ *while the lowest point in the dense features must be* $\leq D_0$*. As the contrast increases (and the gap between* D_0 *and* D_1 *shrinks) it becomes possible to yield smaller pitches together with isolated features, but when the maxima of the isolated feature is less than the minima of the dense features, simultaneously yielding both using the same dose is impossible regardless of resist contrast.*

As the diagram shows, increasing resist contrast allows tighter pitches of dense structures to be yielded simultaneously with isolated structures, but only to a point. As the pitch continues to narrow, the yield conditions described in the figure caption will eventually

require that D_0 be greater than D_1, which is a physical impossibility.

It should be noted that this effect can be mitigated somewhat by using proximity-effect correction (PEC) software to vary the doses of different features, but this is only true to a point: eventually, the modulation in the "dense" energy distribution will be so low that yielding discrete features will require dose control more precise than most SEBL tools are capable of delivering. Thus, even with PEC implemented, the PSF of the beam remains a major limiting factor for resolution.

3.1.2 Limits of Contrast Enhancement

We can quantify this by describing the energy deposition profile of the "dense" features as a sum of Gaussians offset by a pitch p:

$$E(x) = \sum_{k=0}^{\infty} e^{\frac{(x-kp)^2}{2\sigma^2}} \tag{3.1}$$

Where σ is the standard deviation of the Gaussian (the full width at half maximum (FWHM) of a Gaussian is ~2.35σ). If we define the isolated feature as a single Gaussian, and apply the yield criteria described in figure 3-2, we can numerically solve for the minimum yieldable pitch as a function of resist contrast.

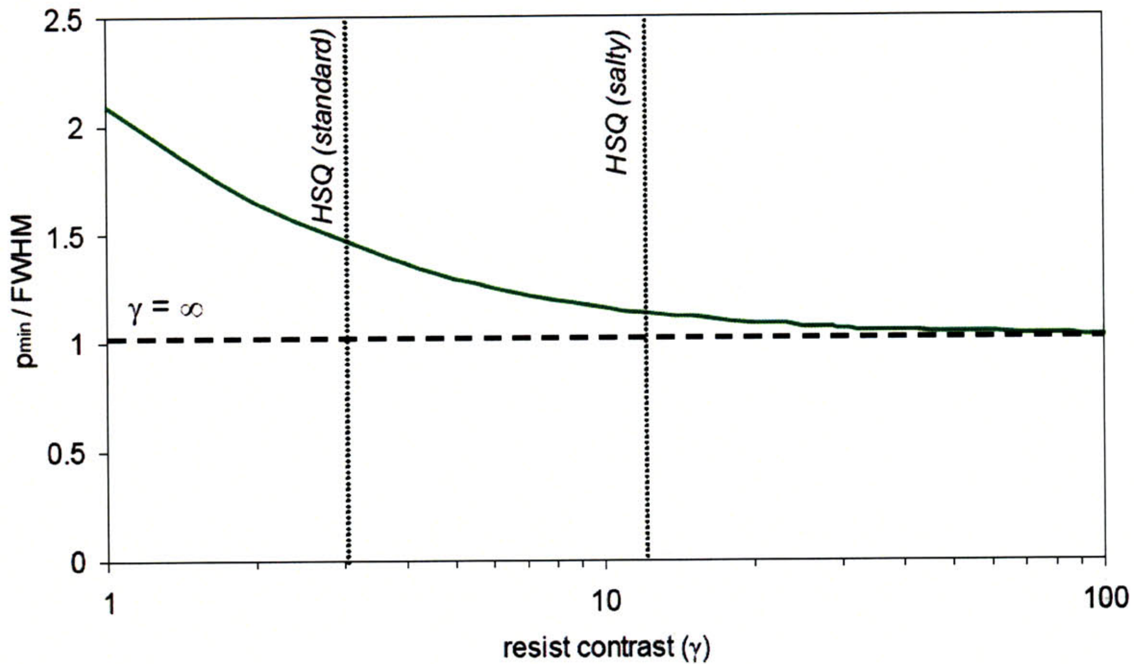

Figure 3-3: Minimum pitch at which it is possible to yield both isolated and dense features (normalized to the FWHM of the primary beam) as a function of resist contrast. Increasing resist contrast does, to a point, increase theoretical resolution (see the difference between the standard development process for hydrogen silsesquioxane (HSQ) (a high-resolution negative electron-beam resist) and the "salty" process developed by Yang et al in 2008[52]), but the gains are asymptotic. Further increase in the contrast of the "salty" development process is unlikely to translate into substantially better resolution, and even with an infinite-contrast resist, resolution is limited to approximately the FWHM of the beam's point-spread function.

This calculation contains a number of simplifying assumptions; the beam profile is assumed to be Gaussian, and resist contrast and beam point-spread function are assumed to be the sole determinants of lithographic resolution. The reality of the situation is more

complicated, but this calculation illustrates the general point—that simply increasing resist contrast is not, past a certain point, a path to higher resolution.

3.2 The Point-Spread Function

Having established that, in a process with reasonably good resist contrast, the beam PSF is in principle the primary resolution limiter, the obvious question is "what sets the PSF width and what can we do about it?" There are three major contributors to the PSF width: primary beam scattering, secondary electrons, and initial beam diameter.

3.2.1 Primary Beam Scattering

Primary beam scattering, illustrated in figure 3-4, occurs when electrons in the beam collide with atomic nuclei in the material and their trajectory is subsequently altered.[69] It is commonly described as two sub-processes: *forward scattering* is the broadening of the incident beam through collisions, and *backscattering* is electrons from the beam scattering back out of the substrate through the resist. Backscattering, which causes beam spreading over length scales of several microns, is not directly relevant to our discussion of resolution at the nano-scale (it can be treated as a small, constant dose offset and generally ignored), so this discussion of primary beam scattering will be primarily limited to forward scattering.

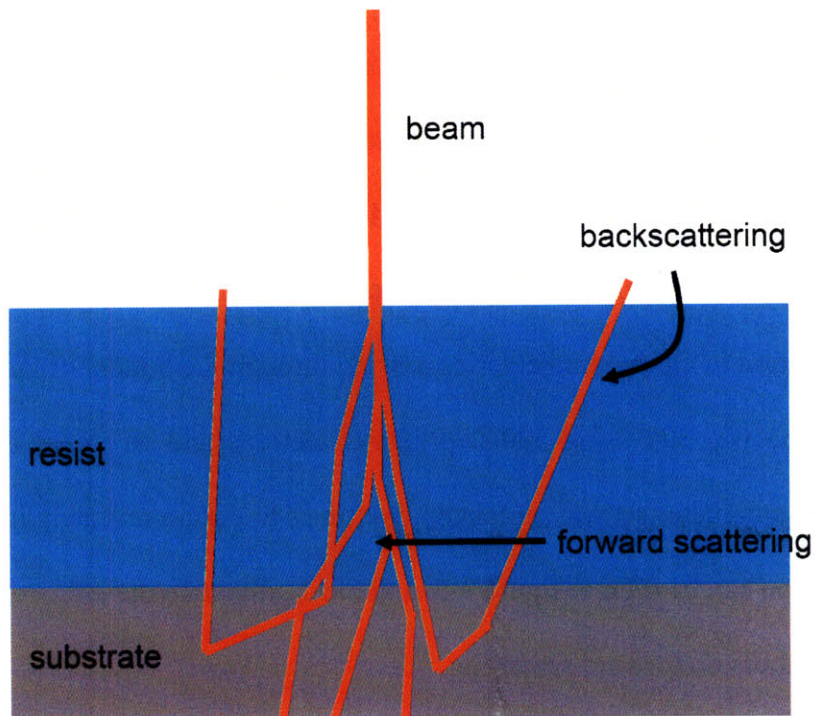

Figure 3-4: Illustration of primary beam scattering as an energetic electron beam travels through a resist layer. As the incident beam travels through the resist, collisions with atoms in the material cause it to broaden (forward scattering). Additional scattering occurs when electrons that have reached the substrate are deflected back out into the resist (backscattering).

The extent of the forward scattering is primarily determined by the resist thickness and the beam energy. Thicker resist will induce more broadening, as the beam has more distance to scatter over, while higher beam energy will reduce scattering by limiting the trajectory change each electron incurs in a collision.

To illustrate these two dependencies, we used CASINO,[70] a free piece of software for performing Monte Carlo simulations of electrons traveling through different materials, to model electron beams of various energies traveling through PMMA films of various thickness. The forward scattering range α (which corresponds to the standard deviation of the electron distribution) was calculated from the simulation results by analyzing the spatial distribution of electron trajectories passing through the bottom of the PMMA film. Each simulation was run using 50000 primary electrons and an initial beam width of zero, and each parameter set was simulated five times to ensure repeatability. The results of the simulation can be seen in figure 3-5, and nicely illustrate the effect of beam energy and resist thickness on forward scattering.

There are two important caveats to keep in mind with these results. Using the distribution of electron trajectories to calculate α is non-fundamental, and fails to take into account how much energy was actually transferred to the resist by each electron. From the point of view of resist exposure, the important parameter to measure is the spatial distribution of the energy deposited by the beam in the resist. Without an easy way to measure this value in CASINO, however, the trajectory distribution provides a good first-order approximation of the beam spread. Additionally, only primary electrons are taken into account by the simulation; any secondary electrons generated during inelastic collisions are ignored. Since we are only concerned with forward (elastic) scattering at the moment, this is acceptable, but a more detailed treatment will eventually be needed to study the effect of secondary electrons, which are discussed in the next section.

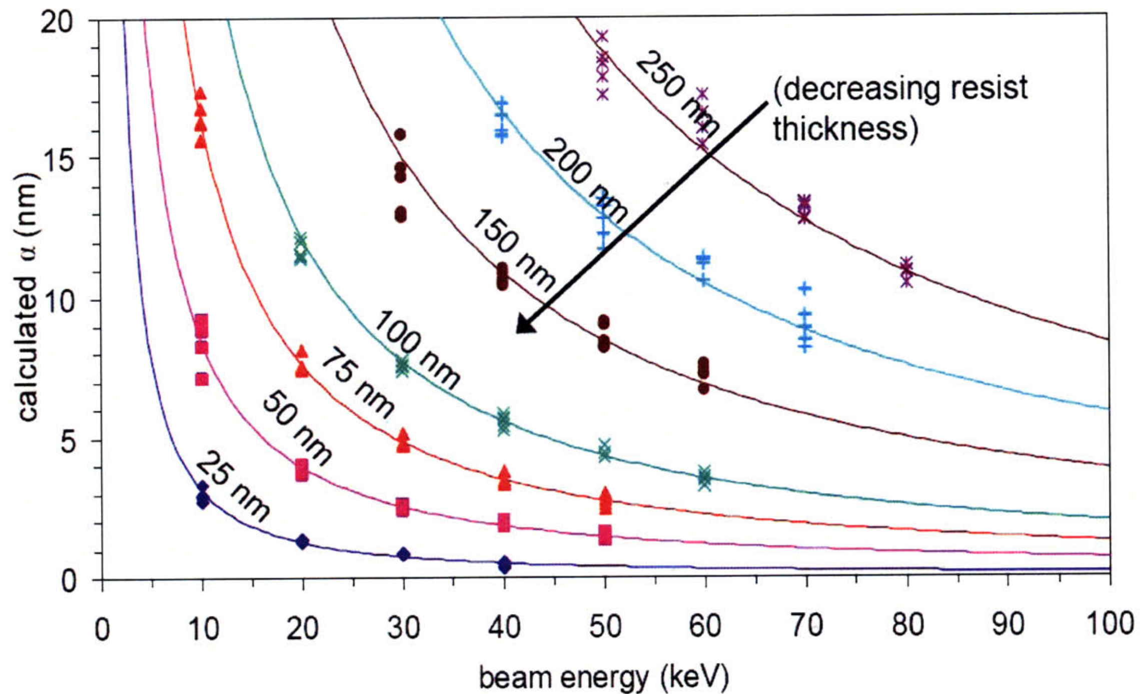

Figure 3-5: Forward scattering coefficients (α is the standard deviation of the final beam distribution) as a function of beam energy for various thicknesses of PMMA, calculated using CASINO, a free Monte Carlo modeling program.[70] For simplicity, the initial beam profile was assumed to be a delta function (zero width) in this simulation. The scattering width decreases dramatically as the beam energy is increased, but using thicker resist results in more scattering.

This behavior is well-documented[21,36,56,71], and the standard solution to the problem of forward scattering is to use the thinnest resist and highest beam energies possible. This solution tends to mitigate the effects of primary beam scattering, but there are still two other factors to consider.

3.2.2 Beam Diameter and Secondary Electrons

While forward scattering is caused by elastic collisions between electrons in the incident beam and particles in the material, it is also possible for inelastic collisions to occur, transferring energy to particles in the resist and occasionally freeing a valence electron. These secondary electrons, with energies ranging from a few eV to nearly half the incident beam energy, typically travel normal to the primary beam and can deposit a substantial amount of energy in the resist.[32,34,43,72] The generation of secondary electrons is illustrated in figure 3-6.

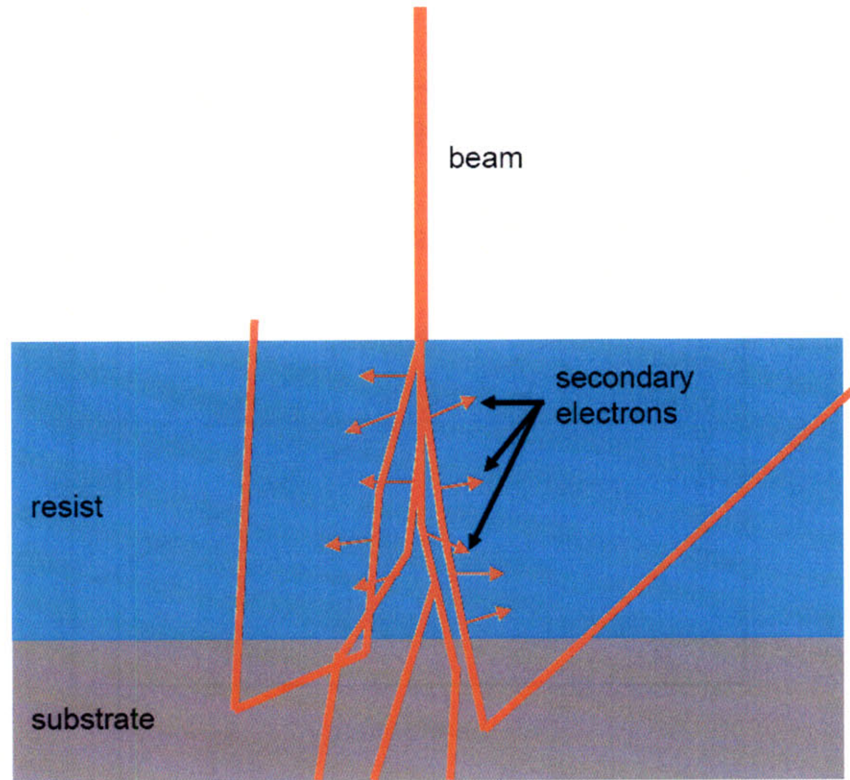

Figure 3-6: Schematic illustration of secondary electrons. Secondaries are generated by inelastic collisions between the primary beam and particles in the resist, and typically travel normal to the beam.

The dependence of the secondary electron range on resist thickness and beam energy is not well-known, but evidence suggests that their range is relatively independent of both parameters.[42,43] Since the initial diameter of the beam (commonly referred to as the "spot size") also has no dependence on the resist thickness or, at least in principle, the beam energy, the spot size and secondary electrons can be thought of as a constant offset to the final PSF width, independent of the beam energy and resist system. The schematic in figure 3-7 considers all three contributors to the PSF width simultaneously, as a function of beam energy.

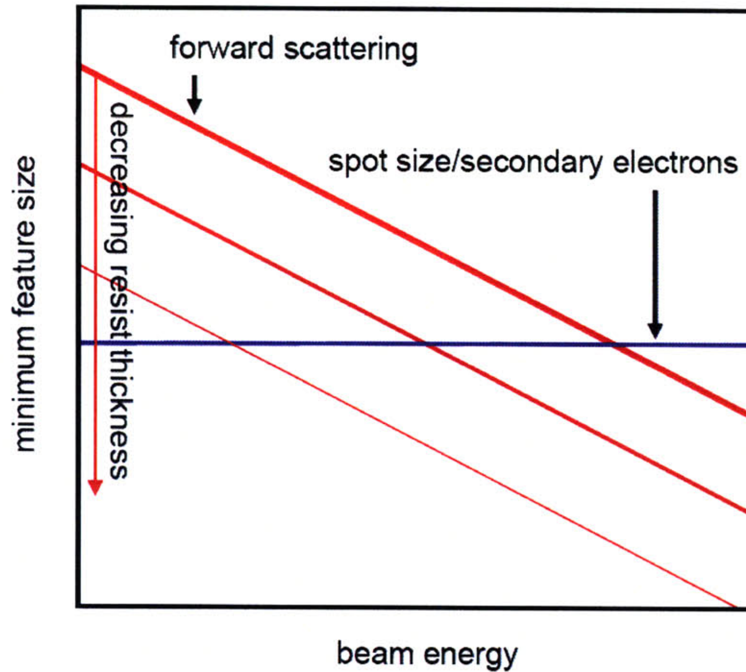

Figure 3-7: Schematic illustration of the effect of forward scattering, secondary electrons, and initial spot size on resolution. The weights of the red lines represent the relative thickness of the resist in each case. The minimum feature size at low beam energies is limited by forward scattering, while the spot size and/or secondary electrons are the primary limiter at high energies. Note that the resist thickness affects where this crossover occurs; for thinner resists, forward scattering will cease to be the resolution limiter at much lower energies than in thicker resists.

Figure 3-7 suggests a crossover point, past which forward scattering ceases to matter and, more importantly, beam energy has no effect on resolution. Further, this crossover occurs at lower beam energies when thinner resist is used.

3.3 Monte Carlo Simulation

We tested this model via Monte Carlo simulations. CASINO could not be used here, as it does not take secondary electrons into account and will not allow extraction of the deposited energy in the resist, so new software had to be written. The model we used was based on David Joy's single-scattering model;[72] the software itself was written in Visual Basic 6.0. The full source code is reproduced in appendix A.

3.3.1 Description

There are many types of interactions that can occur as an electron travels through a solid. For simplicity of programming, we employed the Bethe equation, which convolves most events that induce an energy loss in the electron without changing its trajectory into a continuous-slowdown effect.[73] As the Bethe equation was originally intended for use with high-energy particles, we were forced to use Joy and Luo's low-energy modification of it instead:[74]

$$\frac{dE}{ds} = -785\frac{\rho Z}{AE}\ln\left(\frac{1.166E + kJ}{J}\right) \tag{3.2}$$

Where ρ is the mean density of the resist in g/cm^3, Z is the mean atomic number of the resist, A is the mean atomic weight of the resist in AMU, E is the electron energy in eV, J is the mean ionization potential of the material in eV, and k is a dimensionless correction

factor empirically defined to be ~0.85. The stopping power, $\frac{dE}{ds}$, is the electron's energy loss per unit distance traveled and is expressed in eV/Å in this case.

With Bethe slowing vastly simplifying the electron energy loss in the resist, we only need to be concerned with events that alter the electron's trajectory. These can be subdivided into elastic (no energy exchanged) and inelastic (energy exchanged, secondary electron possibly produced) events, and each one has a certain probability of occurring. For elastic collisions, we use the screened Rutherford cross-section (with units of cm^2/atom) to calculate the deflection of the electron:[75]

$$\sigma_E = 5.21\times10^{21}\frac{Z^2}{E^2}\frac{4\pi}{\alpha(1+\alpha)}\left(\frac{E+511}{E+1024}\right)^2 \tag{3.3}$$

Where Z is the mean atomic number, E is the electron energy in KeV, and α is a dimensionless "screening factor" to take into account the fact that the incident electron does not "see" the full charge of an atomic nucleus because of its electron cloud. α can be approximated using the following analytical expression:[76]

$$\alpha = 3.4\times10^{-3}\frac{Z^{0.67}}{E} \tag{3.4}$$

Where Z and E are, again, the resist atomic number and the electron energy in KeV. Likewise, the Evans cross-section was used to evaluate inelastic collisions—to determine the deflection angle of the primary beam and the energy of the secondary produced:[77]

$$\sigma_I = 2.55\frac{E^2}{N_A} \tag{3.5}$$

Where E is again the incident beam energy in KeV and N_A is Avogadro's number. These cross-sections can be used to define the mean free path λ for each type of collision:

$$\lambda = \frac{A}{\sigma N_A Z\rho} \tag{3.6}$$

Where ρ is the mean density of the material in g/cm^3 and σ is the appropriate cross-section (either eq (3.5) or (3.6)). The mean free path λ has units of cm here. The total mean free path can be calculated by adding the elastic and inelastic mean free paths in reciprocal:

$$\frac{1}{\lambda_T} = \frac{1}{\lambda_E} + \frac{1}{\lambda_I} \tag{3.7}$$

And the probability of a secondary electron being produced in a collision (in other words, the probability that a given collision is inelastic) can be calculated by dividing the total mean free path by the inelastic mean free path:

$$P_{SE} = \frac{\lambda_T}{\lambda_I} \tag{3.8}$$

The resist layer was represented in the simulation as a rectangular block, with the z-axis representing depth (the beam entered the resist at $z = 0$) and the x- and y-axes representing distance from the beam axis in each direction. Each electron started the simulation at the top of the resist layer with its initial xy position determined by the initial beam distribution (a Gaussian distribution with a user-set FWHM was used). The electron was then tracked through the resist as it underwent elastic and inelastic collisions, until it escaped the film or ran out of energy. When a secondary electron was produced, tracking of the primary stopped in order to run the same algorithm on the secondary until it escaped or ran out of energy, after which tracking of the primary resumed. Figure 3-8 illustrates the tracking algorithm schematically.

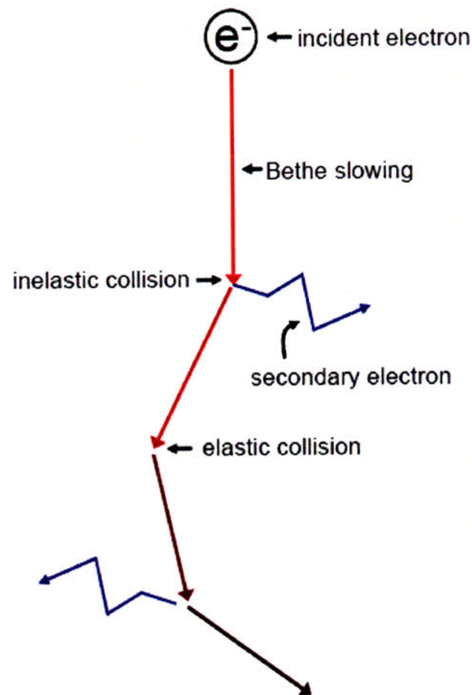

Figure 3-8: Schematic diagram of the single-scattering Monte Carlo model. As an electron travels through the resist layer, it loses energy via continuous Bethe slowing, as well as undergoing both elastic and inelastic collisions that alter its trajectory. The latter type of collisions also produce secondary electrons, which are tracked in a manner similar to the generating electron (for simplicity, no "cascade" effects were included in the model—a secondary can only undergo elastic collisions). The incident electron is tracked in this manner until it either leaves the film or its energy falls below a certain threshold, after which the program starts over with the next incident electron.

3.3.2 Results

This process was repeated over a large number (50-100K) of incident electrons, and the energy deposited throughout the resist stack (subdivided into 1 × 1 nm voxels) by each

primary and secondary electron was summed into a single matrix, giving a 3D plot of the beam's deposited energy density in the resist layer. The distribution is radially symmetric about the z axis, so it was integrated into two dimensions across the x or y axis to simplify calculation (it should be noted that integrating a non-gaussian distribution from 3D to 2D can be nontrivial, but taking a thin slice through the center of the distribution gave a nearly identical 2D distribution to that obtained by integrating). Since the PSF is broadest at the base of the resist stack, only the bottom row of this 2D distribution was taken into account in order to get a "worst-case scenario" 1D PSF. The resulting one-dimensional function was plotted using MATLAB as shown in figure 3-9. Since no single function accurately fit the PSF data taken at all energies and resist thicknesses, the FWHMs of the plotted PSFs were simply calculated graphically.

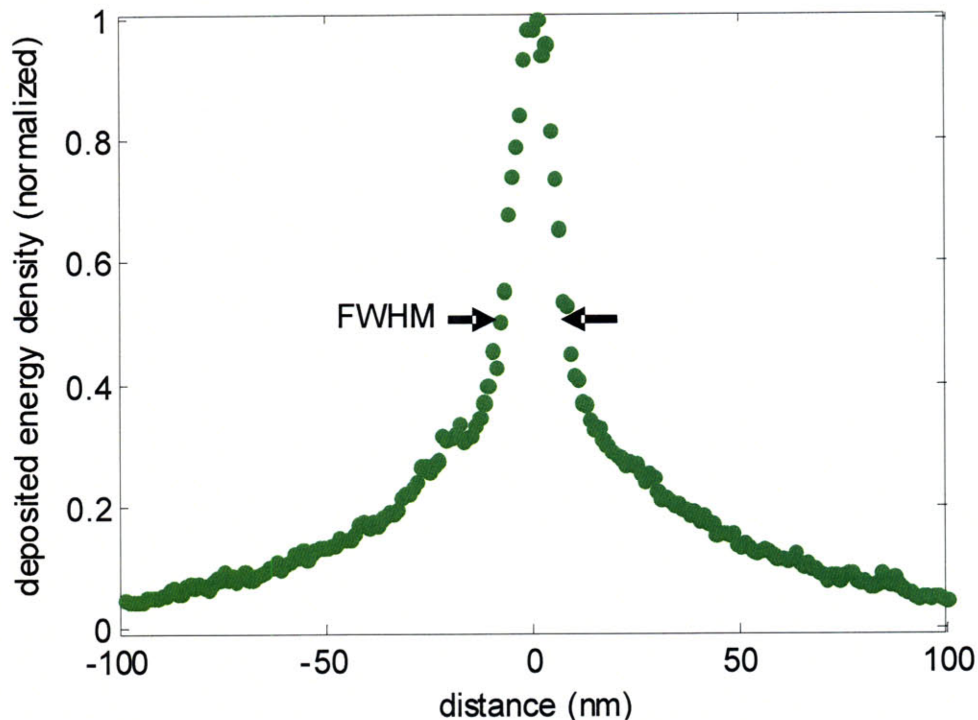

Figure 3-9: Example 1D energy-density plot extracted from the Monte Carlo simulations described above. The beam energy used for this data set was 20 KeV and the resist (HSQ) thickness was 100 nm; the distribution shown here was extracted from the bottom of the HSQ layer. The FWHM of the distribution is marked on the figure and is approximately 20 nm in this case.

These simulations were run for HSQ layers ranging from 25 to 250 nm thick, at beam energies from 10 to 100 KeV. No substrate was included in the simulations so backscattering was not taken into account, but as previously noted backscattering typically occurs over a length scale of microns and has little effect on our measurements at the nanometer scale. The initial beam diameter in all cases was assumed to be 5 nm, a

conservative estimate of the beam diameter in our Raith-150 tool. The combined results of all of these simulations are plotted in figure 3-10.

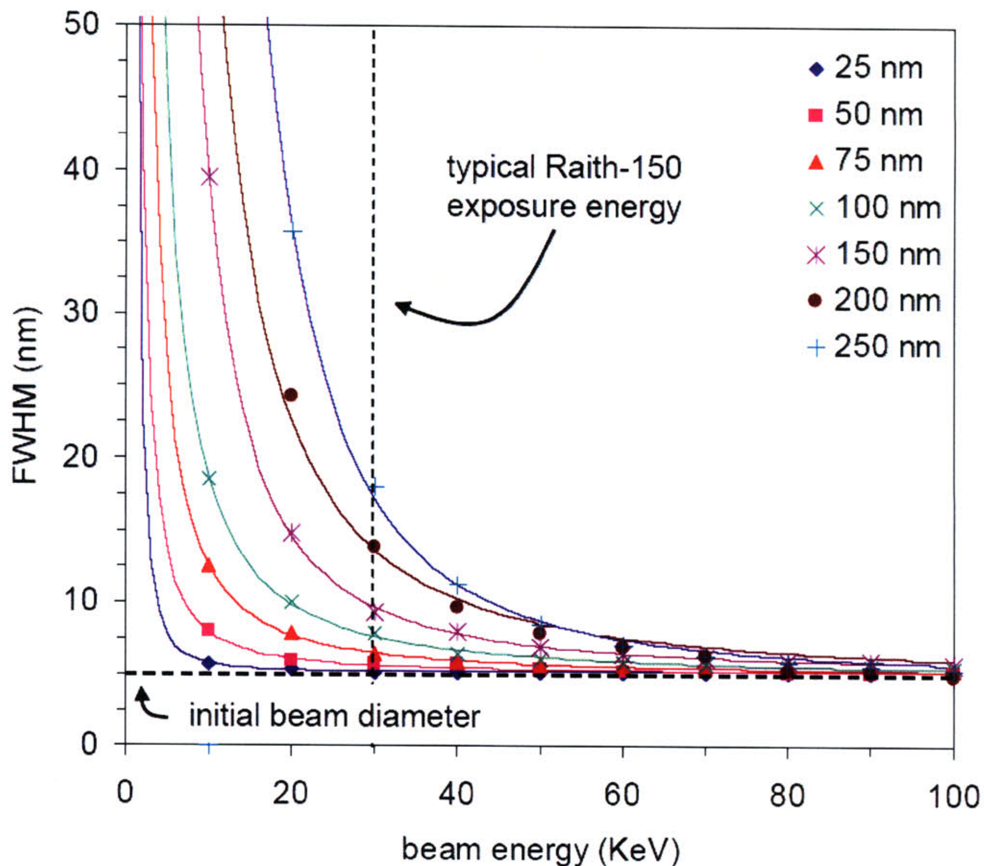

Figure 3-10: FWHM measurements for the deposited-energy distribution point-spread function at the base of HSQ layers of varying thickness, as a function of beam energy. The initial beam profile is assumed to be Gaussian with a FWHM of 5 nm here, and the vertical dotted line marks our typical exposure experimental exposure energy of 30 KeV. For low energies and/or thick resists, forward scattering substantially broadens the PSF, but as the beam energy is increased and/or the thickness is reduced, the FWHM collapses to nearly the initial beam diameter. Secondary electrons, interestingly, seem to have little to no effect on the PSF width, a result which contradicts conventional wisdom.

The data in 3-10 agrees qualitatively with the more simplified result in figure 3-5 and validates our earlier assumptions about the resolution limits of SEBL. At low beam energies, the point-spread function is broadened by forward scattering, but past a certain critical beam energy this becomes a nonissue and the final PSF closely matches that of the incident beam. This crossover point is a function of resist thickness as illustrated in figure 3-11; forward scattering ceases to be an issue at much lower energies when thin resist is used. Interestingly, the "dc offset" effect we expected to observe due to secondary electrons (all of the data points being shifted upward 3-6 nm from the initial beam diameter due to broadening from the secondary electrons) is not apparent, suggesting that at least in this simplified treatment secondary electrons do not significantly affect the final beam diameter.

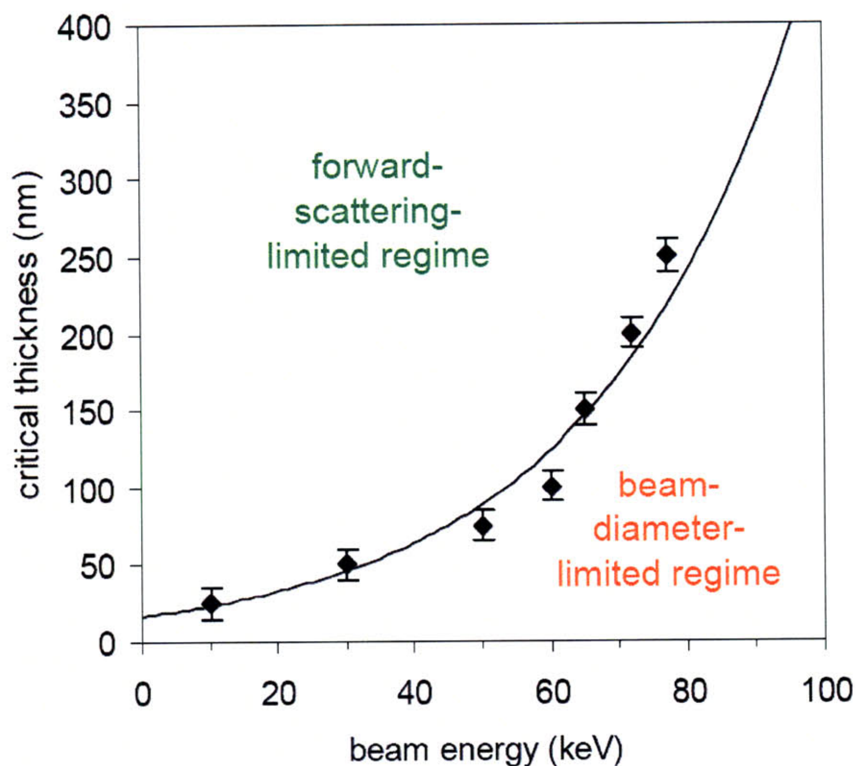

Figure 3-11: "Critical thickness" of resist as a function of beam energy, as extracted from the data in figure 3-10 (the solid line is a generic fit function to serve as a visual aid). At resist thicknesses above the critical thickness, forward scattering limits resolution, whereas below the critical thickness the only resolution limiter (when considering only the exposure process, at any rate) is the beam diameter, which is at least theoretically energy-independent.

The most important conclusion to draw from figure 3-11 is that, below the critical thickness, the final beam point-spread function (and as a result the exposure resolution) is dependent only on the initial beam diameter. Since the beam diameter is, in principle, independent of beam energy in a good SEBL system (we will see later that this is not exactly true in practice), this means that *beam energy is irrelevant as long as it is high*

enough to keep the resist thickness below the critical thickness! This means, for example, that it should be possible to get near-identical resolution in a 50 nm HSQ stack using a 100 KeV SEBL system and an inexpensive 30 KeV system (assuming the beam diameters are similar). This conclusion contradicts the conventional wisdom that high beam energies are absolutely necessary for high resolution.

Since figure 3-11 takes into account only the distribution of the energy deposited in the resist by the beam, it suggests some obviously spurious conclusions (at 100 KeV, it should be possible to yield a feature as wide as the 5-nm incident beam and over 400 nm high!). This is because we are ignoring, at least for now, the mechanical practicalities of actually developing away the resist and creating a free-standing pattern from the latent image generated during exposure. Maximum height of structures is generally aspect-ratio-limited; that is, it is typically impossible to develop structures whose height is more than a certain multiple of their surface area. The maximum achievable aspect ratio will vary with choice of resist and developer, development processing (e.g. the use of ultrasound or critical-point drying), and a host of other factors. An in-depth analysis of aspect ratio limitation and optimization is beyond the scope of this discussion, but a conservative estimate of a reasonable aspect ratio is ~10:1, meaning our 5-nm-wide feature could in actuality be no more than 50 nm tall in order to survive the development process.

3.4 Experimental Verification

In order to verify the conclusions drawn from the Monte Carlo simulations in the previous section, we decided to experimentally test the resolution limit of our SEBL system. Hydrogen silsesquioxane (HSQ), a negative electron resist, was used in all of these experiments, due to its high resolution and ability to withstand direct SEM analysis (unlike PMMA). By using Yang et al's high-contrast "salty development"[14] process and writing dense and isolated structures simultaneously, it should be possible to estimate the point-spread function at various energies and resist thicknesses and see if the results agree with our simulations.

3.4.1 Description

The SEBL tool used in our experiments was MIT's Raith-150 system, which has a maximum exposure energy of 30 KeV. As this beam energy is lower than more costly tools are capable of, we used very thin (~25 nm) HSQ layers on Si substrates to compare resolutions at 10, 20, and 30 KeV; 25 nm should be at or below the critical thickness indicated in figure 3-11 in all three cases. Our resolution test structures, shown in figure 3-12, were "nested-L" structures of pitches ranging from 2 nm to 100 nm.

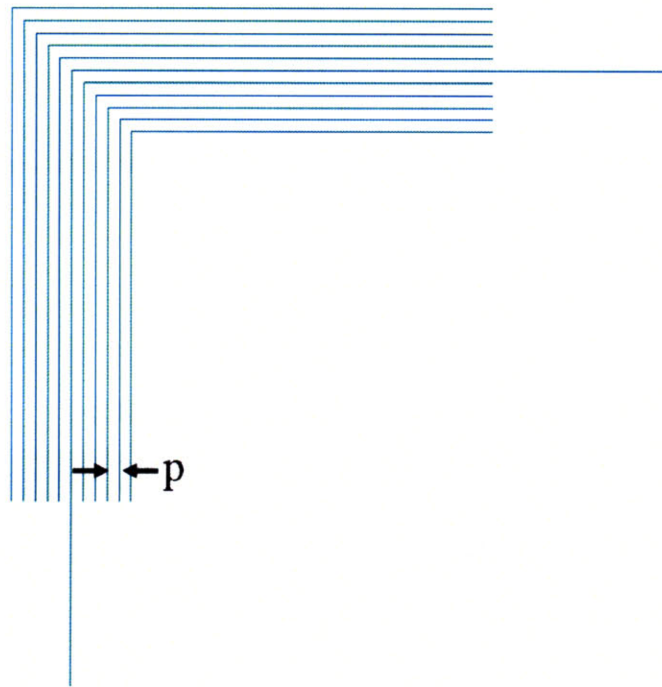

Figure 3-12: Example "nested-L" structure consisting of single-pixel lines with pitch p. The structure allows simultaneous evaluation of dense and isolated lines along the x and y axes, as well as corner structures.

Since exposure doses vary with acceleration voltage, dose arrays of nested-L structures were exposed in 25 nm of HSQ on Si at 10, 20, and 30 KeV. The HSQ was then developed for 4 minutes in a 1% NaOH/4% NaCl aqueous solution, rinsed in de-ionized water and isopropanol, and dried with nitrogen. The HSQ structures were then directly imaged in a scanning electron microscope; a thin layer of Au-Pd was sputtered onto the surface of the sample to improve SEM imaging.

3.4.2 Results

Figure 3-13 shows a broad array of structures resolved at various pitches and acceleration voltages.

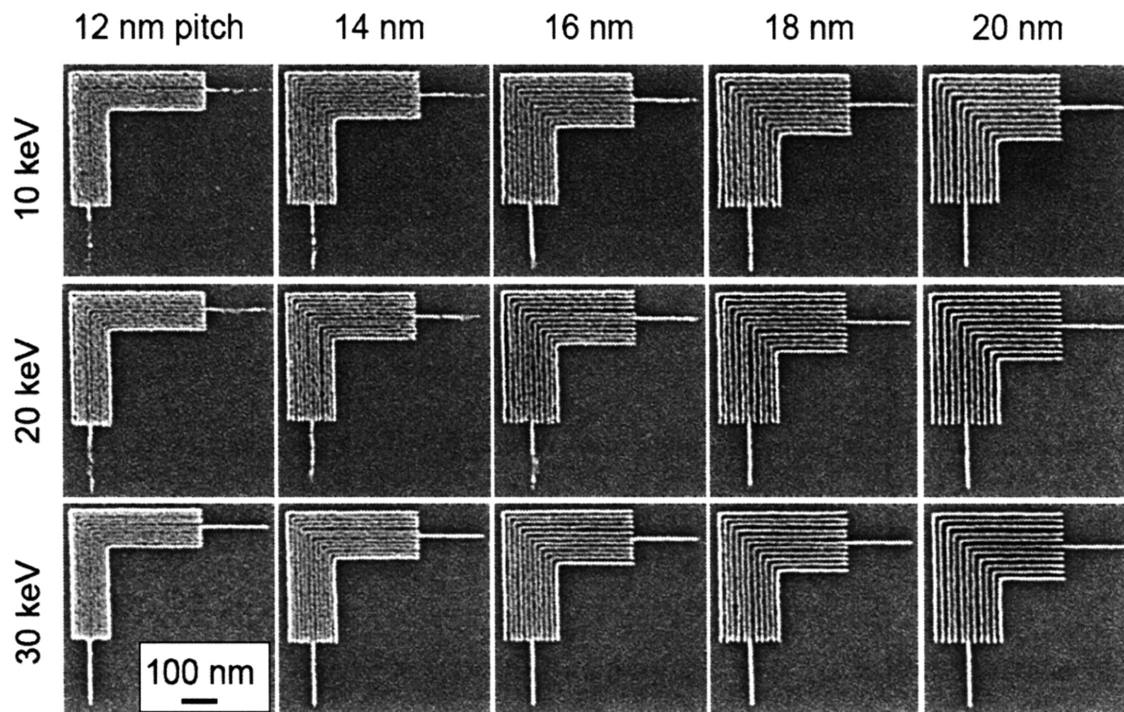

Figure 3-13: Scanning electron micrographs of nested-L structures with pitches ranging from 12 nm (the smallest yielded at any voltage) to 20 nm, exposed at 10, 20, and 30 KeV. While there is some resolution degradation at lower acceleration voltages for the smaller pitches, it is minimal and, at 16 nm and above, almost completely absent.

This data appears to validate the critical thickness theory; when resist this thin is used, the variation in resolution at 10 KeV and 30 KeV is minimal to nonexistent. Figures 3-14 and 3-15 provide a closer look at some of the micrographs in 3-13.

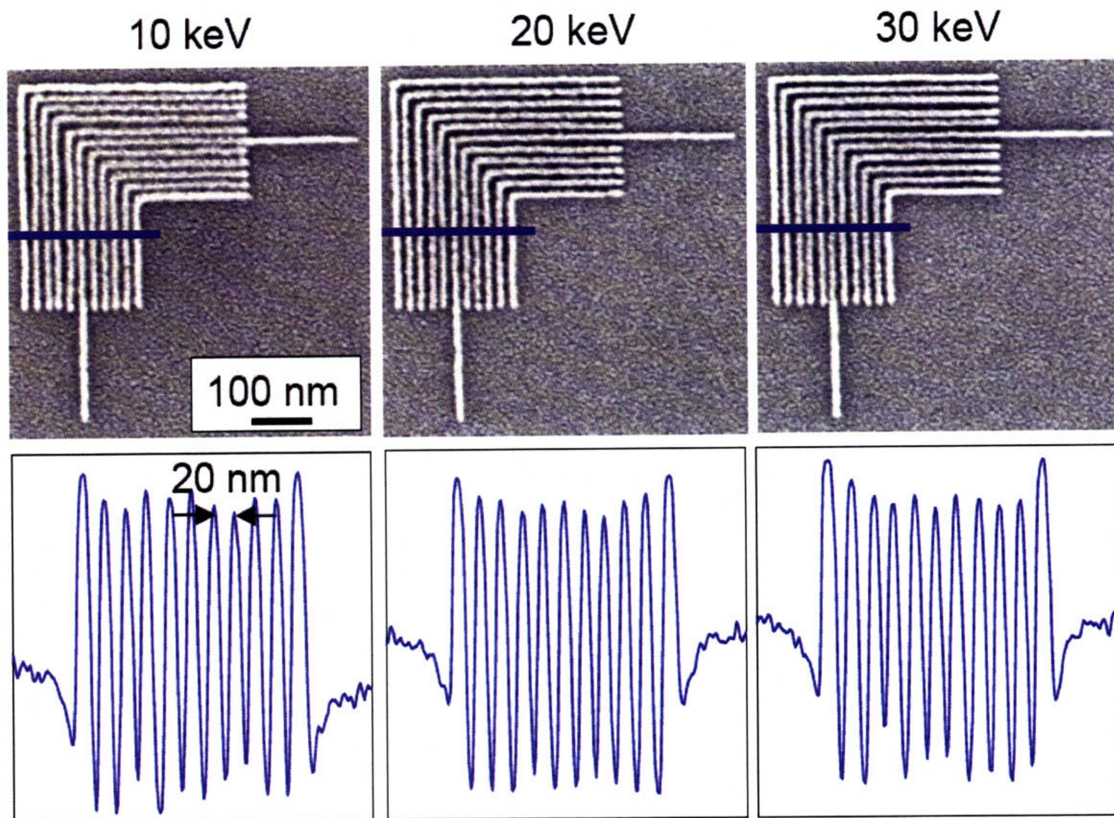

Figure 3-14: Expanded view of 20-nm-pitch (10-nm-linewidth) nested-L structures fabricated at 10, 20, and 30 KeV. The plots below each micrograph are averaged cross-sectional line scans (indicated by the blue line on the micrograph) to illustrate the modulation in each image. At this feature size, modulation is full and even in all three cases and any resolution variation with acceleration voltage is essentially undetectable.

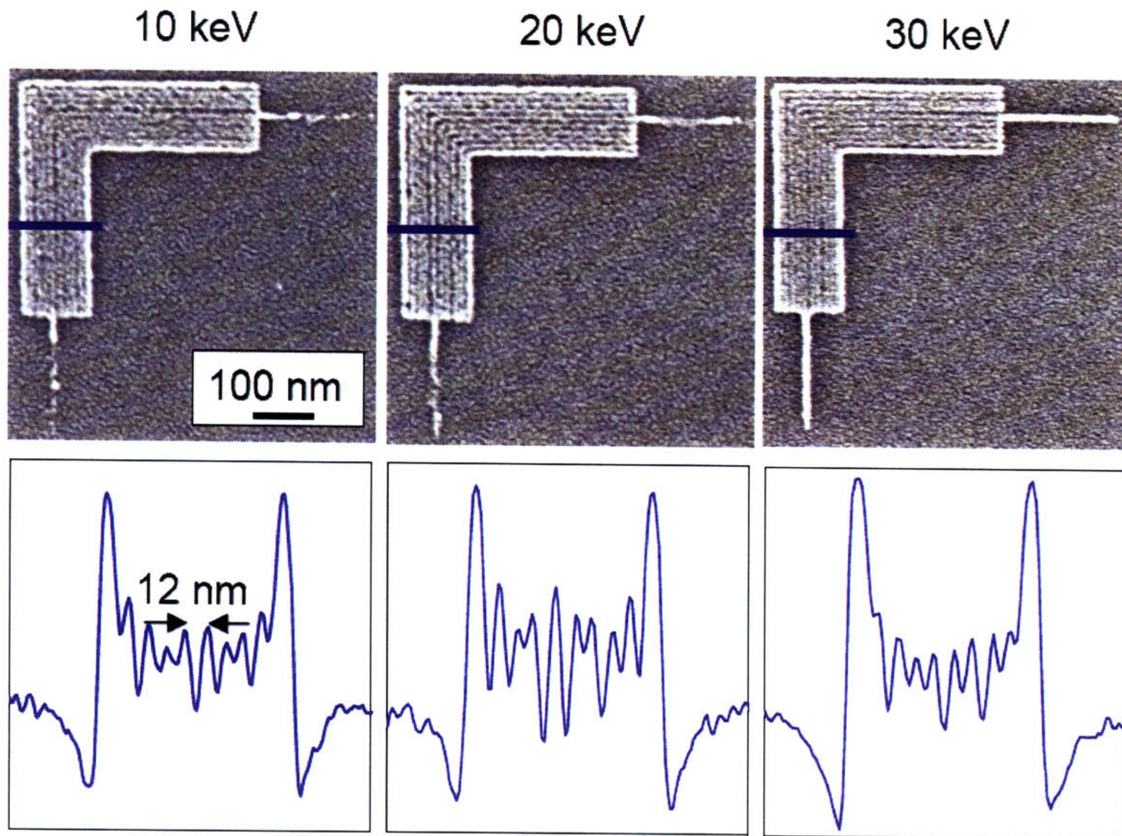

Figure 3-15: Expanded view of 12-nm-pitch (6-nm-linewidth) nested-L structures fabricated at 10, 20, and 30 KeV, with averaged linescans below each image showing the modulation in the pattern. At this feature size (the smallest yieldable on our Raith-150) there are some minor resolution variations present, visible mostly as difficulty yielding both the dense and isolated features at 10 and 20 KeV. Still, even at 10 KeV there are traces of the isolated lines and clear, if uneven, modulation in the dense region, suggesting that our resist thickness is probably just above the critical thickness at 10 and 20 KeV.

An additional advantage of patterning at low voltages was an increase in throughput.[18,31] Electron stopping power, according to equation (3.2), is inversely proportional to electron energy. Lower-energy electrons, as a result, will deposit energy in the resist much more

efficiently than high-energy electrons. The result is that a lower electron dose is needed to deposit enough energy to expose the resist. This effect is somewhat mitigated by the fact that the electron beam current in our Zeiss Gemini column tends to be slightly lower at low acceleration voltages. Figure 3-16 shows, however, that exposing at 10 KeV reduces the critical pixel dwell time (the minimum time the beam needs to dwell on a pixel in order to expose it) by nearly a factor of two over a 30 KeV exposure, even taking the reduced current into account. The ability to pattern at low beam currents has other advantages beyond throughput, such as high-resolution patterning using low-voltage microcolumn/multibeam SEBL schemes.[17,78-80]

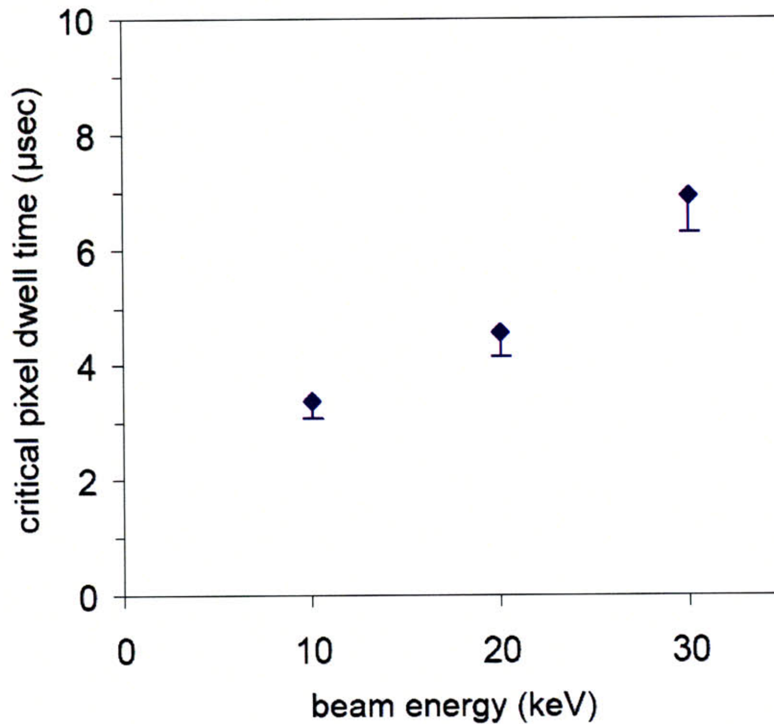

Figure 3-16: Critical pixel dwell time (the minimum time the beam needs to dwell on a pixel in order to expose it) as a function of beam energy, calculated from the beam currents and electron doses used in figures 3-13-3-15. The error bars here represent the uncertainty in deriving a critical dose from a single element in a dose array. Even taking into account the lower beam current at 10 KeV (which we have done here), the critical dwell time is nearly a factor of two lower than it is at 30 KeV, resulting in a nearly 2× increase in throughput when writing at 10 KeV.

The minimum pitch at which we were able to simultaneously yield dense and isolated features (at any beam energy) was 12 nm. According to the calculations in figure 3-3, this result suggests that our point-spread function has a FWHM of approximately

10-12 nm. Further, since we are operating in the voltage/thickness regime where beam diameter is the determining factor in PSF width, this result suggests that the beam diameter in our system is approximately 10-12 nm, more than a factor of two higher than the specified diameter of 3-4 nm. As a sanity check, we decided to measure the beam diameter of the Raith-150 directly.

3.5 Beam Diameter Measurement

The effective beam diameter of our system, according to our best experimental estimates in the previous section, is approximately 12 nm. Raith, however, specifies the diameter of the beam at 3-4 nm. Since there is significant discrepancy between the two numbers, it seems likely that some other factor not accounted for in our assumptions and models is degrading our resolution. One possibility is that the spot size of our particular tool, for whatever reason (possibly vibrations in the system), is actually significantly larger than specified. In order to test this theory, we decided to measure the beam diameter directly and compare the result to our inferred measurement of the diameter in the previous section.

3.5.1 Procedure

Our method for measuring the beam diameter was a variation on the standard ASTM procedure for characterizing scanning electron microscopes.[44] Our measurement sample was a standard gold-on-carbon SEM characterization sample purchased from Ted Pella,

Inc. Our method operated under the assumption, illustrated in figure 3-17, that a Gaussian-profile beam scanned in a line over an edge approximated as a step function would produce a SEM signal that was a convolution of the two shapes. In principle, the width of the Gaussian beam could be deconvolved by measuring the linescan produced by the SEM.

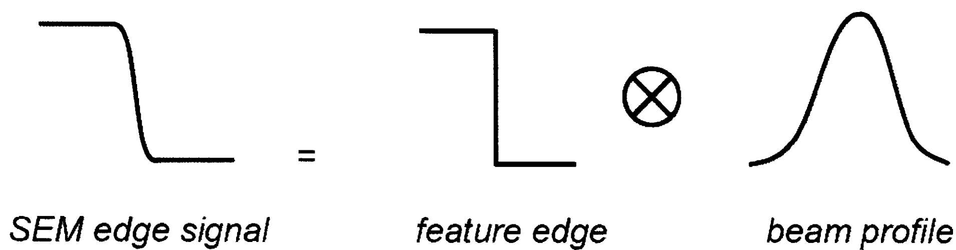

Figure 3-17: Illustration of the method of determining the beam profile by deconvolving it from SEM linescans over edges assumed to be step functions.

In practice, the feature edges on our test sample were not perfect step functions, so this measurement was likely to be biased slightly high. This was acceptable, however, since the measurement was only being used as a first-order diagnostic to check for gross variation; only a reasonable approximation of the beam diameter was needed. Figure 3-18 illustrates the measurement process: a high-magnification image was taken of the test sample, the brightness and contrast were adjusted to ensure that the image was not saturated and three linescans each were taken over edges in the x and y directions. This was repeated for 30 images for each voltage measured, in order to minimize random errors originating from irregular edge shapes and other sources. The linescans were processed with a moving-average filter to remove noise, then measured by taking the

distance between the points of 80% maximum value and 20% maximum value on the slope, which was calculated to be ~71% of the beam's FWHM.

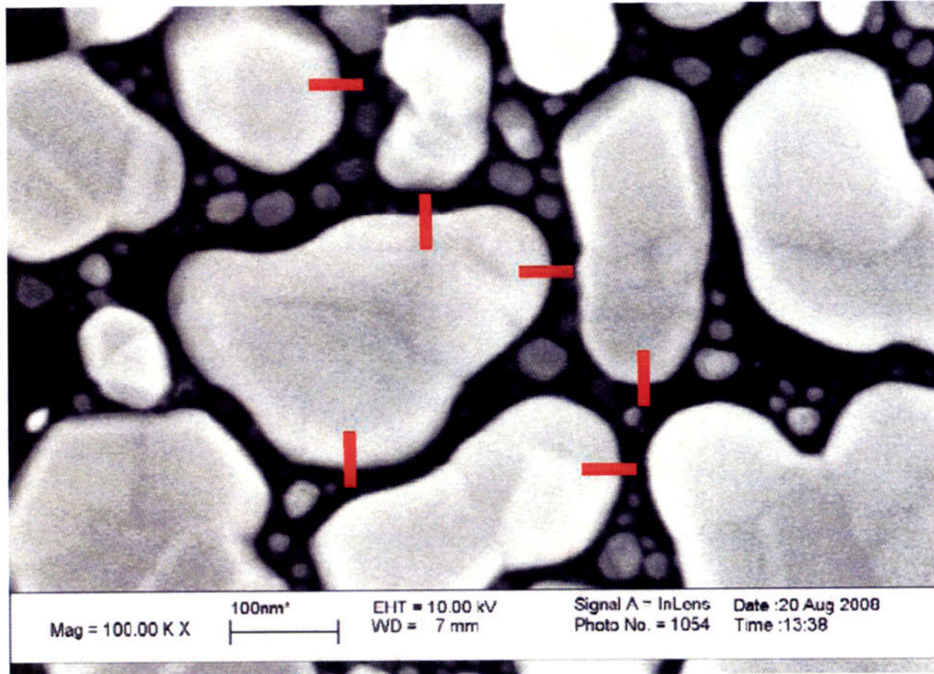

Figure 3-18: High-magnification image of the gold-on-carbon test sample, with the linescans measured on this particular image marked in red. Each linescan was processed with a moving-average filter in order to reduce noise, then the linear distance between the points of 80% and 20% of maximum brightness on the slope was measured and used to deduce the beam diameter.

3.5.2 Results

The results of these measurements at acceleration voltages of 1, 5, 10, and 20 KeV are plotted in figure 3-19. The 30 KeV diameter, unfortunately, could not be measured because the in-lens secondary electron detector in the Raith-150 does not work at this

voltage, making noise-free measurements impossible. Still, the beam diameter at 30 KeV can be reasonably extrapolated from the data we were able to obtain.

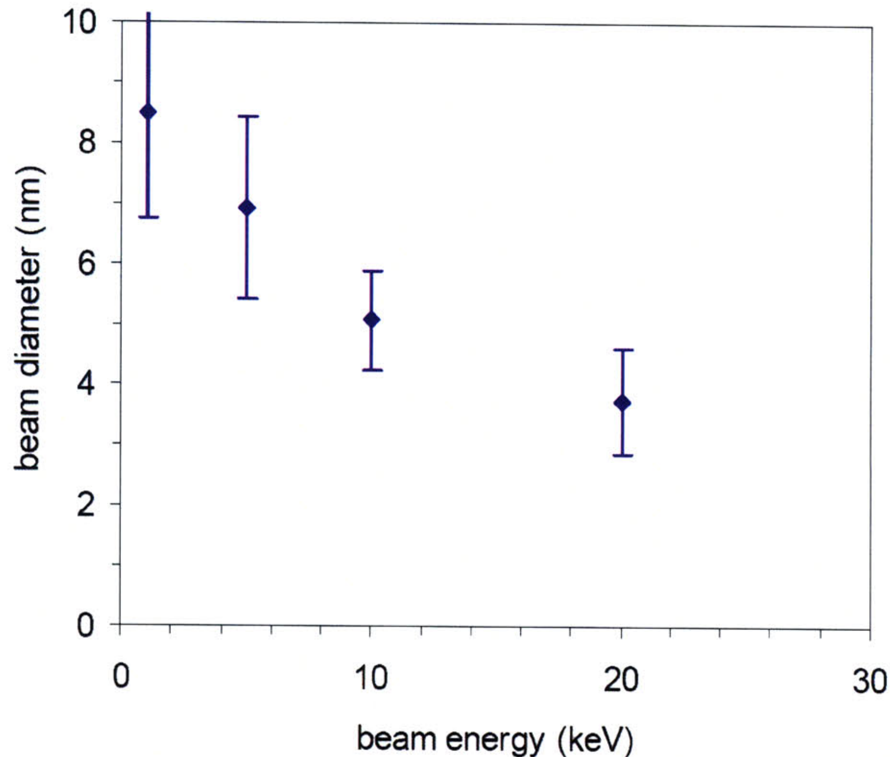

Figure 3-19: Beam diameter as a function of beam energy as measured in the MIT Raith-150 system (the 30 KeV data proved impossible to obtain due to an inherent high-voltage imaging issue with the system). Each data point represents 90 linescans in the x direction (the data from the y direction scans was identical to within the margin of error). While the beam diameter is inexplicably large at voltages below 10 KeV, it seems to be reasonably close to its 3-4 nm specification at 20 KeV and only slightly larger at 10 KeV, suggesting that beam diameter is not the limiting factor in our resolution.

Large spot size at sub-10-KeV voltages aside, these results appear to be reasonably within the specification of the Raith-150. Based on this data, beam diameter does not seem to be the final limiting factor in our resolution.

3.6 Imaging Limitations

Another possible reason for the discrepancy in measured beam diameters is that the *imaging* resolution of the Raith-150 is substantially lower than its *lithographic* resolution. A possible explanation for this is environmental noise and its effect on tool performance. When the Raith is writing patterns, the beam dwell time on a single pixel is typically on the order of 1 μs. At these beam speeds, the bandwidth of environmental noise capable of distorting or "blurring" patterns is on the order of 100 KHz-1 MHz or larger. While ambient electromagnetic noise at these frequencies is certainly present in the Raith's vicinity (due to computers and other electronics), the multiple layers of metal shielding around the system's main vacuum chamber should effectively screen out high-frequency electromagnetic noise.

Imaging is another issue entirely. When the Raith is being used for imaging, the system is scanning the beam comparatively slowly and is consequently vulnerable to electronic and acoustic noise in the 1 Hz-1 KHz range. These low-frequency vibrations can be extremely difficult to compensate for, and the result is an imaging resolution that is limited by system noise, rather than beam diameter. As an example of this, figure 3-20 shows micrographs of a 9-nm-pitch nested L structure, one taken in the MIT Raith-150

and one taken on Raith's prototype 150^{TWO} tool, which is housed in a relatively vibration-free environment. The difference in the two images is striking; in the MIT tool, there is no visible modulation, while the 150^{TWO} is able to clearly show the feature's discrete lines. This result suggests that, due to vibration issues affecting the imaging capability of our tool, we may be fabricating structures smaller than we are able to image.

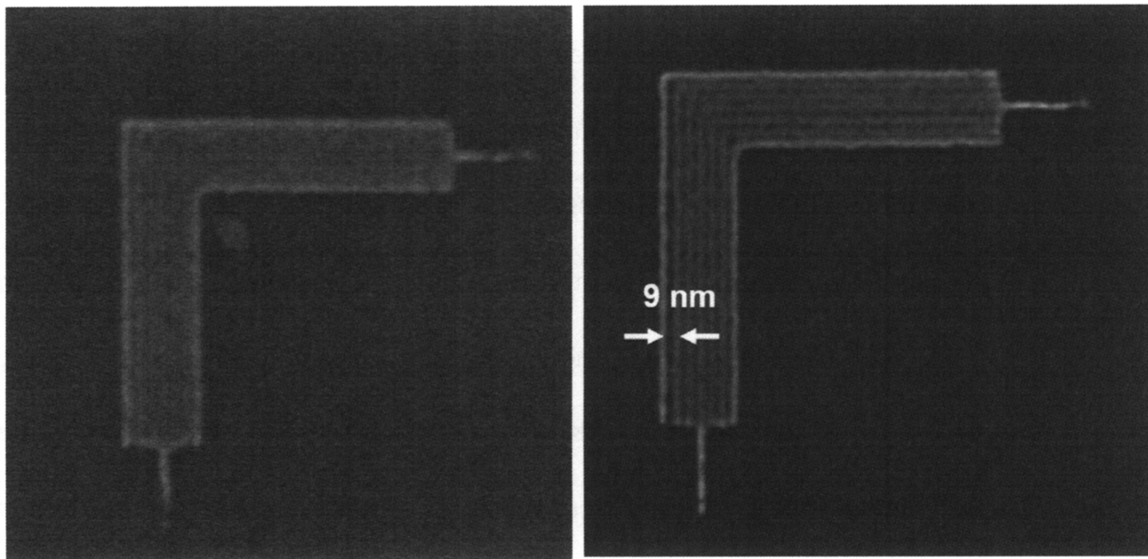

Figure 3-20: 9-nm-pitch nested-L structure fabricated in HSQ on Si and imaged in the MIT Raith-150 system (left) and on the Raith-150^{TWO} prototype tool at Raith headquarters in Germany. The left image shows minimal to nonexistent modulation, while the discrete lines of the structure are clearly visible in the right image. Since the 150^{TWO}'s environment has much better vibration isolation and control than the MIT facility, it seems likely that low-frequency vibrations are a significant source of imaging resolution degradation on the MIT tool. (right micrograph courtesy J. Yang and Raith GmbH)

3.6.1 TEM Analysis

In order to answer the imaging-vs.-lithographic resolution question definitively, we fabricated several samples on Si_3N_4 membranes and imaged them using transmission electron microscopy (TEM). The resolution of TEM is typically on the order of angstroms, so even the smallest structures we were able to fabricate using SEBL should be easily visible.

3.6.1.1 Sample Preparation

Since TEM analysis requires a sample thin enough that high-energy electrons can pass through it, our HSQ structures had to be fabricated on a 50-nm-thick silicon nitride (Si_3N_4) membrane, rather than the usual Si substrate. This necessitated some changes to our standard fabrication process.

We used commercially-available Si_3N_4 membranes 250 μm in diameter, surrounded by a Si frame approximately 5 mm wide. In order to spin-coat the membranes with 20 nm of HSQ, they were temporarily affixed to a Si wafer using a piece of flexible plastic cut from the base of a "gel-pak" sample holder, as the samples are too small to mount directly on the spin-coater chuck; this assembly is illustrated in figure 3-21.

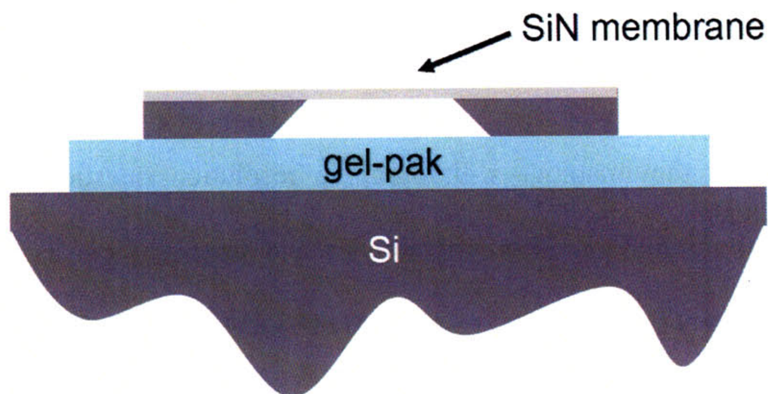

Figure 3-21: Mounting scheme for spin-coating and developing Si_3N_4 membranes for TEM analysis. A piece of flexible plastic cut from a "gel-pak" sample holder is mounted on a piece of silicon. The membrane is then attached to the plastic, enabling it to be processed like a standard-sized sample. The size of the membrane in this schematic is exaggerated for clarity; it is actually much smaller than the silicon mount.

When exposing the samples in the Raith, care had to be taken to avoid trapping air under the membranes when mounting them, as trapped air would cause the membranes to shatter during system pumpdown. To avoid this, we suspended the samples between two strips of carbon tape to allow any air under the membranes to be evacuated during pumpdown; this scheme is illustrated in figure 3-22.

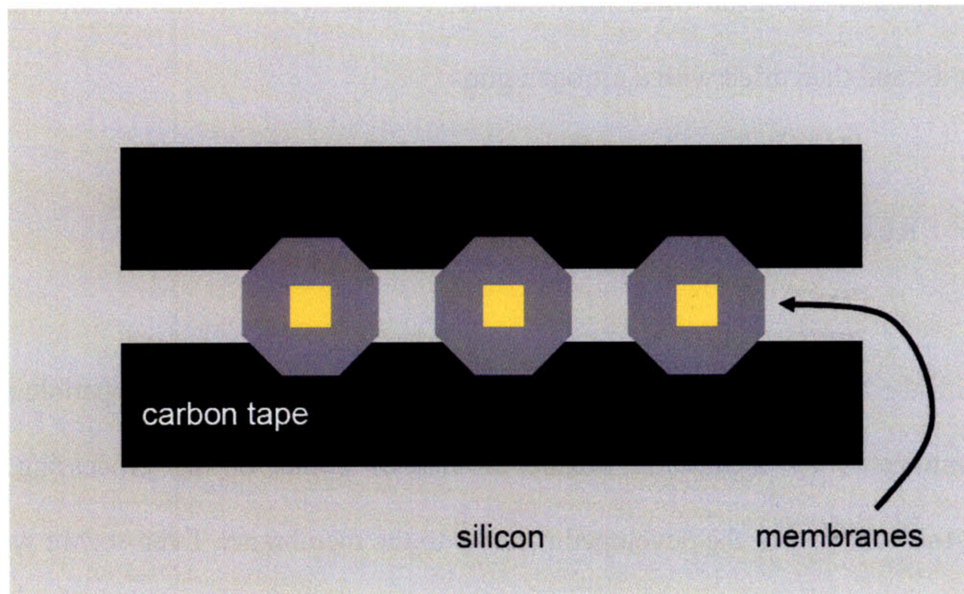

Figure 3-22: Illustration of suspended-mounting scheme for membranes, designed to ensure that the membranes do not rupture under vacuum. The membranes are suspended between two strips of carbon tape attached to a piece of silicon. The membranes are thus raised approximately 1 mm above the silicon surface, allowing air under the membranes to escape during vacuum, rather than blowing out the membranes.

Development presented a similar issue, as the membranes are extremely difficult to handle without damage during standard immersion-development processing. To minimize handling problems, we again mounted the membranes on a flexible plastic film attached to a Si wafer. In order to avoid developer contamination, the sample-mounting assembly was fully cleaned with isopropanol, rinsed in the developer solution, and dried with a nitrogen gun prior to mounting. Once the membranes were attached, the entire assembly was immersed in a solution of 1% NaOH/4% NaCl solution for 4 minutes,

cascade-rinsed in deionized water for 1 minute, cleaned by immersion in isopropanol for 30 seconds, and then dried with a nitrogen gun.

3.6.1.2 Results

Even with the above modifications, the process of fabricating TEM-compatible samples was complicated by membrane flexure at various points during processing, which affected the adhesion of the developed patterns to the membrane. Even so, we were able to obtain micrographs of some samples at resolutions far above those of scanning electron microscopy, as figure 3-23 illustrates. The samples were imaged using a JEOL 2010 TEM with an acceleration voltage of 200 KeV and a nominal resolution of 1.6 Å.

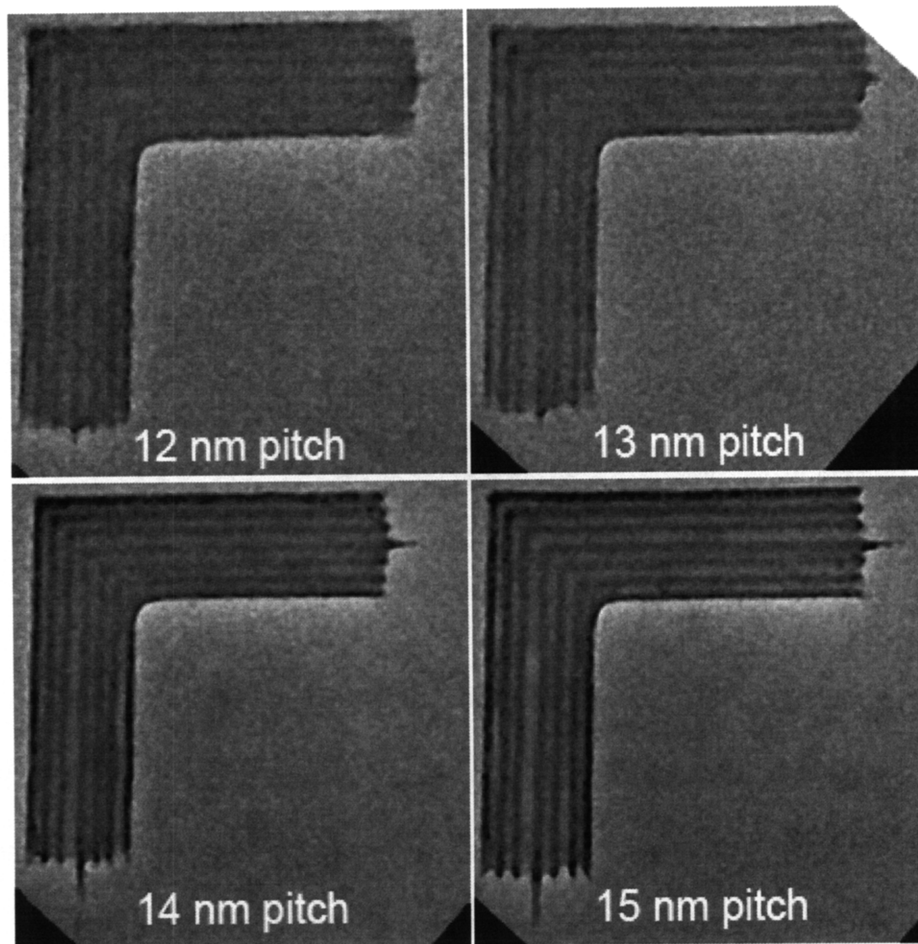

Figure 3-23: Transmission electron micrographs of several 20-nm-thick HSQ "nested-L" structures fabricated on a 50-nm-thick Si_3N_4 membrane. The triangles at the edges of the images are an artifact caused by cropping and rotating the original images. While the imaging resolution is much higher than on a typical SEM (evidenced by the visible line-edge roughness, footing around the lines, and texture on the membrane itself), the observed lithographic resolution is approximately equal to the SEM results in figure 3-13, with 12 nm being the lowest pitch at which any modulation was visible. This result suggests that limitations in our SEM imaging are not the reason our observed maximum resolution is so much lower than the calculated theoretical maximum. (Micrographs courtesy H. Duan)

As the smallest features we were able to image using a TEM were approximately the size of our best SEM results (5 nm structures, corresponding to a pitch of ~10 nm), we concluded that issues with SEM imaging, while possibly accounting for a nanometer or two of "lost resolution," were not the reason our minimum achievable real-world resolution was so much lower than theoretical predictions.

3.7 HSQ Development

With beam diameter and imaging resolution ruled out as the cause of our "missing resolution," we were forced to look beyond the exposure process for an explanation. HSQ being the resist used in the vast majority of our resolution experiments, the logical next step was to investigate the development mechanics of HSQ.

3.7.1 Development Rate

Unlike PMMA and most other resists, HSQ has a highly nonlinear development rate. We measured the time-dependence of the HSQ development rate by using thick (~150 nm) HSQ layers, exposing large areas to specific electron doses, developing for times ranging from 15 seconds to 16 minutes, and measuring the resist developed away using a Dektak profilometer. The results of this experiment are shown in figure 3-24.

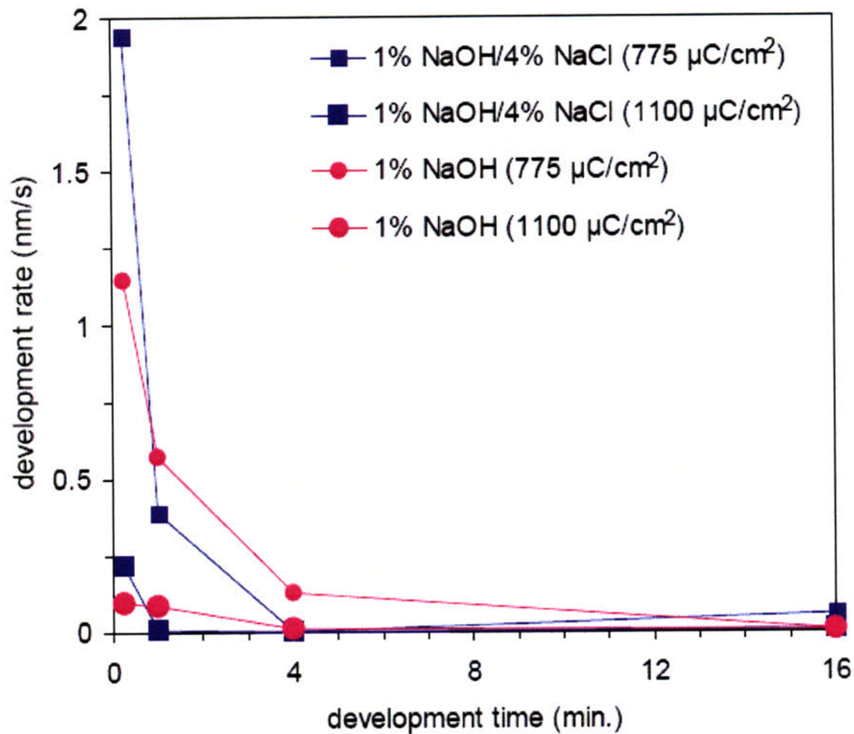

Figure 3-24: HSQ development rates in both "salty" (4% NaOH/1% NaCl) and "nonsalty" (4% NaOH) developer as a function of time, for two different electron doses. The development rate falls off rapidly as a function of time; after one minute, even the fastest resist-developer combination has slowed by nearly a factor of ten, and by four minutes the development rate is negligible. The cause of this development rate reduction is unknown, but thought to be the result of a charge-screening layer building up on the resist surface and inhibiting developer access.[14] (Data courtesy J. Yang)

While the cause of this nonlinearity is currently a matter of some debate, in a practical sense it means that very little HSQ development takes place after the first minute of developer immersion. This introduces a time-critical element to the development process; in order for a given feature to yield, it must be capable of fully developing in one minute or less.

3.7.2 Diffusion-Limited Development[81]

This time-dependence is an issue because, particularly at the length scales of interest to us, development rate is most likely diffusion-limited and thus very dependent on the geometry of the features being developed. The relative effects of reaction rate and developer diffusion on overall development rate are discussed in detail in section 4.5, but a simplified version of the same model can be used in this case, at least to make a qualitative argument.

By measuring the development rate of HSQ at various temperatures, we were able to determine that, like the PMMA development reaction, HSQ development is a first-order reaction with an Arrhenius-like temperature dependence as shown in figure 3-25.

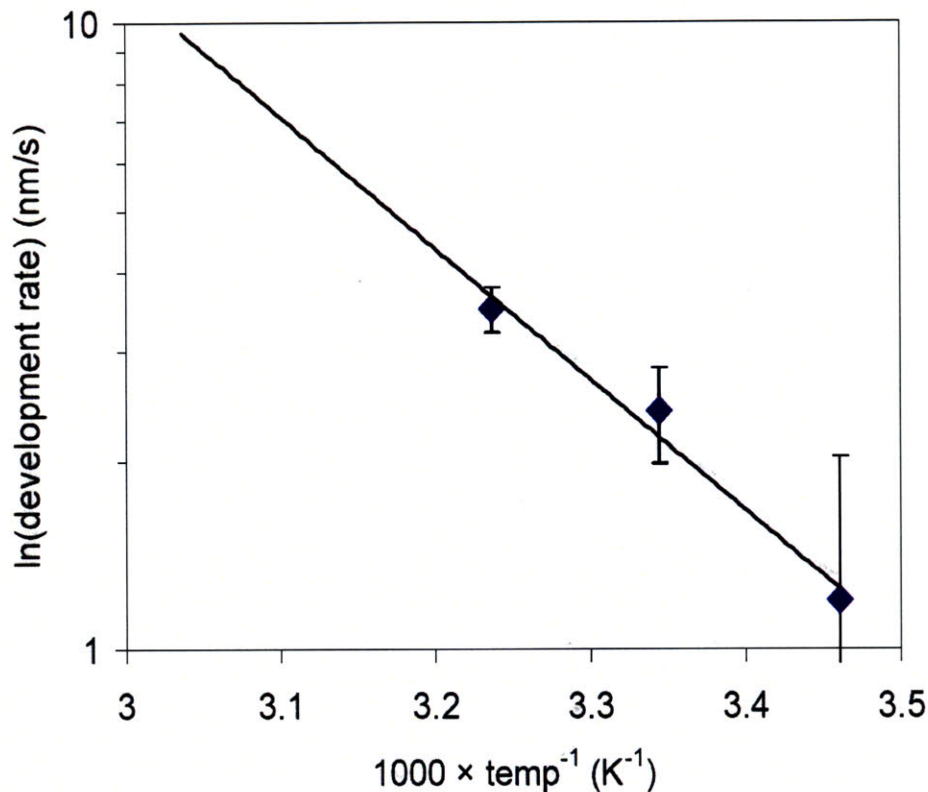

Figure 3-25: Arrhenius plot of HSQ development in 1% NaOH/4% NaCl as a function of temperature. The error bars in this case represent the uncertainty in the development rate. The straight-line dependence exhibited when the natural log of the development rate is plotted vs. the inverse of the temperature indicates that the development reaction can be modeled as a first-order reaction, simplifying characterization.

With this in mind, we can model the removal of resist from a small gap in an HSQ layer as an electrical circuit, as illustrated in figure 3-26. Again, a much more detailed version of this procedure described in section 4.5, which can be referred to for a more detailed description of each component of the model used here.

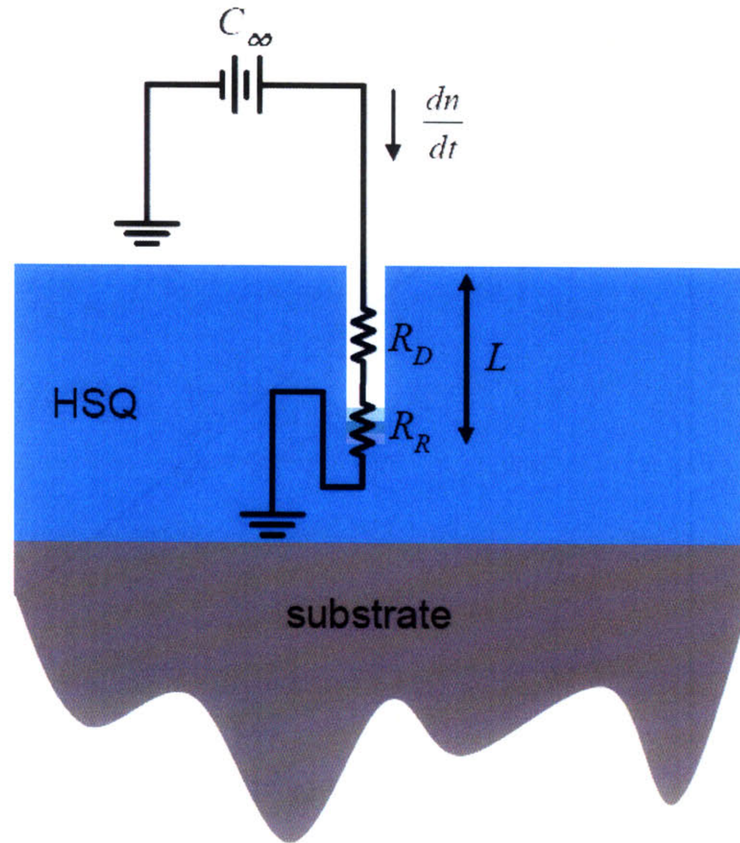

Figure 3-26: Schematic illustrating the modeling of the development of a small gap in an HSQ film as a circuit diagram. The potential in this case is C_∞*, the bulk developer concentration. The current is* dn/dt*, the flux of developer into the feature. The two resistors,* R_D *and* R_R*, represent the restrictions on the development rate due to the rate of developer diffusion into the reaction site and the rate of the development reaction itself, respectively. the distance* L *represents the length of the developed gap; the overall development rate can be represented as* dL/dt.

Each of the elements in the circuit is analogous to a development parameter. the voltage represents C_∞, the bulk developer concentration. The flux of developer into the feature, *dn/dt*, is represented by the current. The two main restrictions on the development rate (the diffusion of the developer into the feature to the reaction site and the rate of the

development reaction itself) are represented by R_D and R_R, respectively. Since the development reaction is first-order, we can write:

$$\frac{dn}{dt} = k_1 C_i A = \frac{C_i}{R_R} \tag{3.9}$$

Where k_1 is a reaction rate constant, A is the cross-sectional area of the gap, and C_i is the developer concentration at the reaction interface. R_R, then can be defined as:

$$R_R \equiv \frac{1}{k_1 A} \tag{3.10}$$

To characterize the influence of diffusion, we can use Fick's law:

$$\frac{dn}{dt} = (C_\infty - C_i) D \frac{A}{L} = \frac{(C_\infty - C_i)}{R_D} \tag{3.11}$$

Where D is the developer's diffusion coefficient and L is the distance from the surface of the HSQ layer to the development reaction site (i.e. the length of the channel that has been developed out). R_D can then be defined as:

$$R_D \equiv \frac{L}{DA} \tag{3.12}$$

The relative influence of the two "resistances" will define the overall development rate. When L is small, R_D is insignificant and the development is reaction-rate-limited. As L increases, though, R_D increases correspondingly and will eventually overwhelm R_R. At this point, the development is diffusion-limited and the reaction rate has little or no effect on the overall development rate. Likewise, R_D will increase much more quickly if the cross-sectional area A is small, meaning that, when developing extremely narrow features, diffusion limitation is a much more serious issue than it is when developing large structures where the developer can easily access the reaction interface.

This diffusion limitation is important because, as previously discussed, HSQ has a "time limit" on its development. In the case of narrow features (such as the sub-10-nm pitches we are trying to yield), the limitation of the development reaction by diffusion may not allow the resist to fully clear before the HSQ reaction is stopped, even if the resist contrast is high and the features are well-defined by a narrow electron beam.

3.7.3 Experimental Verification

Empirical evidence exists to support the idea that diffusion limitation during development is the "x-factor" keeping us from achieving our maximum theoretical resolution. Figure 3-27 shows contrast curves for HSQ developed in 1% NaOH for several development times, again measured by exposing and developing large areas of HSQ and measuring the remaining resist with a profilometer.

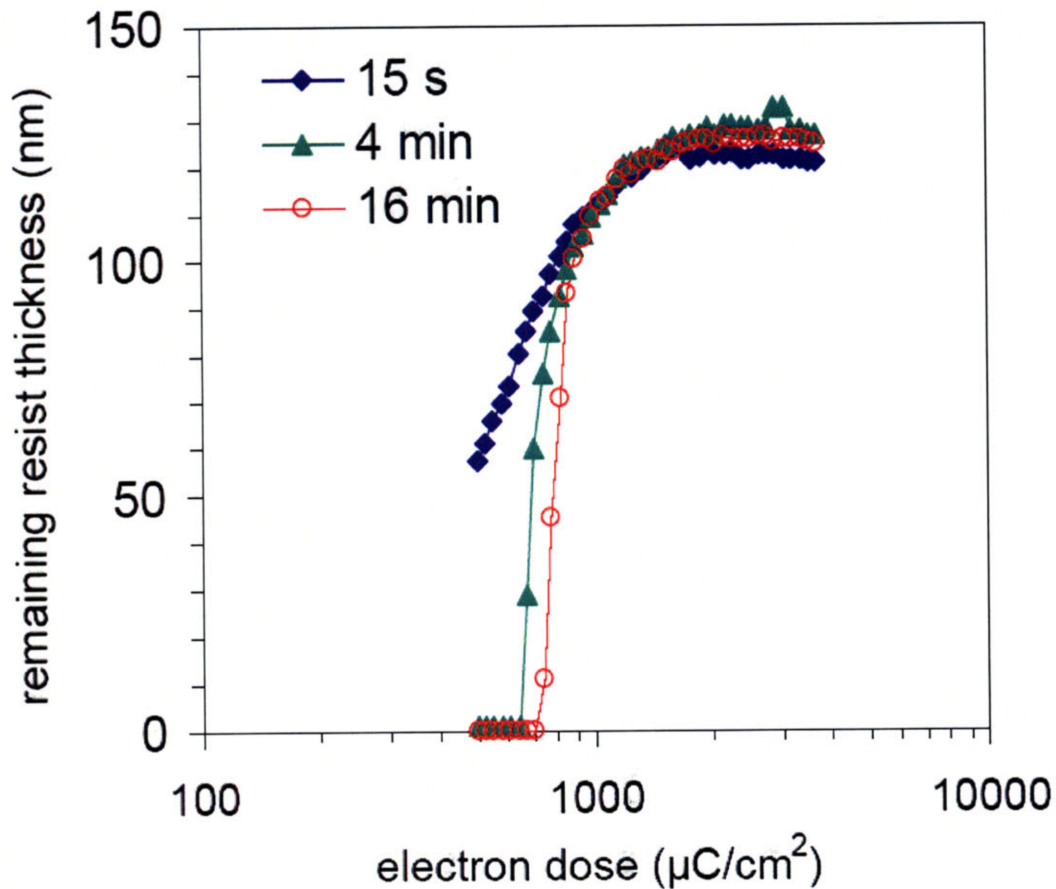

Figure 3-27: Contrast curves for HSQ developed in 1% NaOH/4% NaCl for various times. Note that the contrast in the 15-second development time case is much lower than the others, which would be expected to have a detrimental effect on final resolution. (Data courtesy J. Yang)

The contrast in the 15 second case is much lower than any of the longer development times, which should in principle translate to a lower resolution if short development times are used. As figure 3-28 shows, however, this is not the case.

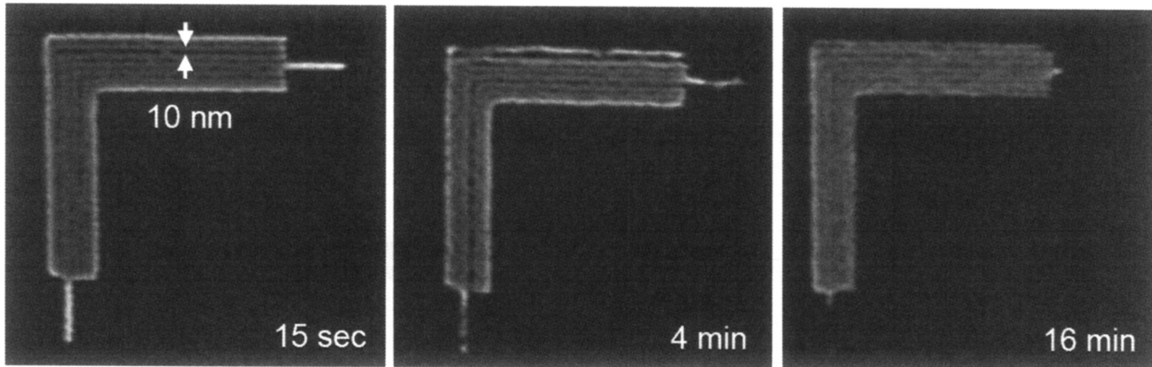

Figure 3-28: Scanning electron micrographs of 10-nm-pitch nested-L structures fabricated using 20-nm-thick HSQ and developed in 1% NaOH/4% NaCl for the times indicated on the images. While the contrast curves in figure 3-27 would seem to suggest that the resolution in the 15-second-develop case should be much lower than the others, the micrographs show that this is not the case. The 15-second sample actually looks better than the others, due to the slow, nonselective pitting of exposed HSQ that occurs during prolonged immersion in developer. This suggests that the resist contrast, as long as it is "good enough," is not an important limiting factor at these length scales. (Micrographs courtesy J. Yang)

The micrographs in figure 3-28 suggest that resist contrast, as long as it is above a certain minimum threshold (high enough to allow pitches that are 1.5-2× the FWHM of the beam to be printed), is not an important real-world limiting factor when working at these length scales, since other factors, most likely diffusion-limited HSQ development, keep us from reaching our theoretical maximum resolution in any case. This contradicts the theory-based conclusion in section 3.1 that contrast will affect resolution as long as the minimum achievable pitch is higher than the FWHM of the beam, a conclusion which does not take developer mechanics into account.

3.8 Conclusion and Further Work

It appears that, when HSQ patterns approach the 10-nm-pitch threshold, both resist contrast and point-spread function cease to be important limiting factors in real-world resolution. There is some additional factor (or factors) keeping us from reaching the 4-nm-pitch resolution that our calculations and beam-diameter measurements suggest is theoretically possible, meaning that no matter how much we improve resist contrast or tighten our beam profile, yielding pitches below 8-10 nm is not possible. On the upside, the lack of dependence on contrast means that the process, while limited in resolution, is much more robust than previously thought—lowered resist contrast or a slightly defocused beam should not have much effect on the final pattern.

The next logical step in this work is the characterization of these new factors that limit resolution when resist contrast and point-spread function cease to be an issue. This is difficult, as there are several processes contributing to the problem. As we saw in section 3.6, vibration noise in our SEM, while it does not affect lithography done in the same tool, tends to "blur out" 1-2 nm of resolution. A better electron microscope would mitigate this somewhat, but to entirely remove the effect of imaging noise transmission electron microscopy should be used for all metrology at these length scales.

According to our Monte Carlo model, secondary electrons generated by the primary beam do not significantly affect the final point-spread function. While this is an encouraging result, it contradicts both conventional wisdom and several published

articles.[31,32,43,71] It is possible that the single-scattering model is not accurate enough to be reliable at our length scales of interest, and that a full, first-principles Monte Carlo simulation with no simplifying assumptions (such as Bethe slowing) would yield different results.

The nanoscale development behavior of HSQ is something that is just beginning to be investigated in detail. The resist's highly nonlinear development rate and self-limiting development behavior are serious problems and remain poorly-understood. Characterizing this behavior, as well as quantifying the diffusion-limited development discussed earlier would allow the pinpointing of the exact pitch where diffusion starts to seriously limit resolution. Another approach is to simply vary the process in order to change the parameters in the model, which can be done without a full understanding of the development process. For example, ultrasound can be used during the development process to increase the diffusivity of the developer, or the developer can be heated to increase both the diffusivity and reaction rate.[82] These approaches should in principle circumvent the diffusion problem, but both have issues of their own—ultrasonic development can damage small, delicate features, and aqueous-base developers tend to attack silicon substrates when heated past 30˚C or so. These problems have kept us from characterizing the effect of either process on final resolution, but this is an engineering issue only; better process control should allow more thorough work to be done in this vein in the future.

Finally, it should be noted that all of our resolution studies have been done using HSQ. The reason for this is that HSQ has many properties useful for characterization work—its developed patterns are hard enough to measure with a profilometer, can be imaged in a SEM without pattern transfer, and stand up to most types of postprocessing, and its sensitivity is fairly low. Unfortunately, its drawbacks (nonlinear development, mainly) may outweigh its advantages when working at sub-10-nm pitches. Most other common electron beam resists are difficult to use for this type of pure characterization work (PMMA degrades during SEM imaging, calixerene requires extremely high doses and extremely long write times to yield patterns, etc.), but in light of HSQ's issues it may be worth re-investigating other e-beam resists for these types of experiments.

Chapter 4: High-Resolution Liftoff Patterning Using a Lithographically-Defined Bilayer

Having investigated the optimization and limits of the exposure and development steps of SEBL processing in chapters 2 and 3, respectively, this chapter describes the implementation of that knowledge in a more practical context—in this case, the development of a robust metal-liftoff process capable of sub-10-nm resolution.

4.1 Electron-beam Evaporation

The ability to pattern metal structures using scanning electron beam lithography has been critical to advances in many different fields of nanotechnology. From mainstream applications like photomasks and interconnects to more exotic processes such as metal-catalyzed nanowire growth, the length scale at which it is possible to arbitrarily pattern metal in many ways defines the state of the art in nanoelectronics. While a number of groups, including ours, have obtained impressive results in this regard using negative electron resists (such as HSQ) and etch-based processes, liftoff processing, illustrated schematically in figure 4-1, has remained the technique of choice for this type of patterning almost since the industry's inception. There are several reasons for this: it permits patterning of materials that are difficult to etch (such as gold, platinum, and exotic magnetic materials), requires fewer steps and equipment than etch-based processing, and can, if done correctly, be reasonably high-resolution.

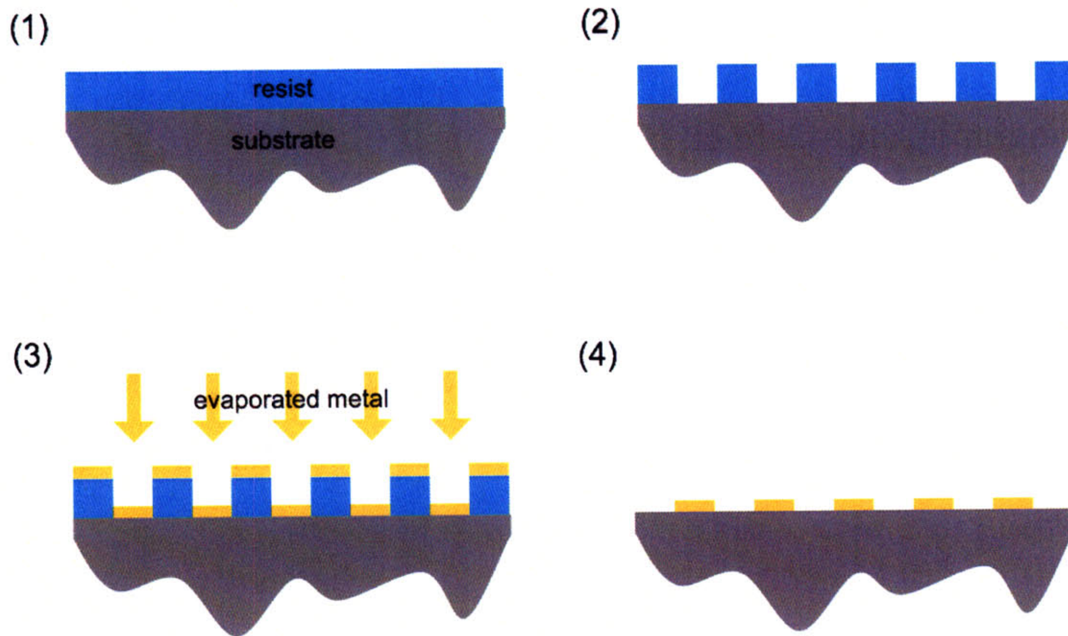

Figure 4-1: Generalized schematic of the liftoff process. Resist is deposited on a substrate (1), then exposed and developed (2). Metal is then evaporated onto the patterned resist (3). When the resist is dissolved (4), metal remains in the regions where resist has been developed away.

While liftoff-processing resolution in the 50-nm regime have been sufficient for most mainstream industrial uses over the last few decades, some of the more exotic applications we have encountered (gold-catalyzed nanowire growth, study of thin-film dewetting, nanogap contacts for quantum dots, liftoff of sputter-deposited films, among others) have forced us to develop a liftoff process with both high resolution and a high degree of adaptability. Fortunately, a process I developed in 2006 for the fabrication of small Josephson junctions[50] has proven much more versatile than originally planned, and is currently still used in processes where sub-50-nm resolutions and a high degree of repeatability are required.

4.2 Suspended Shadow-Mask Evaporation

Suspended shadow-mask evaporation was developed in the 1970s as a simple, high-resolution method of fabricating Josephson junctions[83], a superconducting device consisting of two layers of superconducting metal (aluminum, in this case) with a thin dielectric layer (aluminum oxide here) in between. Josephson junctions are used in superconducting quantum interference devices (SQUIDs), superconducting flux-quantum (SFQ) logic circuits, and superconducting qubits; the latter application's interest in studying nanoscale junctions was the original motivator for this research.[84,85]

4.2.1 Process Overview

The shadow-mask process, illustrated in figure 4-2, consists of two sequential angle-evaporation steps into a suspended "bridge" region of a resist bilayer, with a brief oxidation step in between to form the necessary insulating barrier. As the schematic suggests, fabricating the 3D bilayer resist structure required to make the "suspended-shadow-mask" is the most difficult part of the process.

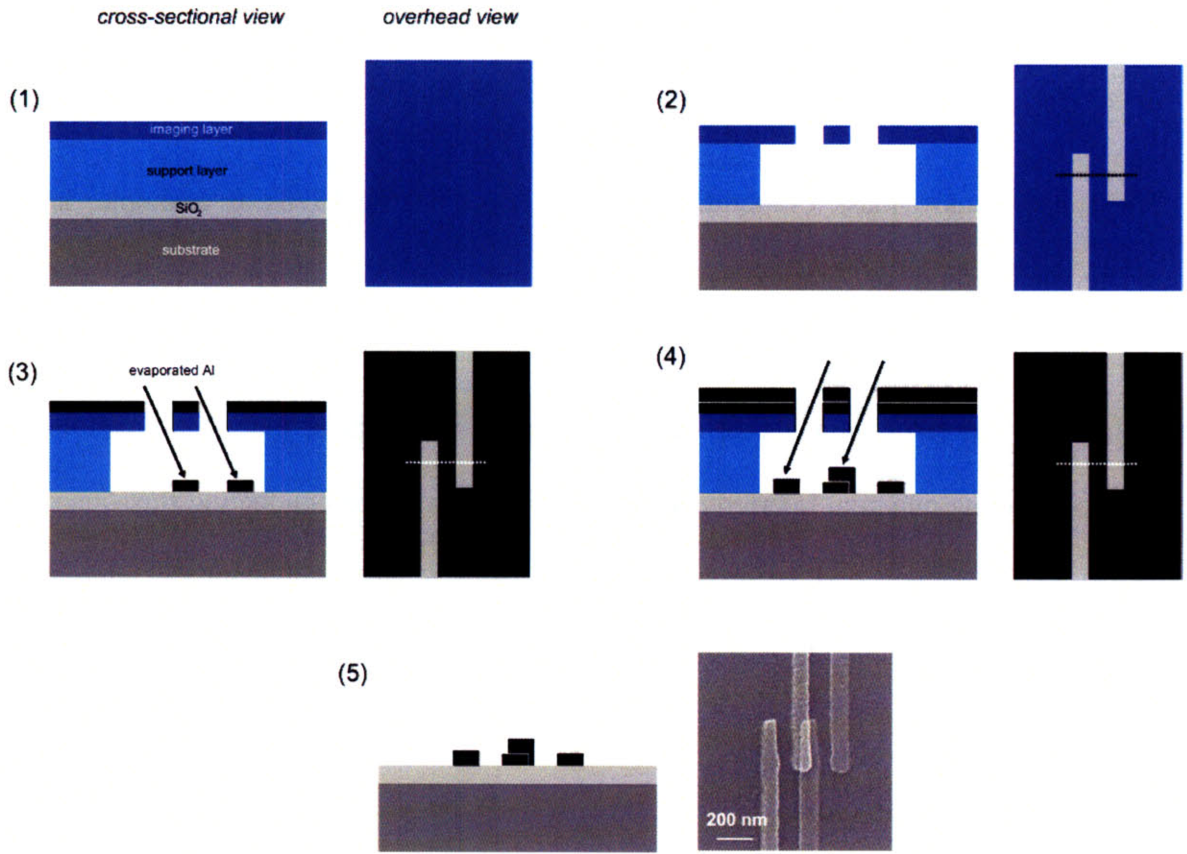

Figure 4-2: Schematic diagram of the suspended shadow-mask evaporation process flow, from both cross-sectional (left) and overhead views, with the dotted line in the overhead view representing the point of cross-section. A resist bilayer consisting of a thick support layer and thin imaging layer is deposited on an insulating substrate (1). The bilayer is then patterned with two overlapping lines, and then developed so that a suspended "bridge" is formed in the imaging layer where the lines overlap (2). Aluminum is then angle-evaporated into the region under the suspended bridge (3), allowed to oxidize, and then evaporated again from the opposite angle (4). When the resist is stripped (5), an Al/AlO$_x$/Al Josephson junction is formed where the lines overlap, as shown in the bottom-right micrograph.

4.2.2 Bilayer Fabrication

The nontrivial part of the shadow-mask evaporation process is the fabrication of the 3D suspended shadow mask structure in the resist bilayer. Fabricating this structure at high resolution involves care in the selection of bilayer materials, exposure and development of the imaging layer, and removal of the support layer to create the suspended region.

4.2.2.1 Overview

The traditional way to define the bilayer structure is to use a thin, high-resolution imaging layer (PMMA is excellent here, and nearly universally used) on top of a thick support layer. The choice of stack materials varies, and many variations have been tried by different groups over the years. Imaging layers made of PMMA,[86-88] other electron resists such as ZEP520,[89,90] optical photoresist,[83] polysilicon,[91] and metal[92,93] have been used, and support layers as varied as poly(methylglutarimide) (PMGI),[86,87] various copolymers of PMMA,[88,94] standard organic photoresists,[83] and spin-on glass[91] have all been tried at some point in time.

4.2.2.2 Copolymer Method

Of the previously-mentioned approaches, the poly(methylmethacrylate)/ poly(methylmethacrylic acid) (PMMA/PMAA) copolymer scheme is the most common method of bilayer fabrication, owing to its relative processing simplicity and reasonably

high resolution.[94] As the schematic in figure 4-3 illustrates, the undercut opening is first exposed in the PMMA imaging layer using SEBL. The entire bilayer is then subjected to a UV flood exposure, which increases the dissolution rate of the PMMA/PMAA copolymer support layer without significantly affecting the PMMA imaging layer. When the structure is developed in a standard PMMA developer (various mixtures of methyl-isobutyl-ketone (MIBK) and isopropanol (IPA) are most commonly used), the support layer develops much more quickly than the imaging layer, producing an undercut structure. Several groups have used variations on this process, with generally favorable results.[83,84,86-88,93,94]

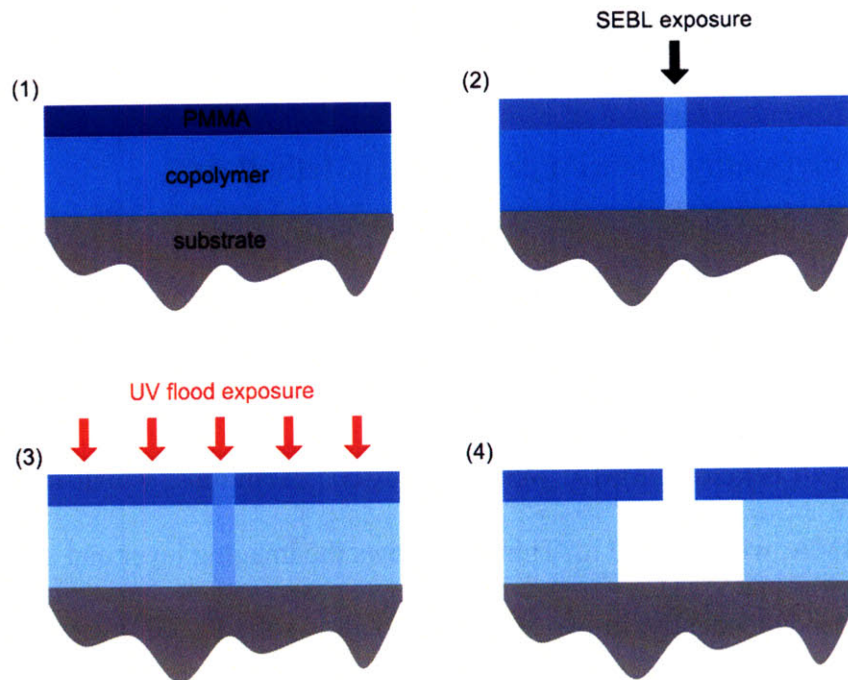

Figure 4-3: Schematic illustration of the PMMA/copolymer shadow-mask process. A bilayer consisting of a PMMA imaging layer and a PMMA/MAA copolymer support layer (1) is exposed using scanning electron-beam lithography (SEBL) (2), then flood-exposed with 220 nm UV light to increase the sensitivity of the copolymer imaging layer (3). When the bilayer is developed, the flood exposure causes the copolymer to develop much more quickly than the PMMA, resulting in an undercut structure (4).

An inherent issue with the PMMA/PMAA bilayer scheme is imaging layer bias—since the two layers are developed concurrently, the longer development times required to produce a suitable amount of undercut in the support layer can also significantly enlarge the features in the imaging layer. This effect is negligible for structures larger than 50-75 nm, but for structures smaller than this the copolymer-based method is unsuitable, as variations in feature geometry and development conditions will cause the biasing to be

both significant and relatively unpredictable, making repeatable structure fabrication impossible.

4.2.2.3 Poly(methylglutarimide) (PMGI) Method

Using poly(methylglutarimide) (PMGI), rather than PMMA/MAA copolymer, as the support layer mitigates this biasing problem. PMGI is not affected by the various organic solvents used to develop PMMA; only aqueous-base solutions, which in turn have no effect on PMMA, will dissolve it. This fact allows the imaging layer and support layer to be developed independently, in two steps; it also allows the PMGI layer to be developed for any necessary length of time without significantly affecting the imaging layer.[11] PMGI also has the advantage of being a "lift-off resist," meaning it dissolves in developer without exposure to radiation or electrons. There are, in principle, other similarly complementary choices of bilayer materials that could be used here, but none have demonstrated the imaging-layer resolution and ease of processing of the PMMA/PMGI approach.[89,90]

In principle, a PMMA/PMGI bilayer should allow any degree of undercut to be produced simply by exposing and developing the PMMA, then leaving the sample in the PMGI developer for as long as is necessary to produce the desired degree of undercut. In practice, however, small variations in factors such as temperature, developer concentration, and feature size can cause significant run-to-run variations in the undercut; we observed undercut variations of 50 nm or more in some cases, using ostensibly

identical processing conditions, when using this process. Since an undercut that is too small will complicate the liftoff process and an undercut that is too large will collapse the imaging layer, the PMMA/PMGI process suffers from a lack of robustness, despite its improved resolution.

4.2.3 Lithographic Undercut Control

The solution to the repeatability problem in the PMMA/PMGI process is to define the undercut regions lithographically, rather than during development. Although PMGI is sold as a "lift-off resist" and was not designed to be exposed to an electron beam, our experiments have shown that it is actually an extremely sensitive electron resist. Figure 4-4 shows contrast curves for PMGI using various dilutions of CD-26 (a standard developer consisting of a 0.26N solution of tetra-methyl-ammonium-hydroxide [TMAH]), as well as a similar curve for PMMA for comparison purposes. Two characteristics of the curves are readily apparent. While PMGI still dissolves without exposure in these dilute developers, electron exposure can significantly increase the development rate—in the case of the 60% CD-26 curve, by nearly a factor of ten. The electron sensitivity of PMGI is also much lower than PMMA, meaning a dose of electrons too low to affect PMMA can significantly increase the development rate of PMGI. The result of this difference in sensitivity is that there is a dose regime, indicated on the figure, where the PMGI layer of a resist bilayer can be exposed without affecting the PMMA above it.

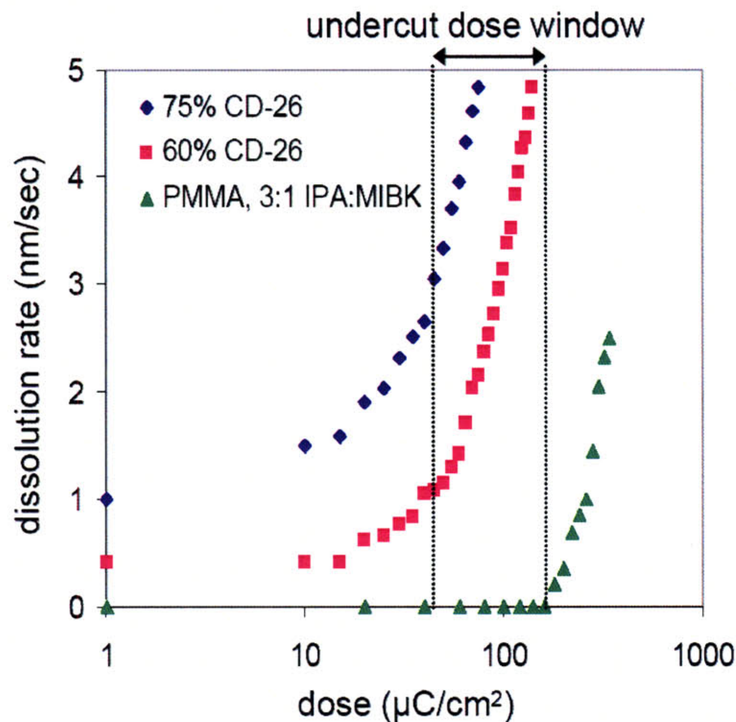

Figure 4-4: Contrast curves (dissolution rate as a function of electron dose) for PMGI in two dilutions of CD-26 developer, as well as PMMA in its standard 3:1 IPA:MIBK developer for reference. When a 60% solution of CD-26 is used, electron exposure of PMGI can increase its dissolution rate to up to 10× the rate of unexposed PMGI. The "undercut dose window" noted on the figure qualitatively indicates the dose regime where the dissolution rate of PMGI is increased but that of PMMA is unaffected.

The useful properties of PMGI when exposed to an electron beam allow us to define undercut structures in a bilayer using lithography, rather than relying on imprecise and easily-contaminated development processes. In order to do this, a second electron exposure, at a dose contained in the "undercut window" of figure 4-4, is used to define the undercut regions adjacent to the feature in the imaging layer; this process is described in figure 4-5. This low dose passes through the imaging layer without affecting it, but

causes the underlying PMGI to develop much more rapidly. As a result, the support-layer-development step of the process is both faster and more robust: since the exposed PMGI develops so much more quickly than the unexposed PMGI, slight variations in development time, developer temperature, concentration, and other factors will not significantly alter the dimensions of the undercut.

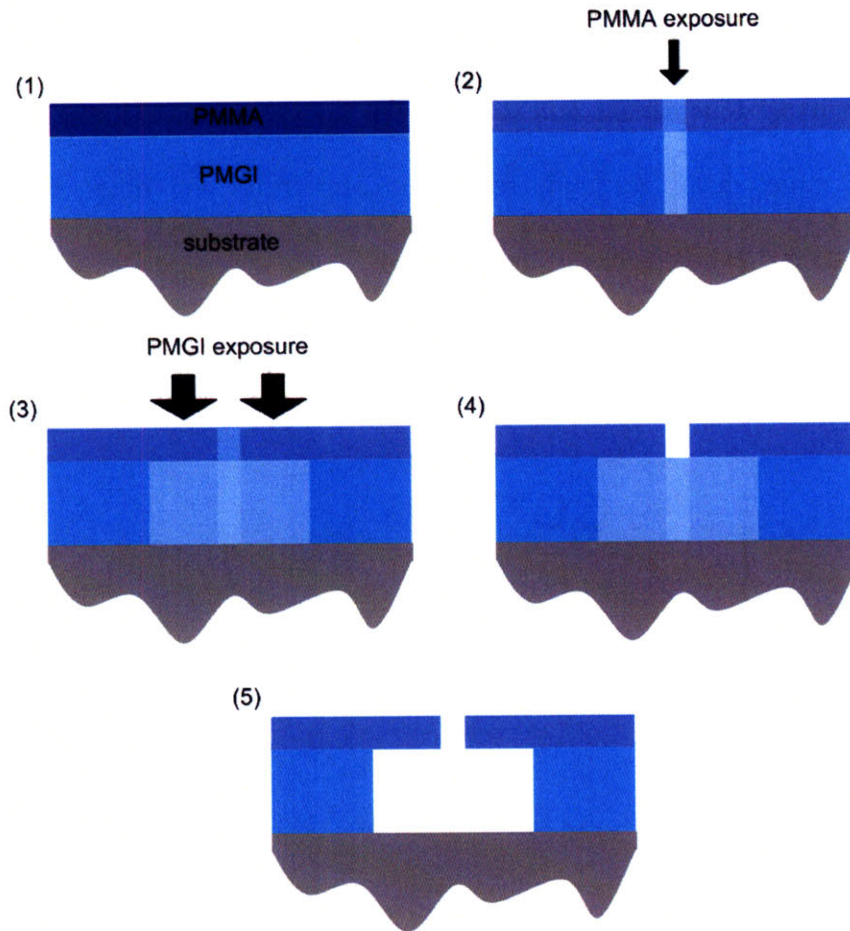

Figure 4-5: Schematic illustration of the PMMA/PMGI process with lithographic undercut definition. The PMMA/PMGI bilayer (1) is exposed to a high electron dose to define the imaging-layer features (2), followed by a low electron dose to define the undercut regions in the PMGI (3). The PMMA layer is then developed (4), followed by the PMGI, which quickly develops away in the exposed regions and produces a final undercut that is very close to the defined undercut regardless of minor process variations.

4.3 Exposure Modeling

In order to formulate a complete model of the lithographic-undercut process and determine whether it 1) was realizable, and 2) would produce results in line with what was expected (i.e. controllable, robust undercuts), the electron-scattering properties of the PMMA/PMGI bilayer, as well as its contrast behavior, were examined.

4.3.1 Description

A Monte Carlo model was used to simulate the bombardment of a typical bilayer with 30 keV electrons using CASINO, a program for modeling electron scattering behavior in materials.[70] The simulation results, a 3D plot of deposited energy density vs. position in the bilayer, were integrated along one lateral dimension to obtain a two-dimensional data set, then plotted as 1D representations of the electron point-spread function at various depths. The point-spread function plots were then fitted to equation (4.1) the standard double-Gaussian model used to model electron scattering in materials:[38,56]

$$E(r) = \frac{D_n}{\pi}\left(\frac{1}{\alpha^2}e^{-\left(\frac{r^2}{\alpha^2}\right)} + \frac{\eta}{\beta^2}e^{-\left(\frac{r^2}{\beta^2}\right)}\right) \quad (4.1)$$

Where E is the actual dose at a given point, D_n is the nominal electron dose, α is the forward-scattering parameter, β is the backscattering parameter, η is the ratio of backscattered electrons to incident electrons, and r is the radial distance from the center

of the function. The double-Gaussian model allows the entire Monte Carlo data set to be reduced to table 4-1, expressing the three scattering parameters as a function of resist depth. In order to verify the Monte Carlo results, the point-spread function was measured experimentally (figure 4-6),[35] and the backscattering coefficient β shown to be within 10% of the surface β in the model.

depth (nm)	**material**	α **(nm)**	β **(nm)**	η
50	PMMA	5.20	4090	*3.2*
100	PMMA	4.87	3650	0.42
150	PMGI	6.40	3770	0.68
200	PMGI	7.23	3710	0.74
250	PMGI	8.46	3420	0.82
300	PMGI	9.84	3280	0.94
350	PMGI	12.75	2970	0.95

Table 4-1: Double-Gaussian scattering parameters as a function of depth for a resist bilayer consisting of 100 nm PMMA on 250 nm PMGI, based on data from Monte Carlo simulations. The top-layer η *value is a spurious result (suggesting that there are 3.2*$\times$ *more backscattered than incident electrons near the top of the resist stack) thought to be caused by a mesh-boundary problem in the software.*

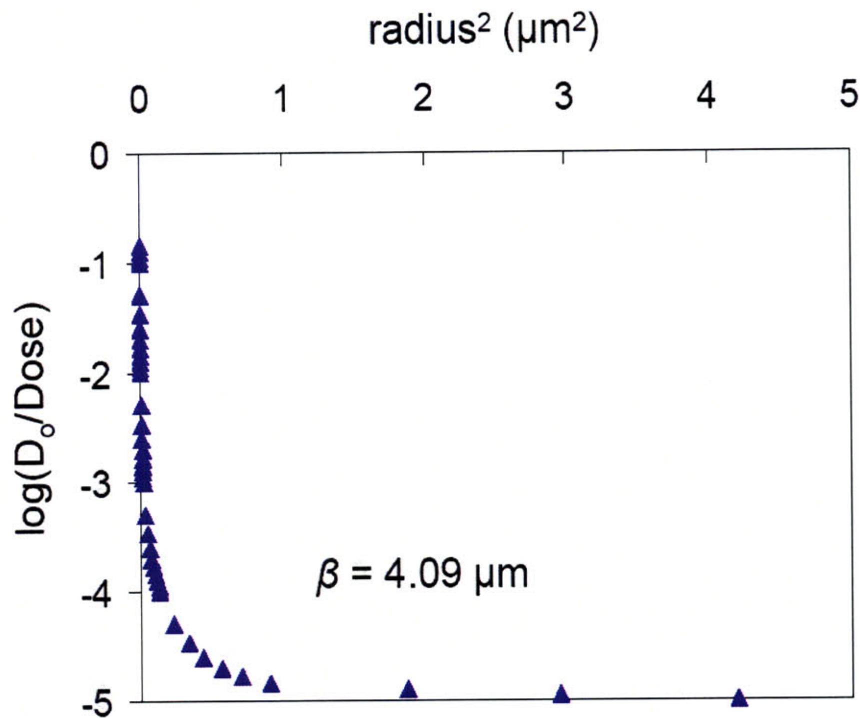

Figure 4-6: Experimentally measured point-spread function for 30 KeV electron exposure of PMGI, taken using single-point exposures at many doses and measuring the radii of the developed features.[35] *The backscattering coefficient extracted from this data closely matches the Monte Carlo results in table 4-1.*

4.3.2 Results

Using the scattering data obtained from the Monte Carlo simulation and the experimental resist-contrast data in figure 4-4, it is possible to simulate the exposure of a PMMA/PMGI bilayer and create a predictive model of the two-dose process shown in figure 4-5. In order to do this, a feature with a given PMMA linewidth and PMGI undercut dimension was convolved with the point-spread functions at several resist depths. The resulting dose profile was then combined with the contrast curve data for

each resist type, giving 2D cross-sections of the resist profile showing contours of constant development rate. As expected (and shown in figure 4-7), the additional dosing of the PMGI adjacent to the feature increased its dissolution rate by nearly a factor of five, indicating that lithographic control of the undercut was a viable alternative to development-based undercut processes.

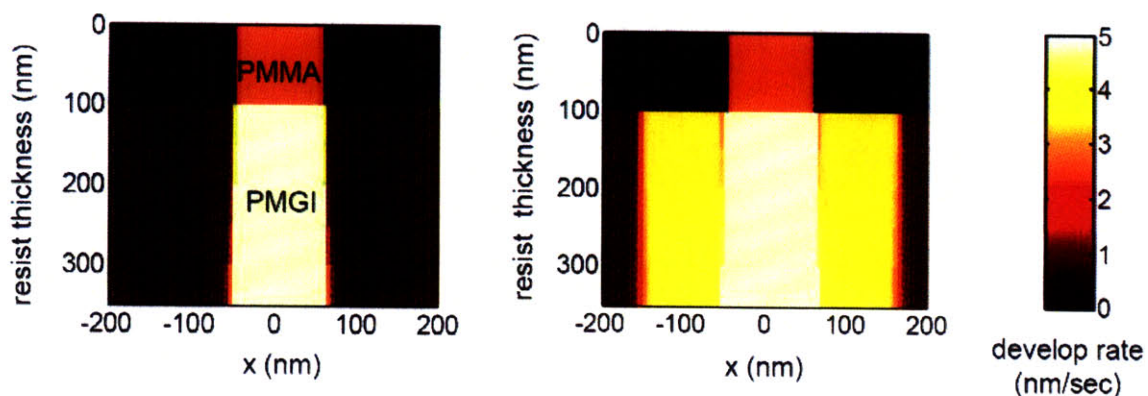

Figure 4-7: Contours of constant development rate (extracted from the scattering and contrast data shown in table 4-1 and figure 4-4) for a bilayer consisting of 100 nm of PMMA on top of 250 nm of PMGI. Each plot has a 100-nm-wide feature defined in the imaging layer. Plot (A) has no lithographically-defined undercut, while plot (B) has 100 nm of undercut defined on each side of the feature. As the figures show, the development rate of the PMGI increases significantly in the undercut region when an undercut dose is applied, proving the validity of the lithographic-undercut process.

4.4 Experimental Results

Modeling of the PMMA/PMGI-bilayer exposure process indicated that it should be possible to accurately define a wide range of undercuts using lithography, and our subsequent experiments have borne this out.

4.4.1 Procedure

The samples we used to collect data were silicon wafers coated with a 100-nm layer of insulating SiO_2. The 250 nm PMGI support layer was applied by spin-coating and baked on a hot plate at 265°C for 5 min, followed by the 50-100 nm 950K-PMMA imaging layer, which was baked at 180°C for 10 min. The samples were exposed in a Raith 150 SEBL system with an electron energy of 30 keV, a working distance of ~6 mm, and a beam current of ~250 pA; the lines were exposed at a dose of 400 $\mu C/cm^2$ and the adjacent undercut regions were exposed at a dose of 100 $\mu C/cm^2$. The PMMA was developed via immersion in a 3:1 IPA:MIBK solution at 20˚C for 180 s, and the PMGI was developed in a 60% solution of CD-26 developer for 1 to 4 min.

4.4.2 Results

The resulting structures were cross-sectioned and measured using a scanning electron microscope (SEM) to determine the extent of the undercuts. As figure 4-8 shows, if a

sufficiently long PMGI development time was used, the experimental results closely matched the undercuts defined by the lithography.

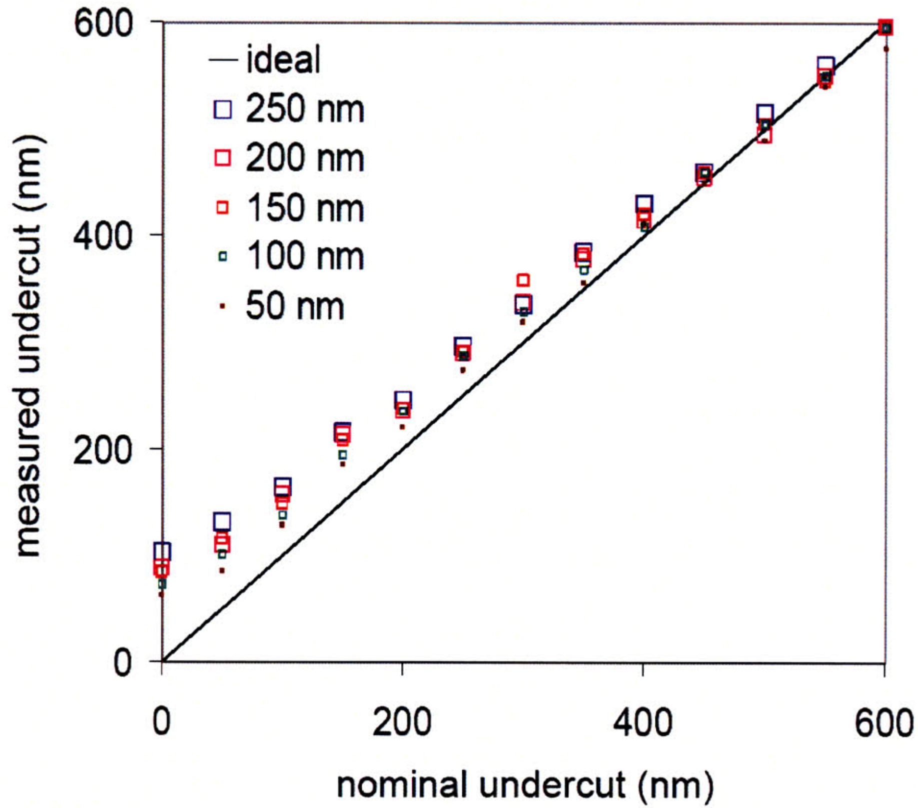

Figure 4-8: Measured vs. nominal (defined) undercut values for five different imaging-layer linewidths after a 4-minute development of the PMGI support layer. For small undercuts, slow dissolution of the unexposed PMGI results in undercuts that are slightly larger than defined, but for larger undercuts the results for all linewidths are very close to ideal.

4.4.3 Undercut Saturation

When the development time was reduced, a noticeable "saturation effect" was observed in the data, with undercuts that never exceeded a certain width regardless of their nominal value. This effect, illustrated in figure 4-9, was more pronounced at shorter development times, and the maximum achievable undercut was proportional to the linewidth of the PMMA features. Nothing in the exposure model accounts for this behavior, suggesting that the development process may be introducing another limiting factor.

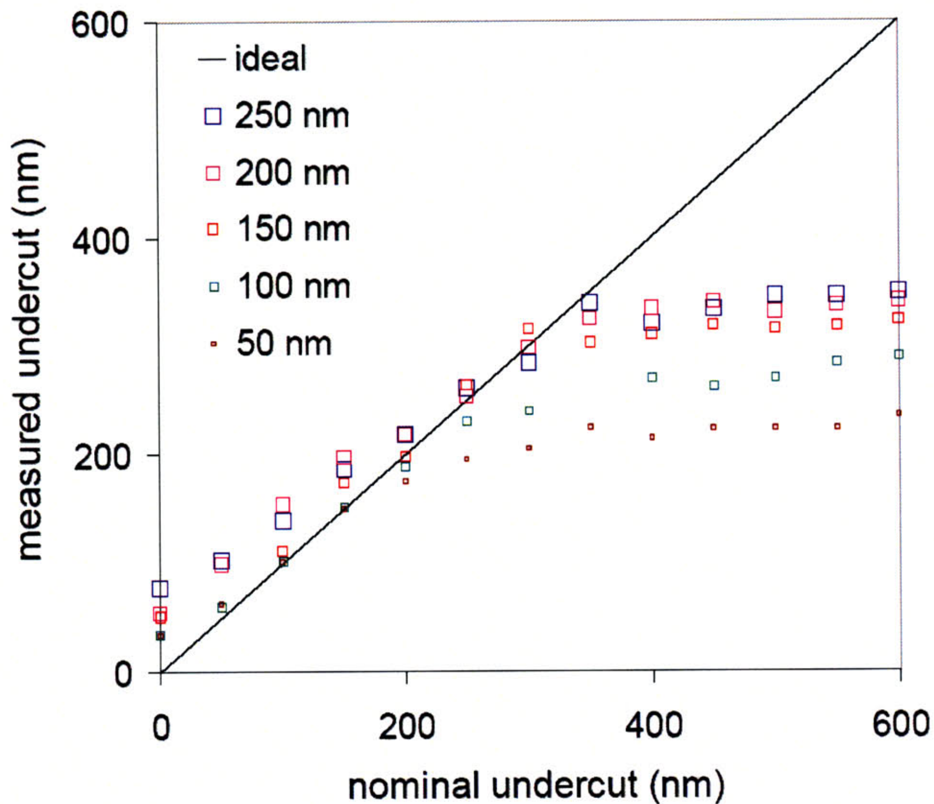

Figure 4-9: Measured vs. nominal undercut for conditions identical to those in figure 4-8, but with the PMGI development time reduced to 2 minutes. For undercuts below about 200 nm there is no significant change in the data, but for larger undercuts the measured values "saturate" to a maximum undercut width proportional to the linewidth of the imaging-layer feature.

4.5 Development Modeling

The saturation behavior in figure 4-9 can be explained with some additional modeling of the development process.[81] The reduction in development rate for deeper undercuts and

the fact that highest achievable undercut was proportional to the imaging-layer linewidth suggested that narrow openings in the PMMA may restrict the developer's access to the PMGI support layer. In order to quantify this behavior, a model combining mass-transfer and reaction kinetics was used to examine the development process. This model is actually a more detailed version of the qualitative development model described in section 3.7.

4.5.1 Model Description

Both the reaction rate and diffusion rate of the developer were taken into account in the model, in order to determine the relative effect of each process on the development rate. Figure 4-10 illustrates the temperature dependence of the development reaction, and shows that it is a standard first-order reaction with an Arrhenius-like (exponential) temperature dependence. In addition, it was assumed for simplicity that the diffusion of developer through the PMMA/PMGI bilayer could be described by ordinary diffusion in a stationary medium. Operating under these assumptions allows the problem to be expressed as the equivalent electrical circuit shown in figure 4-11, with the developer concentration corresponding to the voltage, developer flux corresponding to the current, and the different inhibitors of the development reaction (diffusion through the bilayer and rate of reaction) corresponding to resistors. The diffusion "resistances" can be expressed as $R_D = \frac{L}{DA}$, where L is the length of the channel, A is the cross-sectional area, and D is the diffusivity of the developer. The resistance due to the reaction rate can be written as

$R_R = \frac{1}{k_1 A}$, where k_1 is the first-order reaction rate and A is the cross-sectional area of the reaction interface.

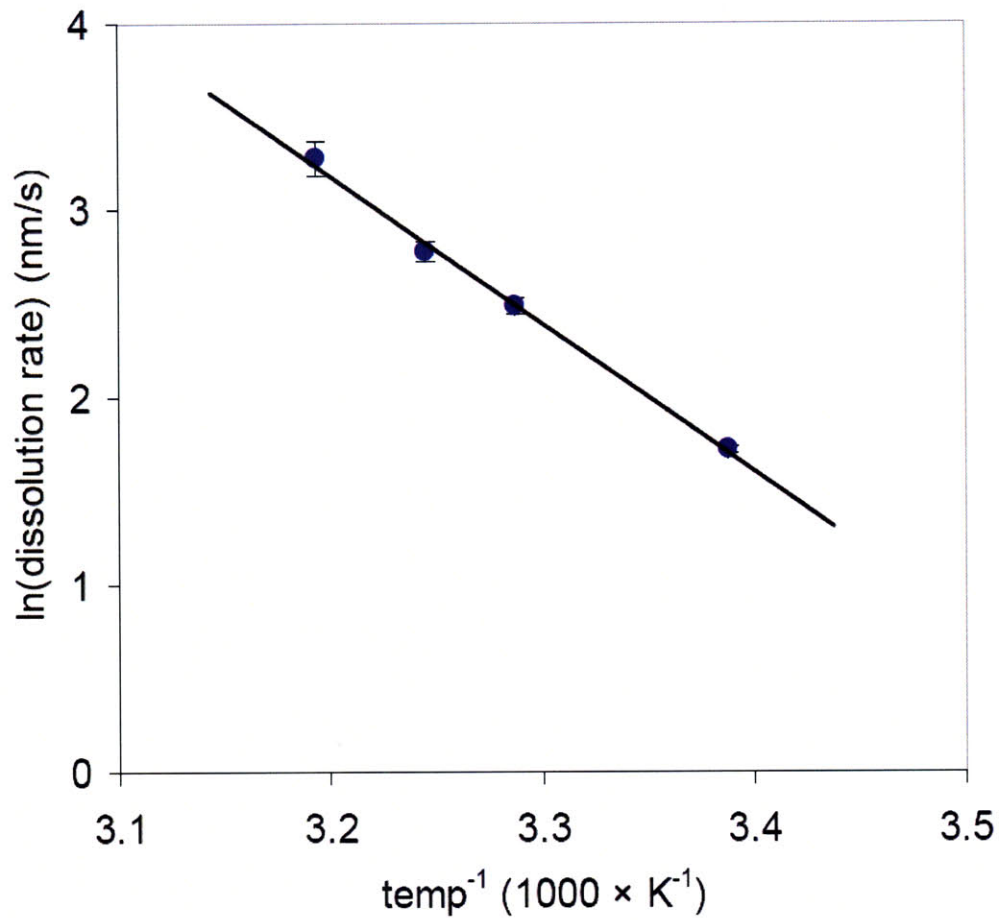

Figure 4-10: Arrhenius plot of the temperature dependence of the PMGI development reaction. The data corresponds to a first-order reaction with a rate defined by the equation $R = R_0 e^{-\frac{T_0}{T}}$. *$R_0$ in this case is 2.01 × 10^{12} nm/s and T_0 is 7860 K.*

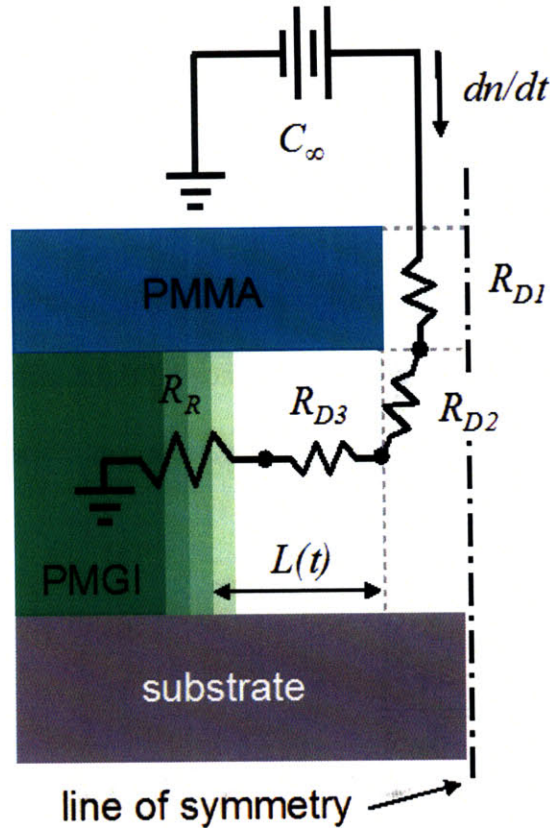

Figure 4-11: Cross-section of a PMMA/PMGI overhang structure with the equivalent circuit used to model the development process shown. The "voltage" is the developer concentration, the "current" is the developer flux, and the "resistors" are the various inhibitors (both diffusion- and rate-related) to the development reaction.

4.5.2 Derivation of Undercut Relationship

Using the equivalent circuit model of figure 4-11 and Ohm's law, we can write down the following:

$$C_\infty = \frac{dn}{dt}(\sum R_D + R_R) \tag{4.2}$$

Where C_∞ is the bulk developer concentration, $\frac{dn}{dt}$ is the flux of developer into the undercut structure, R_R is the resistance due to the development reaction rate, and $\sum R_D$ is the sum of the resistances due to diffusion into the imaging layer, around the "corner", and beneath the undercut to the reaction site. Since both the diffusion- and rate-limited resistances are of interest here, two equations are relevant. The first is derived from Fick's law of diffusion:

$$\frac{dn}{dt} = (C_\infty - C_i)D\frac{A}{L} = \frac{(C_\infty - C_i)}{\sum R_D} \tag{4.3}$$

Where C_i is the reactant concentration at the reaction site. The rate of the development reaction can be described by first-order reaction kinetics:

$$\frac{dn}{dt} = k_1 C_i A = \frac{C_i}{R_R} \tag{4.4}$$

Where k_1 is the reaction rate. We can relate the rate of undercut $\frac{dL}{dt}$ to the developer flux (current) $\frac{dn}{dt}$ using a constant:

$$\frac{dL}{dt} = \frac{\gamma}{A}\frac{dn}{dt} \tag{4.5}$$

Where γ is a constant relating the two rates and A is the cross-sectional area of the channel. Combining equations (4.4) and (4.5) gives the following:

$$\frac{dL}{dt} = C_i k_1 \gamma \equiv v_i \tag{4.6}$$

Where dL/dt is being defined as the "undercut velocity" v_i for simplicity. As the developer concentration at the interface is unknown, it is impossible to solve for the undercut velocity here, but equation (4.6) can be modified to describe the undercut velocity in a purely rate-limited case, i.e. a case where the reaction-site concentration is identical to the bulk concentration and developer diffusion is irrelevant:

$$v_\infty = C_\infty k_1 \gamma \tag{4.7}$$

Where v_∞ is the rate-limited undercut velocity. The contrast measurements in figure 4-4 give a good estimate for v_∞, since the dissolution of the PMGI in those experiments was purely rate-limited. We can now solve equation (4.2), first by substituting equation (4.5) into it, which gives:

$$\frac{dL}{dt} = \frac{\gamma}{A(\sum R_D + R_R)} \tag{4.8}$$

Substituting the value for R_R and equation (4.7) into this expression gives the final expression for the undercut rate:

$$\frac{dL}{dt} = \frac{v_\infty}{1 + \frac{v_\infty A \sum R_D}{\gamma C_\infty}} \tag{4.9}$$

The values of γ and C_∞ are not precisely known, but since they appear as a product in the equation they can be used as a single fit parameter here. The form of equation (4.9) is interesting, suggesting that for small values of R_D the undercut rate is approximately equal to the reaction rate, but as the diffusion resistance increases, the equation is increasingly dominated by the second term in the denominator and the rate decreases. This behavior qualitatively matches the form of the plot in figure 4-9, which shows a constant-rate reaction eventually slowing and stopping.

4.5.3 Model Results

Using a single value for the fit parameter γC_{∞}, we were able to accurately fit this development model to data taken for four different PMGI development times, as shown in figure 4-12:

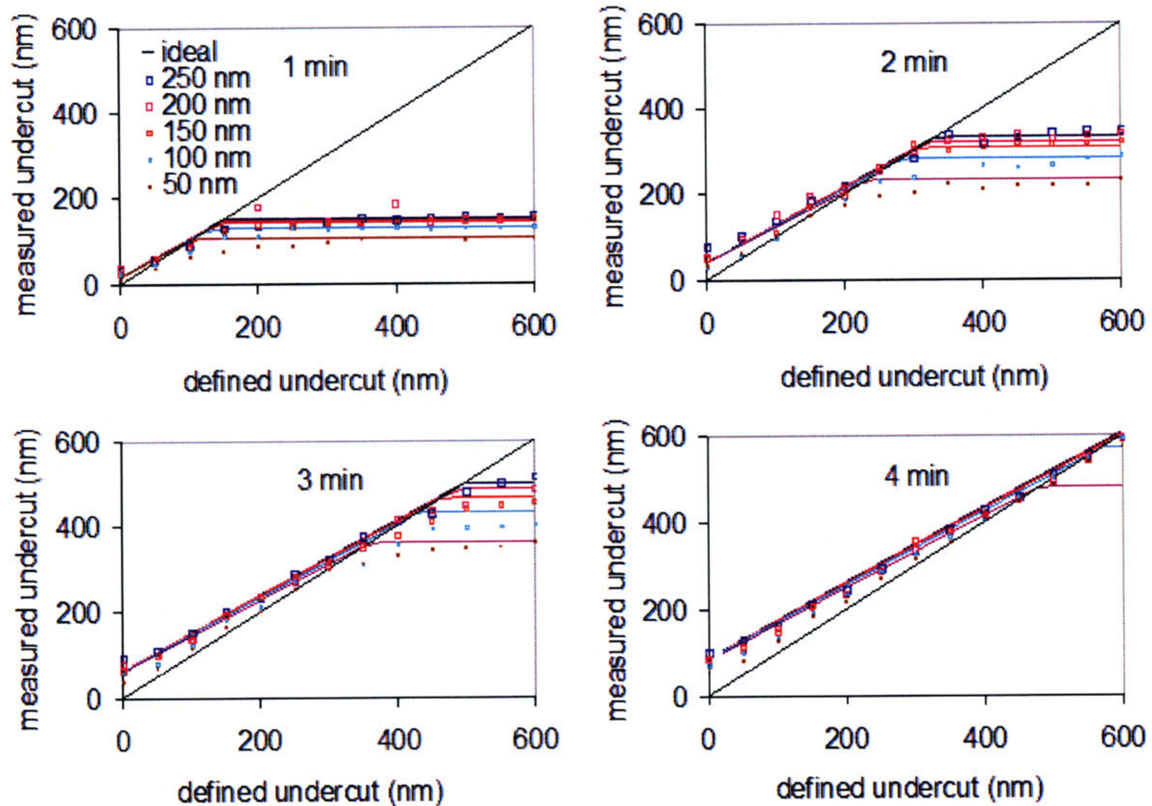

Figure 4-12: Measured vs. defined undercut for five different imaging-layer linewidths and four different PMGI layer development times. The solid lines are the development-model fits to the data (using the same fit parameter value in all four cases). The model accurately predicts both the biasing that occurs at small undercuts and long development times and the saturation effect observed in figure 4-9. At short (1 minute) development times, the onset of the saturation is nearly immediate, while PMGI allowed to develop for 4 minutes shows almost no saturation up to 600 nm of undercut, at the expense of some significant bias at lower undercut values.

Using this single fit parameter, the mass-transfer model can be used to simulate undercut behavior that closely matches the experimental data at all development times. The model

is plotted alongside the experimental data as solid lines in figure 4-12. As in the data, the undercut shows nearly linear behavior at long development times, but when the development time is reduced a clear saturation effect is observed as the developer is forced to travel through an increasingly long undercut channel to reach the reaction site. This channel increases the diffusion resistance ($\sum R_D$) in eq. (4.9) and causes the development process to transition from reaction-rate-limited to diffusion-rate-limited. In the diffusion-limited regime the developer is unable to reach the reaction site efficiently, resulting in a reduced undercut rate and a maximum undercut value that is independent of the defined undercut. As expected, this saturation occurs at smaller undercut values for narrow imaging-layer linewidths, since the developer encounters a higher diffusion resistance when traveling through narrow openings in the imaging layer. The model also predicts the nonzero *y*-intercepts (undercut bias) observed in figure 4-8; when the nominal undercut is very small, the developer quickly reaches the edge of the exposed PMGI and attacks the unexposed material beyond the defined undercut region, resulting in a larger-than-expected undercut.

4.6 Conclusion and Applications

While the process was originally designed for fabricating sub-100-nm Josephson junctions, it has also proven useful in various other liftoff-based applications due to its high resolution and robustness. Similar controlled-undercut bilayer processes have been developed in the past,[89,90] but none have demonstrated the combination of high resolution

and precise undercut definition of the PMMA/PMGI process, which has facilitated several interesting and useful applications.

The process has proven capable of its original application (sub-100-nm junctions), as figure 4-13 shows. Experimentation with undercut definition, however, has shown that the process is also capable of undercuts much wider than those needed for shadow-mask evaporation; as figure 4-14 illustrates, the sole limiting factor of undercut width (assuming diffusion is accounted for) appears to be the strength of the imaging layer. While the actual application for undercuts this large is not obvious (possibly nanoscale channels under the imaging layer for MEMS/NEMS applications), they demonstrate the range and robustness of the process nicely.

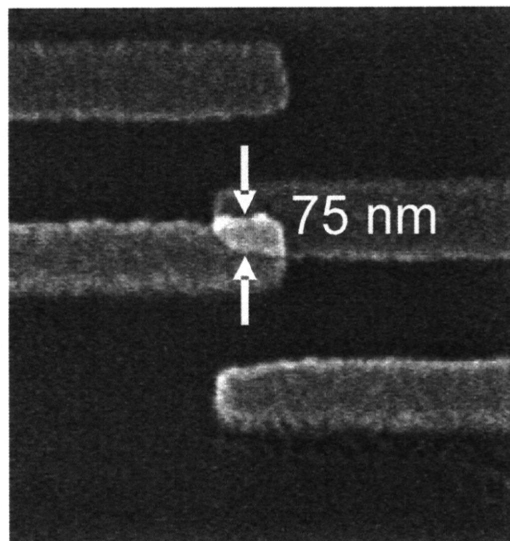

Figure 4-13: Scanning electron micrograph of an Al/AlO$_x$/Al Josephson junction fabricated using the PMMA/PMGI bilayer process. The width of the junction is 75 nm and the area is ~0.01μm^2.

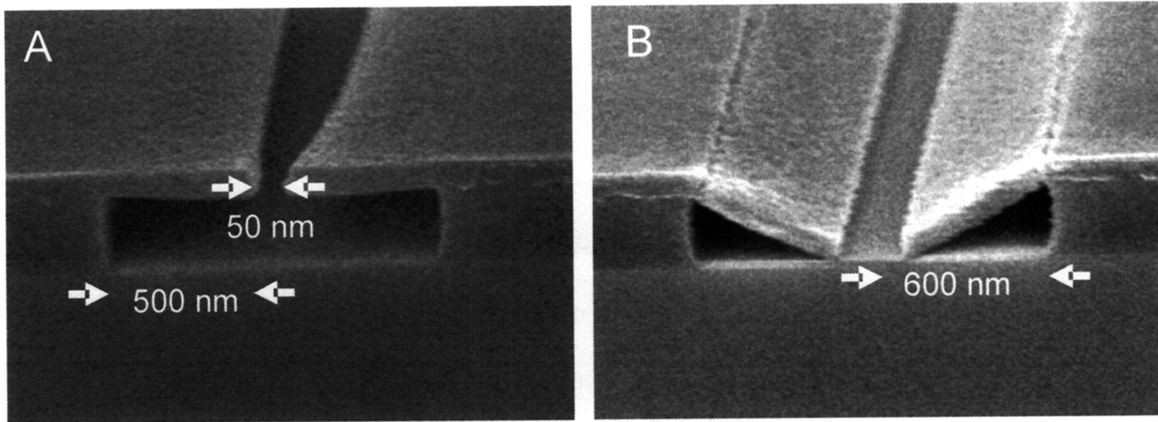

Figure 4-14: A*) Scanning electron micrograph of a 50-nm-wide line with 500 nm of undercut on each side defined in a PMMA/PMGI bilayer. The broadening of the line near the top of the image is an imaging artifact due to charging by the electron beam.* B*) 50-nm-wide line with 600 nm of undercut defined in an identical resist bilayer, illustrating the limits of undercut definition. The PMMA has collapsed here, though thicker PMMA layers allow even larger undercuts to be successfully defined.*

Resist thickness is one of the key resolution limiters in any liftoff process. Conventional wisdom states that, for a clean metal liftoff, the resist must be ~3× thicker than the metal being deposited. This can be a problem in SEBL-based processes, as thicker resist usually translates to increased beam scattering and consequently degraded resolution.[6,20-23,31,56] The bilayer process circumvents this issue; as long as the support layer is thick enough to satisfy the 3:1 resist/metal ratio, the imaging layer (which defines the final resolution) can be as thin as is mechanically feasible (extremely thin imaging layers will bend due to stress from the deposited metal film). Moreover, the ability to dial in an arbitrary undercut in the support layer ensures that, even in an imperfect evaporation system (with a large source width and/or short throw distance) it is possible to engineer

the discontinuous metal-film deposition that guarantees a stable and repeatable liftoff process.

As a result, the bilayer process has proven to be very versatile, and we have successfully used it to fabricate various high-resolution metal structures. As figure 4-15 shows, the process can be used to fabricate nano-spaced contacts, templates for the self-assembly of quantum dots, and any arbitrary metal structure with feature diameters down to nearly 10 nm.

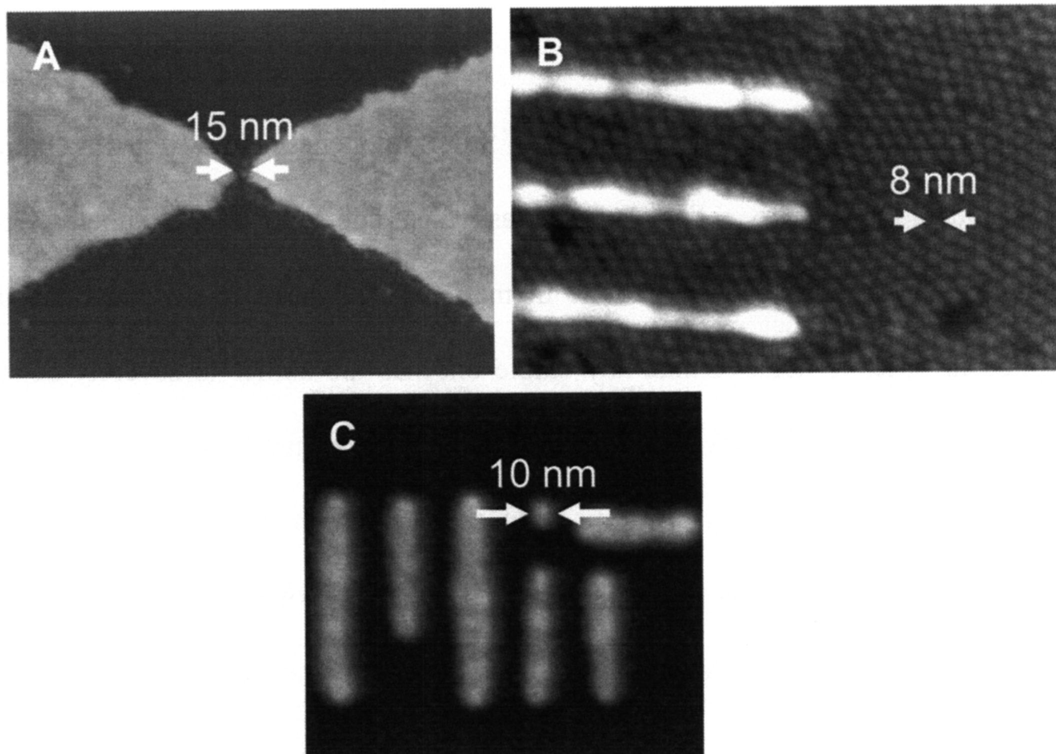

Figure 4-15: Various applications of the PMMA/PMGI bilayer process. A*) Ti-Au electrodes with a spacing of 15 nm, used to contact single quantum dots for electrical measurements.* B*) Ti-Au grating with ~15 nm linewidth, used as a template for the self-assembly of 8-nm-wide CdSe quantum dots.* C*) Ti-Au MIT logo, demonstrating liftoff resolution on the order of 10 nm.*

Chapter 5: Conclusion and Further Work

As we have shown, extending the resolution of SEBL to pitches below 10 nm in diameter is a formidable challenge. Factors such as resist contrast, beam diameter, resist development mechanics, and limitations in metrology all have to be simultaneously controlled in order to achieve this; any single one has the ability to severely degrade process resolution. While have succeeded in fabricating features as small as 8 nm in PMMA, and pitches as small as 9 nm in HSQ, the calculations of minimum achievable resolution in section 3.1 suggest that there is still quite a bit of room for improvement, and that issues with resist processing and metrology are the key limiting factors at present.

5.1 Resist Processing Limitations

At present time, the issue of resist contrast appears to be sufficiently under control for the two most common electron resists (PMMA and HSQ), as various resist-processing techniques have increased their contrast to the point where it is for all practical purposes infinite. Removing the influence of electron-beam scattering is relatively trivial; sufficiently thin resist and/or sufficiently high beam energies will ensure that the beam never experiences significant broadening when traveling through the resist film. The theoretical resolution (pitch on the order of the beam diameter) that should be achievable under these conditions is nowhere close to being realized, however, as issues with the

development mechanics of each resist remain serious limiting factors to final process resolution.

5.1.1 PMMA

While cold development has boosted the contrast of PMMA by nearly a factor of two over standard processing techniques, the minimum pitch achieved in our experiments was a disappointing 60 nm, which did not see the resolution improvement that individual lines did as the developer temperature is reduced. The most likely cause of this is mechanical instability—PMMA is a soft material, and thin, free-standing sections of it (such as the area between two closely-spaced lines) have a tendency to collapse during development. The standard method of mitigating this type of problem (using critical-point drying to eliminate the effects of surface tension on the developed pattern) cannot be used here, as the organic solvents used in CPD also develop PMMA; a full, 15-minute-plus CPD process will have the side effect of severely overdeveloping the resist. One possible solution to the collapse problem that has not been investigated yet is high-molecular-weight PMMA. While nearly all PMMA used in nanofabrication has a molecular weight of 950K, it has been shown that the starting molecular weight of the resist has (within reason) very little effect on sensitivity or contrast.[29] With this in mind, it may be possible to use PMMA with a molecular weight higher than 950K (2200K is commercially available) to fabricate patterns which, due to being composed of longer, more entangled macromolecules, have higher mechanical stability and, as a result, smaller minimum pitches.

Another issue with PMMA, purely from a characterization standpoint, is its notorious instability when exposed to an electron beam during SEM imaging. PMMA features inspected with a SEM will broaden and distort within seconds of exposure. There are ways to avoid this—using single, fast scans and coating the PMMA film with metal are the most common—but at the length scales we are interested in, accurate direct imaging of PMMA in a SEM is essentially impossible. This means that the PMMA pattern will either have to be transferred to a stronger material for imaging (as is the case with the results in section 2.4) or an alternate, less destructive imaging technique such as atomic force microscopy (AFM) must be used. Both approaches have disadvantages, however; even the best pattern-transfer process will slightly degrade the resolution of the resist pattern being transferred, and AFM imaging is difficult when the features being imaged are on the order of the AFM tip diameter. In most cases these issues can be ignored but, again, at sub-10-nm-pitch length scales, even a lost nanometer or two can lead to a 10-20% measurement error. As a result, accurately imaging nanoscale PMMA patterns remains a nontrivial problem even if the issue of mechanical stability is solved.

5.1.2 HSQ

Many of PMMA's inherent problems can be circumvented by using HSQ as a resist instead. A negative resist, HSQ hardens into a glass-like substance when exposed to an electron beam; the resulting developed pattern is mechanically durable, a good etch mask, and can be directly imaged in a SEM with little effort. The bulk of our SEBL

characterization work has been done using HSQ for these reasons but unfortunately, when the sub-10-nm length scale is reached, HSQ has unique problems of its own.

Again, improvements in processing (in this case, the "salty development" process developed by Yang et al) have increased the contrast of HSQ to the point where it is no longer a concern. The best resolution achieved using HSQ is approximately a 10-nm pitch though, which is still more than a factor of two wider than the incident beam diameter. The cause of this most likely lies, again, in the development mechanics. While HSQ, unlike PMMA, does not typically suffer from collapse during development, its development rate exhibits a unique, nonlinear behavior, essentially dropping to zero after 60 seconds of development. The cause of this is unknown, but it seems to be a fairly inherent property of the resist; variations on the developer chemistry had little effect on it. This nonlinear development is a problem because, as was shown in detail in section 4.5, resist development in narrow gaps is typically diffusion-limited and proceeds much more slowly than development of wide areas. Knowing that, it seems likely that the developer cannot diffuse down into small gaps fast enough to fully develop them away before the unknown reaction-stopping mechanism occurs. Again, two possibilities have been suggested for circumventing this (ultrasonic development and elevated developer temperature) but both have issues of their own--ultrasound affects the mechanical stability of small features and alkaline developers can attack silicon substrates at high temperatures—and have not, at this point, been shown to be capable of solving this problem.

5.2 Metrology Limitations

Inspecting and accurately measuring sub-10-nm features can be nearly as difficult as fabricating them, and in some cases even more so. The scanning electron microscope (SEM) was used for the vast majority of the characterization work in this thesis due to its ease of use and the fact that its imaging resolution should, in principle, be as high as the resolution of the SEBL features being examined (particularly if, as in our case, the microscopy and lithography are being done on the same system). In practice, though, low-frequency vibration noise in our system, while it did not significantly affect the lithography, limited the imaging capabilities of our tool to the point where we could not inspect the features we were writing. Using a SEM with better vibration isolation mitigated this somewhat, but ultimately we were forced to turn to transmission electron microscopy (TEM), which has a resolution several times higher than even the best SEBL tools. The drawback of TEM is the high difficulty of preparing compatible samples (see section 3.6 for details), but the improvement in resolution suggests that all sub-10-nm characterization requiring a high degree of accuracy should be done with a TEM, rather than a SEM.

5.3 Summary

Although unresolved issues with resist development kept us from reaching our theoretical minimum resolution, we have successfully patterned features smaller than 10 nm in both PMMA and HSQ, the two most common electron beam resists. By fully characterizing

the relationship between contrast and temperature, and in the process clarifying some of the specifics of the exposure mechanism, we were able to optimize the contrast of PMMA and fabricate (and transfer via plasma-etch) lines as small as 8 nm, nearly a factor of two improvement over the best possible room-temperature processing.

By fully characterizing the behavior of the electron beam when traveling through HSQ and selecting process parameters to minimize its effect on resolution, we were able to fabricate dense features with half-pitches as small as 5 nm using beam energies as low as 10 KeV. While imaging these small features proved somewhat problematic, we were able to use a combination of TEM and vibration-isolated SEM imaging to clearly see the patterns. While still larger than the theoretical minimum possible feature size, we believe these structures to be among the smallest fabricated using conventional resist-based scanning electron beam lithography.

The bilayer process for fabricating Josephson junctions and other liftoff-based structures described in chapter 4 is an example of one application of high-resolution electron beam lithography. By using a resist bilayer and generating undercut profiles lithographically, the process allows very thin PMMA to be used as an imaging layer, eliminating the effects of beam scattering on resolution while still allowing for a reliable, robust liftoff. The result is a metallization process with a repeatable resolution on the order of 10 nm, among the highest reported for this type of process. A side benefit of developing this process is that the characterization of the undercut saturation effect, and the development model that resulted, was integral in explaining the HSQ development issues in chapter 3.

5.4 Further Work

With resist contrast and electron beam scattering effectively removed as barriers to resolution, pushing further into the sub-10-nm regime with SEBL appears to be primarily a materials issue. Both HSQ and PMMA have development issues that limit their resolution even in the best lithographic circumstances. Finding a way to stabilize PMMA features during development or neutralize the reaction-halting effect seen during HSQ development is the most likely path to the next breakthrough in resolution. Other electron beam resists may also be the key; fully characterizing the development behavior of calixerene or ZEP (to name two other relatively common resists) could show that one is a high-contrast resist with the relatively linear development of PMMA and the robust mechanical characteristics of HSQ. Whatever the details, solving this new problem should, barring the appearance of any heretofore unknown limiting factors, allow electron beam resolution to push deep in to the sub-10-nm regime, and possibly even reach its theoretical limit of structures with beam-sized pitches.

Appendix A: Monte Carlo Source Code

Since most freely-available Monte Carlo electron-beam simulators are designed for microscopy, rather than lithography, applications, we decided to write our own. Our simulator differs from CASINO and similar software in that it takes secondary, as well as primary electrons into account. It also measures the energy deposited in the film by the beam, rather than simply keeping track of electron trajectories.

The new software is heavily based on the single-scattering model published in David Joy's 1995 book on the subject.[72] The key differences are that the code was ported from PASCAL to Visual Basic 6.0 and that the output style was changed. While Joy's original program showed the simulation results as graphical representations of the electron trajectories, our software outputs a 2D array containing the accumulated energy distribution in the resist film. The array can then be processed by MATLAB, Origin, or other data-analysis software. For simplicity and speed of programming, no graphical output was implemented in our software, and like Joy's code only a single, suspended film of a given material and thickness can be analyzed.

A.1 Interface

As part of the process of porting the code to VB6, we added a basic GUI where the user can easily define the simulation parameters. The main GUI screen is shown in figure A-1. All the major user-definable simulation parameters are set here, including material

type (characterized by atomic number, atomic weight, and density; several common materials are preprogrammed or the user can add custom parameters), film thickness, primary beam energy, and the full-width half-maximum (FWHM) of the initial Gaussian beam profile. The program can track electrons until a given number of either primaries or secondaries (the user can determine which) is reached, and the maximum count is set here as well. Finally, the program can record the energy contributions from primaries alone, secondaries alone, or all electrons, and the 3D energy distribution can be converted to 2D by either integrating across one of its dimensions or taking a thin slice through the center. An option to ignore electrons that travel straight through the film without colliding was added for debugging purposes but not used in any simulations where data was taken.

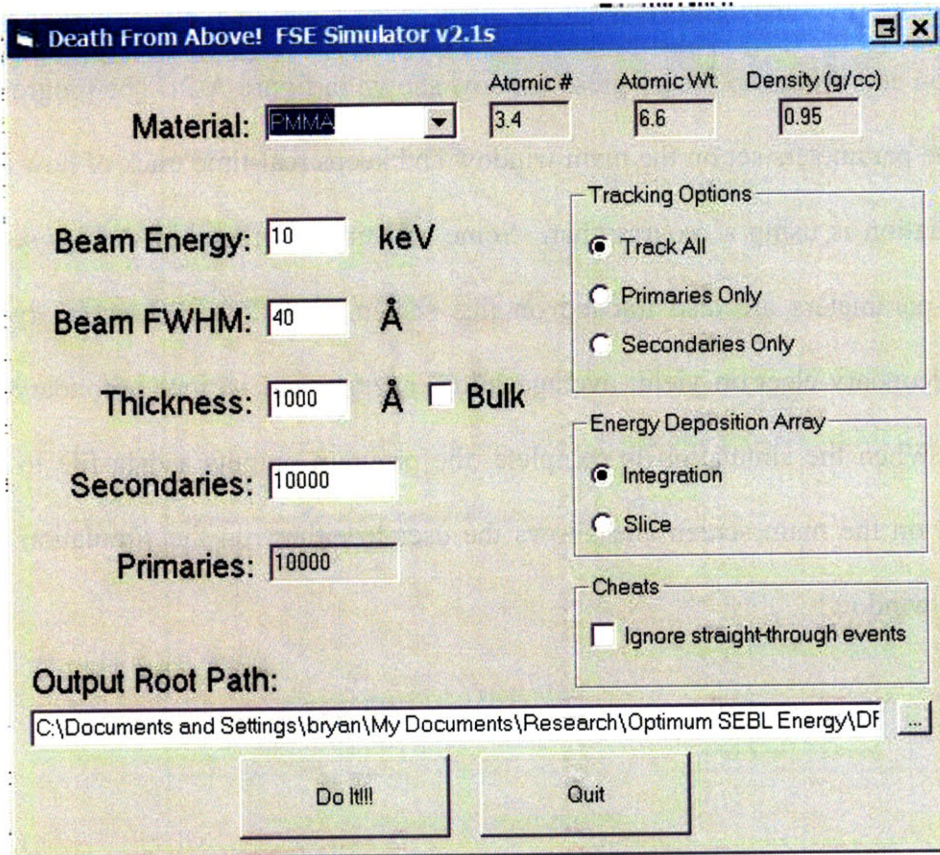

Figure A-1: Screenshot of the home window of Death From Above!, our electron-beam simulation software. The simulation parameters, such as beam energy, beam width, and film thickness and type are all set here. In addition, the user can tell the software whether to count primaries (run until a certain number of primary trajectories is reached) or secondaries (run until a certain number of secondary electrons are generated), and how high to count in each case. The program can track the energy deposited by primary electrons, secondary electrons, or both, and convert the 3D energy distribution to a 2D array by either integrating across one dimension or taking a thin slice through the center. Finally, the program can be forced to ignore electrons that travel straight through the resist without interacting; this was used primarily for debugging purposes.

When all the parameters are set on the main screen, the "Do It!!!" button starts the simulation and brings up the progress window shown in figure A-2. The progress screen shows the parameters set on the main window and keeps real-time track of how far along the simulation is using a progress bar. Some real-time averages of various secondary-electron parameters are also tracked on this screen, including the secondary-electron count, secondary-electron yield, average initial energy, and various secondary-electron ranges. When the simulation is complete, the program outputs a data file to the path specified on the main screen and allows the user to either run the simulation again or close the window.

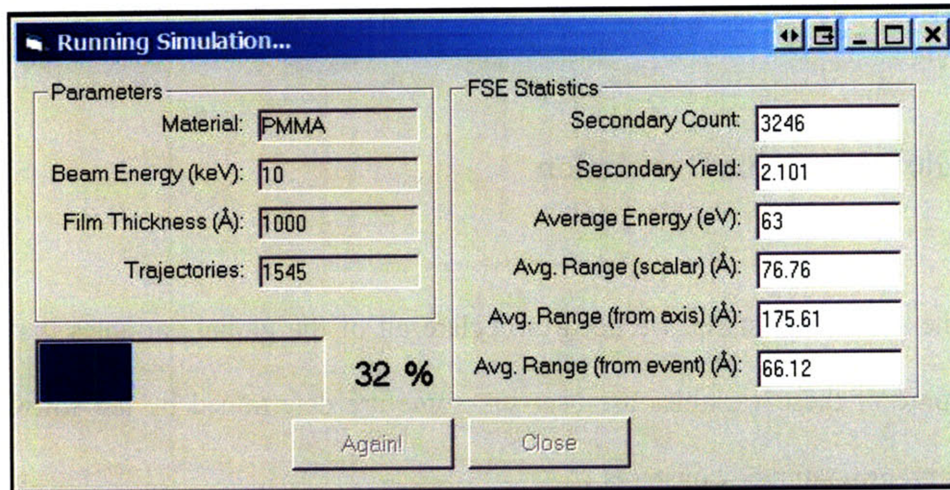

Figure A-2: Simulation progress window. The simulation's parameters (and a running count of trajectories tracked) are shown on the left, and a meter indicating the simulation's progress is shown below. The box on the right keeps real-time track of some secondary-electron statistics, including count, yield (the number of secondaries produced per primary), initial energy, and final range from both the generation point and the beam axis, as well as total scalar distance travelled. When the simulation is complete, an output file is generated in the directory specified on the main screen and the user has the option to either re-run the simulation or close the window.

A.2 Source Code

The full source code of the program (aside from data-display routines and other ancillary functions) is reproduced below. Aside from being in a different language, its flow and structure are very similar to Joy's original implementation, with most of the major

changes being due to the switch from a procedural to an object-oriented programming language.

A.2.1 Global Variable Declaration

Before the simulation starts, we need to declare all of the global variables that will be used. Some of these variables are user-set, some are determined by the software, and some are preprogrammed constants.

```
' Declare the variables we'll need in the simulation

' *********************************** CONSTANTS ******************************
Private Const MIN_ENERGY = 0.05 ' the minimum energy to track in keV; 50 eV is reasonable
Private Const TWO_PI = 6.2832
Private Const ED_SLICE = 5 ' the half-width of the energy density array "slice" if we're
not integrating it, in angstroms
Private Const UNIT_CONVERT = 1 ' used to change the final units of the energy density
plot. 1 is angstroms, 10 is nm, etc
Private Const PLOT_WIDTH = 1000 ' total width of the energy density plot, in angstroms
Private Const STOP_PWR_MULTIPLIER = 0.00000001 'multiplier to get the stopping power into
the right units. 1e-8 in Joy's book
' ****************************************************************************


' ****************************** SIMULATION PARAMETERS ************************

' these variables are grabbed from the initial form when the "Go" button is pressed.

Public SaveDirectory As String ' directory to save the results to
Public TodaysDate As String ' the date
Public CurrentTime As String ' the time
Private OutputPath As String ' the full path of the output file

Public AtomicNumber As Double ' the atomic number of the film material
Public AtomicWeight As Double ' the atomic weight of the film
Public Density As Double ' the film density, in g/cm3
Public BeamEnergy As Double ' the beam energy, in KeV
Public FWHM As Double ' the initial FWHM of the beam, in nm
Public Thickness As Long ' the film thickness, in angstroms
Public Bulk As Boolean ' if this is set to true, the film thickness is infinite and
Thickness is ignored
Public ED_Halfwidth As Long ' the half-width of the slice to integrate the deposited
energy plot over, in angstroms

Public IgnoreStraightThrough As Boolean ' if true, electrons that pass through the film
without collisions are ignored
Public CountSecondaries As Boolean ' if true, ElectronCount counts secondaries; otherwise
it counts primaries
```

```
Public TrackSecondaries As Boolean ' if true, secondaries are tracked, otherwise they're
ignored
Public TrackPrimaries As Boolean ' similarly, this ignores the contribution from
primaries if false

' these variables are altered by the simulation itself

Public ElectronCount As Long ' the running count of tracked electrons (primary or
secondary, depending on form input)
Public TotalElectrons As Long ' the total number of electrons to track
Public Trajectories As Long ' the running total of trajectories tracked
Public TotalFSE As Long ' the integrated energy of all secondaries to date, used to
compute the average energy
Public StraightThrough As Long ' this just tells us if the currently-tracked electron
went straight through the film
' ****************************************************************************



' ****************************** INTERNAL VARIABLES **************************

' these are all the (private) variables used internally by the simulation.

Private MIP As Double ' the mean ionization potential in eV
Private Lambda0 As Double ' the energy-independent part of the mean free path
Private er As Double ' relativistic beam energy correction
Private a1_a, sg_a As Double ' the energy-independent parts of the Rutherford cross-
section
Private FSEProbability As Double ' the probability of generating a FSE

Private cp, SP, ga As Double ' the three variables holding the current electron's scatter
angles

Private OldCoords As New xyz ' the old and new XYZ coordinates of the current electron
Private NewCoords As New xyz ' the xyz type is just a data structure that holds 3D
coordinates

Private OldCosines As New xyz ' the old and new direction cosines of the current electron
Private NewCosines As New xyz

' running integrations of various energies, used to calculate averages
Private TotalFSEEnergy, TotalFSEBethe, TotalFSEAxis, TotalFSEEvent As Double

' counts of the SEs tracked as well as backscattered and transmitted electrons
Private TrackedFSECount, FSECount, BSCount, TXCount As Long
Private FSEYield As Double ' the SE yield (the number of secondaries generated per
primary)

' the big array that holds the deposited energy density information
Private EDArray() As Double
Private EDArrayX, EDArrayY As Long ' dimensions of EDArray
' ****************************************************************************
```

A.2.2 The XYZ Data Type

Since we are using 3D coordinates to keep track of electrons' positions in the film, it makes sense to define a data type to make working with coordinate triplets easier. The "xyz" data structure is designed to hold a single triplet, and also contains several methods to simplify common tasks, such as copying one triplet's coordinates to another.

```
' ******************************** CLASS 'XYZ' ********************************
' a simple data structure for 3D coordinates. It's pretty generic, so it can be used
' for both the XYZ coordinates and the directional cosine triplets in the main program.
' Contains both the actual coordinates and a couple of helpful methods for doing
' repetitive things with them.
' ****************************************************************************


' declare the actual variables
Public x As Double
Public y As Double
Public z As Double

Private Sub Class_Initialize()
' set everything to zero when a new xyz object is created

x = 0
y = 0
z = 0

End Sub

Public Sub Zero(cosines As Boolean)

' zero the triplet. If we're using it to store cosines, rather than coordinates, the
third value
' should "zero" to 1. The boolean argument tells us whether to do this or not.

If cosines = True Then
    x = 0
    y = 0
    z = 1
Else
    x = 0
    y = 0
    z = 0
End If

End Sub

Public Sub SetCoordinates(NewXYZ As xyz)
' easily transfer the values of one xyz triplet to another one (basically an assignment
operator)
```

```
x = NewXYZ.x
y = NewXYZ.y
z = NewXYZ.z

End Sub

Public Function distance(vector As xyz) As Double
' find the magnitude of a vector between these XYZ coordinates and another set
' provided in the argument

distance = Sqr((x - vector.x) ^ 2 + (y - vector.y) ^ 2 + (z - vector.z) ^ 2)

End Function
```

A.2.3 Main Program Loop

This section is the part of the program that is actually run when the simulation is started. It consists of one large loop (the MonteCarloLoop subroutine) and several ancillary subroutines and functions.

```
Public Sub MonteCarloLoop()

' This is the guts of the program. Note that it's public; the main form runs
' this routine when the "Go" button is pressed.

' Define some local variables we're going to need
Dim Energy, TravelDistance, TestForFSE, vector As Double
Dim i, j As Long ' accumulators

Dim TrackCoord As New xyz

' zero some variables first of all
ElectronCount = 0
Trajectories = 0
TotalFSEEnergy = 0
TotalFSEBethe = 0
TotalFSEAxis = 0
TotalFSEEvent = 0
ElectronCount = 0
TrackedFSECount = 0
BSCount = 0
TXCount = 0
FSEYield = 0
StraightThrough = 0
FSECount = 0

Randomize ' reset the random number generator

Call getConstants ' set up the constants we'll need
```

```
' *************************** MAIN PROGRAM LOOP ******************************

While ElectronCount < TotalElectrons

    ' if we're not counting secondaries, add this primary to ElectronCount
    ' (the variable that tells us when we're done simulating). Either way
    ' add it to Trajectories, which just counts the number of primaries run.
    If Not CountSecondaries Then
        ElectronCount = ElectronCount + 1
    End If
    Trajectories = Trajectories + 1

    ' zero all the coordinates and cosines
    OldCoords.Zero (False)
    NewCoords.Zero (False)
    OldCosines.Zero (True)
    NewCosines.Zero (True)

    ' ***********************************************************************
    'calculate the entrance point, assuming a gaussian beam with the given FWHM

    sigma = FWHM / 2.35 ' get the st. dev. from the FWHM

    ' need a nonzero random number here
    nzRnd = Rnd
    If nzRnd = 0 Then
        nzRnd = 0.000001
    End If

    r = sigma * (-2 * Log(nzRnd)) ^ 0.5 ' the radial distance from the beam axis
    theta = TWO_PI * Rnd ' the angular position is random

    ' set OldCoords and NewCoords to the starting position
    OldCoords.x = Round(r * Cos(theta))
    OldCoords.y = Round(r * Sin(theta))
    Call NewCoords.SetCoordinates(OldCoords)
    ' ***********************************************************************



    Energy = BeamEnergy 'the initial energy is the beam energy, believe it or not

    nzRnd = Rnd
    If nzRnd = 0 Then
        nzRnd = 0.000001
    End If

    TravelDistance = -getMFP(Energy) * Log(nzRnd) 'the first step distance, in angstroms
    NewCoords.z = TravelDistance ' set the new z-coordinate. we assume the electron went
    ' straight in, so the x and y coordinates don't change on this step.


    ' calculate the stopping power and the energy lost on this step
    dE = StoppingPower(Energy) * Density * STOP_PWR_MULTIPLIER * TravelDistance
    Energy = Energy - dE

    ' update the coordinates
    OldCoords.z = NewCoords.z

    If NewCoords.z > Thickness Then ' check if it just went straight through
```

```
        'record the energy deposition, unless we're ignoring the straight-through cases
        If Not IgnoreStraightThrough Then
            ' here we're populating EDArray with the energy deposited by the electron as
             it traveled through the film
            For q = 0 To Thickness - 1

                ' basically, if it's in the film and within the bounds of the 'slice'
                 defined by ED_HALFWIDTH, we
                ' record the energy it deposited in each 1-angstrom voxel it passed
                 through in the process. Note
                ' that if we're in 'integrate' mode, ED_HALFWIDTH is set to a large,
                 basically infinite value
                ' so all energies get taken into account.

                If NewCoords.y <= ED_Halfwidth And NewCoords.y >= -ED_Halfwidth And
                 NewCoords.z > 0 Then

                    If NewCoords.x < PLOT_WIDTH / 2 And NewCoords.x > -PLOT_WIDTH / 2
                     Then
                        EDArray(Round(NewCoords.x / UNIT_CONVERT) + EDArrayX / 2, q /
                        UNIT_CONVERT) = EDArray(Round(NewCoords.x / UNIT_CONVERT) +
                        EDArrayX / 2, q / UNIT_CONVERT) + StoppingPower(Energy) * Density
                        * STOP_PWR_MULTIPLIER
                    End If
                End If
            Next

        End If

        ' update some counts
        TXCount = TXCount + 1
        StraightThrough = StraightThrough + 1
    Else

        ' if the electron didn't go straight through, we've got some work to do....

        If TrackPrimaries Then

            ' if we're tracking primaries, add the energy deposited in the first step to
             the array as we did
            ' in the straight-through case above.

            For q = 0 To TravelDistance - 1
                If q < Thickness - 1 Then
                    If NewCoords.y <= ED_Halfwidth And NewCoords.y >= -ED_Halfwidth And
                     NewCoords.z > 0 And NewCoords.z < Thickness Then

                        If NewCoords.x < PLOT_WIDTH / 2 And NewCoords.x > -PLOT_WIDTH / 2
                         Then

                            EDArray(Round(NewCoords.x / UNIT_CONVERT) + EDArrayX / 2,
                            Round(NewCoords.z / UNIT_CONVERT)) =
                            EDArray(Round(NewCoords.x / UNIT_CONVERT) + EDArrayX / 2,
                            Round(NewCoords.z / UNIT_CONVERT)) + StoppingPower(Energy) *
                            Density * STOP_PWR_MULTIPLIER

                        End If
                    End If
                End If
            Next

        End If
```

```
Do While Energy >= MIN_ENERGY ' now we track the electron until it escapes or
 runs out of energy

    Randomize ' reset the RNG again for good measure

    nzRnd = Rnd
    If nzRnd = 0 Then
        nzRnd = 0.000001
    End If

    TravelDistance = -getMFP(Energy) * Log(nzRnd) ' get the next step distance,
     using the new energy


    ' Now check if the collision at the end of this step is elastic or inelastic
    ' (i.e. did we create a secondary electron?)

    TestForFSE = Rnd 'i can haz secundry?
    If TestForFSE > FSEProbability Then
        ' if we did make a secondary, FSETrack will track it until it escapes or
         dies, then come back here.
        ' it also sets Energy to take into account the energy lost by the primary
         in the inelastic collision
        Energy = FSETrack(Energy)
        FSECount = FSECount + 1
        If CountSecondaries Then
            ' if we're counting secondaries, now we're one closer to being done
            ElectronCount = ElectronCount + 1
        End If

        ' recalculate the SE yield
        FSEYield = FSECount / Trajectories
    Else
        ' if it was an elastic collision, just recalculate the trajectory
        Call GetScatterAngles(Energy) ' get new scattering angles
    End If

    Call GetNewCoordinates(TravelDistance) ' calculate new coordinates based on
     how far we traveled

   ' check and see if it passed into the y-plane defined by ED_Halfwidth where
     we're tracking deposited energy,
   ' and if it did record, how much energy was deposited there.
   If TrackPrimaries Then

        ' this large conditional checks to see if the last step passed through
         the 'tracking' plane, using a variety of tests.
        If (NewCoords.y <= ED_Halfwidth And NewCoords.y >= -ED_Halfwidth) Or
         (OldCoords.y <= -ED_Halfwidth And NewCoords.y >= ED_Halfwidth) Or
         (OldCoords.y >= ED_Halfwidth And NewCoords.y <= -ED_Halfwidth) Or
         (OldCoords.y <= ED_Halfwidth And OldCoords.y >= -ED_Halfwidth) Then

            ' if it did pass through the plane, we need to calculate the energy
              it deposited while it was in there.

            vector = TravelDistance 'find the length of the last path

            For j = 0 To Round(vector)
                'check each angstrom of the path to see if it's in the zone
                TrackCoord.x = OldCoords.x + j * NewCosines.x
                TrackCoord.y = OldCoords.y + j * NewCosines.y
                TrackCoord.z = OldCoords.z + j * NewCosines.z
```

```
                        'if the current angstrom is in the y-plane, deposit the energy in
                        the correct xz coordinate of the array
                        If TrackCoord.y <= ED_Halfwidth And TrackCoord.y >= -ED_Halfwidth
                        And TrackCoord.z > 0 And TrackCoord.z < Thickness Then

                            ' make sure it's within the plot width!
                            If TrackCoord.x < PLOT_WIDTH / 2 And TrackCoord.x > -
                            PLOT_WIDTH / 2 Then

                                EDArray(Round(TrackCoord.x / UNIT_CONVERT) + EDArrayX /
                                2, Round(TrackCoord.z / UNIT_CONVERT)) =
                                EDArray(Round(TrackCoord.x / UNIT_CONVERT) + EDArrayX / 2,
                                Round(TrackCoord.z / UNIT_CONVERT)) +
                                StoppingPower(Energy) * Density * STOP_PWR_MULTIPLIER
                            End If
                        End If
                    Next

                End If
            End If

            ' having done all that, recalculate the stopping power and electron energy
             for the next step
            dE = StoppingPower(Energy) * Density * STOP_PWR_MULTIPLIER * TravelDistance
            Energy = Energy - dE

            ' now check and see if it's still in the film
            If NewCoords.z <= 0 Then ' OH LOOK IT BACKSCATTERED
                BSCount = BSCount + 1
                Exit Do ' it got away; we're done with this electron

            ElseIf NewCoords.z >= Thickness Then ' IT DONE GOT TRANSMITTED
                TXCount = TXCount + 1
                Exit Do ' I'LL GET YOU NEXT TIME

            Else ' if it's still in there, calculate how much energy it's got left
                Call ResetForNextStep ' this gets all the variables ready for the next
                 iteration
            End If

        Loop

    End If

    Call UpdateDisplay(i) ' update the program's display window

Wend

' Now we have a 2D array with all the energy deposited by all the primary electrons we
ran, as well as the secondaries they generated. So what do we do with it?

' ****************************************************************************
' programming is hard and MATLAB already has nice data-display routines, so we'll dump
' EDArray into a giant text file and let MATLAB deal with it from there.
' ****************************************************************************

Dim OutputFilename As String

' set the path for the output file, creating a subdirectory of the format
THICKNESS_MATERIAL_DATE_TIME
OutputPath = SaveDirectory + "\" + Str(Thickness / 10) + "nm_" +
MainFrm.MaterialSelect.Text + "_" + TodaysDate + "_" + CurrentTime
```

```
' check if the directory exists and create it if it doesn't
Dim FSO, stream
Set FSO = CreateObject("Scripting.FileSystemObject")
If Not FSO.folderexists(OutputPath) Then
    FSO.createfolder OutputPath
End If
If Not FSO.folderexists(OutputPath + "\logs") Then
    FSO.createfolder OutputPath + "\logs"
End If

' the output filenames have the format ENERGY_THICKNESS_TRAJECTORIES.TXT
OutputFilename = OutputPath + "\" + Str(BeamEnergy) + "keV_" + Str(Thickness / 10) +
"nm_" + Str(Trajectories) + ".txt"

Open OutputFilename For Output As #1

' dump EDArray into the output file
For j = 0 To EDArrayY - 1
    For i = 0 To EDArrayX - 1
        Print #1, EDArray(i, j); ",";
    Next
    Print #1, " "
Next

Close #1

' ** Make a little log file with info about the simulation in a subdirectory **

Dim LogFilename As String
LogFilename = OutputPath + "\logs\" + Str(BeamEnergy) + "keV_" + Str(Thickness / 10) +
"nm_" + Str(Trajectories) + ".log"

Open LogFilename For Output As #2
Print #2, "Date: "; Date
Print #2, "Time: "; Time
Print #2, "Voltage: "; Str(BeamEnergy); " KeV"
Print #2, "Beam Width: "; Str(Round(FWHM / 10)); " nm"
Print #2, "Film Type: "; MainFrm.MaterialSelect.Text
Print #2, "Film Thickness: "; Str(Round(Thickness / 10)); " nm"

If MainFrm.optEDArrayType(0).Value = True Then
    Print #2, "Energy Deposition Array Type: Integration"
Else
    Print #2, "Energy Deposition Array Type: Slice"
End If

If MainFrm.chkIgnoreStraightThrough.Value = True Then
    Print #2, "Ignoring Straight-Through Events: Yes"
Else
    Print #2, "Ignoring Straight-Through Events: No"
End If

Print #2, " "

If MainFrm.optPriSecAll(0).Value = True Then
    Print #2, "Tracking: Primaries and Secondaries"
    Print #2, "Primary Electrons: "; Str(Trajectories)
    Print #2, "Secondary Electrons: "; Str(FSECount)
    Print #2, "SE Yield: "; Str(Round(FSEYield, 3))
    Print #2, "SE Avg. Energy: "; Str(Round(TotalFSEEnergy * 1000 / FSECount, 0)); " eV"
    Print #2, "SE Avg. Range (from event): "; Str(Round((TotalFSEEvent / TrackedFSECount)
```

```
    / 10, 2)); " nm"
    Print #2, "SE Avg. Range (from axis): "; Str(Round((TotalFSEAxis / TrackedFSECount) /
    10, 2)); " nm"
    Print #2, "SE Avg. Range (scalar): "; Str(Round((TotalFSEBethe / TrackedFSECount) /
    10, 2)); " nm"

ElseIf MainFrm.optPriSecAll(1).Value = True Then
    Print #2, "Tracking: Primaries Only"
    Print #2, "Primary Electrons: "; Str(Trajectories)
Else
    Print #2, "Tracking: Secondaries Only"
    Print #2, "Secondary Electrons: "; Str(FSECount)
    Print #2, "SE Yield: "; Str(Round(FSEYield, 3))
    Print #2, "SE Avg. Energy: "; Str(Round(TotalFSEEnergy * 1000 / FSECount, 0)); " eV"
    Print #2, "SE Avg. Range (from event): "; Str(Round((TotalFSEEvent / TrackedFSECount)
    / 10, 2)); " nm"
    Print #2, "SE Avg. Range (from axis): "; Str(Round((TotalFSEAxis / TrackedFSECount) /
    10, 2)); " nm"
    Print #2, "SE Avg. Range (scalar): "; Str(Round((TotalFSEBethe / TrackedFSECount) /
    10, 2)); " nm"
End If

' *********************** End log file creation code ****************************

Close #2

End Sub

Private Sub getConstants()
    ' this just calculates all the values the program needs to do the simulation.
    ' i've cleverly combined this all into one oversized subroutine

    'calculates the mean ionization potential in KeV
    'using the Berger-Selzer fit with atomic number
    MIP = (9.768 * AtomicNumber + (58.5 / AtomicNumber ^ 0.19)) * 0.001

    'energy-independent part of the alpha term (see Joy pg 28)
    a1_a = 0.00343 * AtomicNumber ^ 0.667

    'relativistic correction to the beam energy
    er = ((BeamEnergy + 511#) / (BeamEnergy + 1022#)) ^ 2

    'energy-independent bits of the rutherford cross-section (see Joy pg 27)
    sg_a = AtomicNumber ^ 2 * 12.56 * 5.21E-21 * er

    'the energy-independent parts of the mean free path (lambda)
    Lambda0 = AtomicWeight / (Density * 6E+23) 'lambda in cm
    Lambda0 = Lambda0 * 100000000# 'put it into angstroms

    'set the height and width of the energy density array
    EDArrayX = PLOT_WIDTH / UNIT_CONVERT 'the x dimension is fixed at PLOT_WIDTH (100 nm
here)
    EDArrayY = Round(Thickness / UNIT_CONVERT, 0) 'the y dimension is just the thickness
in nm
    ReDim EDArray(EDArrayX, EDArrayY) 'set the array dimensions

End Sub


Private Function getMFP(Energy) As Double

    ' calculate the mean free path of a primary electron. Note that we
```

```
    ' have to calculate both the elastic and inelastic mean free paths
    ' here; the actual MFP is determined by reciprocal-adding the two.

    Dim a1, ak, sg, EMFP, IMFP, MFP As Double

    ' compute the elastic mean free path (EMFP) for a given energy
    a1 = a1_a / Energy ' get the 'real' alpha (see Joy pg 28)

    'sg is the screened rutherford xsec (in cm2)
    ak = a1 * (1# + a1)
    sg = sg_a / (ak * Energy ^ 2)

    'the EMFP (in angstroms) is...
    EMFP = Lambda0 / sg

    ' check to see if we're tracking secondaries in this particular simulation
    If TrackSecondaries Then
        ' if we are, calculate the inelastic mean free path using the Evans x-sec
        IMFP = AtomicWeight * (Energy ^ 2) * 2.55 / (Density * AtomicNumber)
    Else
        ' if we're not tracking SEs, just set the IMFP to a high number so it
        ' will cancel when we reciprocal-add it
        IMFP = 100000000000#
    End If

    ' Use the two to get the total MFP
    MFP = (EMFP ^ -1 + IMFP ^ -1) ^ -1 'just like resistors in parallel

    'to figure out the probability of FSE production, use the ratio MFP/EMFP
    'note that this comes out to zero if we're not tracking secondaries
    FSEProbability = MFP / EMFP

    'aaaand we're done!
    getMFP = MFP

End Function

Private Sub UpdateDisplay(i)

' this subroutine updates the numbers on the display form (frmCalculate), as well as the
progress bar

' only update every 1000 trajectories, to save the computer some headache
If (i Mod 1000) <> 0 Then
    Exit Sub
End If


' update the display values

frmCalculate.lblTrajectories = Trajectories
frmCalculate.txtSECount = FSECount
frmCalculate.txtSEYield = Round(FSEYield, 3)
If TrackedFSECount > 0 And FSECount > 0 Then ' make sure we're not dividing by zero
    frmCalculate.txtEnergy = Round(TotalFSEEnergy * 1000 / FSECount, 0)
    frmCalculate.txtBetheRange = Round(TotalFSEBethe / TrackedFSECount, 2)
    frmCalculate.txtAxisRange = Round(TotalFSEAxis / TrackedFSECount, 2)
    frmCalculate.txtEventRange = Round(TotalFSEEvent / TrackedFSECount, 2)
End If

' update the progress bar
```

```
If FSECount > frmCalculate.pbPctDone.Max Then
    frmCalculate.pbPctDone.Value = frmCalculate.pbPctDone.Max
Else
    frmCalculate.pbPctDone.Value = ElectronCount
End If

' update the percent-done label
frmCalculate.lblPctDone.Caption = Round((ElectronCount / TotalElectrons) * 100, 0)

' if we're done, enable the redo/close buttons

If frmCalculate.lblPctDone.Caption = "100" Then
    frmCalculate.cmdAgain.Enabled = True
    frmCalculate.cmdClose.Enabled = True

End If

'force the forms to completely redraw before we exit
MainFrm.Refresh
frmCalculate.Refresh

End Sub


Private Sub GetScatterAngles(Energy)

' uses the screened Rutherford xsec to calculate new scatter angles for the primary
' see Joy pg 27 for more info

Dim R1, a1 As Double

a1 = a1_a / Energy
R1 = Rnd

cp = 1# - ((2# * a1 * R1) / (1# + a1 - R1))
SP = Sqr(1# - cp * cp)
ga = TWO_PI * Rnd ' azimuthal scatter angle is just random

End Sub

Private Sub GetNewCoordinates(step)

' computes the new coordinates for the electron
' using the scattering angles found earlier
' transforms coordinates back to laboratory frame

' step is just the distance traveled during the previous step

Dim V1, V2, V3, V4, an_m, an_n As Double

If OldCosines.z = 0 Then
    OldCosines.z = 0.000001 ' dividing by zero is bad
End If

' get the transformation terms (see Myklebust et al 1976 for derivation)[75]
an_m = -OldCosines.x / OldCosines.z
an_n = 1# / Sqr(1 + (an_m * an_m))
V1 = an_n * SP
V2 = an_m * an_n * SP
V3 = Cos(ga)
```

```
V4 = Sin(ga)

' get the new direction cosines using the transcendentals above
NewCosines.x = (OldCosines.x * cp) + (V1 * V3) + (OldCosines.y * V2 * V4)
NewCosines.y = (OldCosines.y * cp) + (V4 * (OldCosines.z * V1 - OldCosines.x * V2))
NewCosines.z = (OldCosines.z * cp) + (V2 * V3) - (OldCosines.y * V1 * V4)

' hence the new coordinates are...
NewCoords.x = OldCoords.x + step * NewCosines.x
NewCoords.y = OldCoords.y + step * NewCosines.y
NewCoords.z = OldCoords.z + step * NewCosines.z

End Sub

Private Function ResetForNextStep() As Double

' This just resets the coordinates and cosines for the primary electron's next step

Call OldCosines.SetCoordinates(NewCosines)
Call OldCoords.SetCoordinates(NewCoords)

End Function
Private Function StoppingPower(Energy) As Double

' calculates the stopping power for a given electron energy, using
' Joy's modification of the Bethe equation

If Energy < MIN_ENERGY Then Energy = MIN_ENERGY ' make sure it's at least 50 eV or the
equation doesn't apply

'units are keV/gm/cm^2
StoppingPower = 78500 * AtomicNumber * (Log(1.166 * (Energy + 0.85 * MIP) / MIP)) /
(AtomicWeight * Energy)

End Function
```

A.2.4 Secondary Electron Tracking

When a primary electron generates a secondary in the main loop, the program temporarily ignores the primary and runs a subroutine called FSETrack that tracks the secondary through the solid until it either escapes or runs out of energy. This routine is essentially the same as the one in MonteCarloLoop, with the exception of the secondary electrons' inability to generate secondaries of their own.

```
Private Function FSETrack(PrimaryEnergy)

' this tracks secondary electrons until they escape or die. it's basically just
' another single-scattering loop like the one in MonteCarloLoop. A better programmer
' would have just written a generic procedure for both but I'm tired and hungry

' it also spits back the new energy of the primary that generated the secondary, taking
' the energy it lost in the inelastic collision event into account

' Define some local variables. You may recognize some of these...
Dim FSEnergy As Double ' the SE's energy
Dim epsilon, sa1, loss, vector As Double

Dim j As Long
Dim TrackCoord As New xyz

Dim NewSECoords As New xyz
Dim OldSECoords As New xyz
Dim NewSECosines As New xyz
Dim OldSECosines As New xyz
Dim InitialSECoords As New xyz

Dim ssp, scp, sga As Double
Dim V1, V2, V3, V4, an_m, an_n, dFSE As Double

Dim BetheRange, AxisRange, EventRange As Double
Dim ThisBetheRange, EscapeLength As Double
Dim NonZeroRandom As Double

'get the initial energy of the secondary
epsilon = (1000 - 998 * Rnd) ^ -1 ' the fraction of the primary energy transferred to the
SE (see Joy pg 151)
FSEnergy = PrimaryEnergy * epsilon ' the actual SE energy
TotalFSEEnergy = TotalFSEEnergy + FSEnergy ' Update the total

' We're going to calculate the "Bethe Range" (scalar range of the SE) by adding up
' all its step distances in this variable, which we're starting at zero for obvious
reasons.
ThisBetheRange = 0

'grab the initial coordinates and stuff
Call OldSECoords.SetCoordinates(NewCoords)
Call InitialSECoords.SetCoordinates(NewCoords)
Call OldSECosines.SetCoordinates(NewCosines)

'initial coordinates are stored in OldSECoords and InitialSECoords and OldSECosines

loss = PrimaryEnergy - FSEnergy ' how much energy the primary lost generating the SE

' get the initial scattering angles
ssp = 2 * (1 - epsilon) / (2 + epsilon * FSEnergy / 511#)
scp = Sqr(1 - ssp)
ssp = Sqr(ssp)

If FSEnergy <= MIN_ENERGY Then

    ' if it's a low-energy SE don't bother tracking it, just dump the energy at the
      generation point

    FSETrack = loss
```

```
    If TrackSecondaries Then

        If InitialSECoords.y <= ED_Halfwidth And InitialSECoords.y >= -ED_Halfwidth And
         InitialSECoords.z > 0 And InitialSECoords.z < Thickness Then

            If InitialSECoords.x < PLOT_WIDTH / 2 And InitialSECoords.x > -PLOT_WIDTH / 2
             Then 'fix the x dimensions at 0.5um in each direction

                EDArray(Round(InitialSECoords.x / UNIT_CONVERT) + EDArrayX / 2,
                 Round(InitialSECoords.z / UNIT_CONVERT)) =
                 EDArray(Round(InitialSECoords.x / UNIT_CONVERT) + EDArrayX / 2,
                 Round(InitialSECoords.z / UNIT_CONVERT)) + StoppingPower(FSEnergy) *
                 Density * STOP_PWR_MULTIPLIER

            End If
        End If
    End If

Else

    ' if we get a live one, we have to follow it like we do with the primary electrons.

    Do

        ' this loop works almost exactly the same as the one in MonteCarloLoop, so I'll
        ' keep the comments to a minimum here. The main difference is that a lot of stuff
        ' in that loop that was done in subroutines isn't here, so the "guts" are more
        ' visible.

        Randomize

        nzRnd = Rnd
        If nzRnd = 0 Then
            nzRnd = 0.000001
        End If

        FSEStep = -getFSEMFP(FSEnergy) * Log(nzRnd) 'find the step length in angstroms
        sga = TWO_PI * Rnd ' get the (random) azimuthal scatter angle
        If OldSECosines.z = 0 Then OldSECosines.z = 0.0001 'don't divide by zero

        ' **** Calculate the new position and trajectory of the SE ****

        'get transcendentals (see Myklebust et al, 1976)...
        an_m = (-OldSECosines.x / OldSECosines.z)
        an_n = 1 / Sqr(1 + (an_m ^ 2))
        V1 = an_n * ssp
        V2 = an_n * an_m * ssp
        V3 = Cos(sga)
        V4 = Sin(sga)

        ' ...use them to find the new direction cosines...
        NewSECosines.x = (OldSECosines.x * scp) + (V1 * V3) + (OldSECosines.y * V2 * V4)
        NewSECosines.y = (OldSECosines.y * scp) + (V4 * (OldSECosines.z * V1 -
       OldSECosines.x * V2))
        NewSECosines.z = (OldSECosines.z * scp) + (V2 * V3) - (OldSECosines.y * V1 * V4)

        ' ...and get the new coordinates, finally!
        NewSECoords.x = OldSECoords.x + FSEStep * NewSECosines.x
        NewSECoords.y = OldSECoords.y + FSEStep * NewSECosines.y
        NewSECoords.z = OldSECoords.z + FSEStep * NewSECosines.z

        'check and see if it passed into the y-plane where we're tracking deposited
         energy
```

```
If TrackSecondaries Then

    ' make sure we're tracking secondaries, even though we should never have
     gotten here if we weren't

    If (NewSECoords.y <= ED_Halfwidth And NewSECoords.y >= -ED_Halfwidth) Or
     (OldSECoords.y <= -ED_Halfwidth And NewSECoords.y >= ED_Halfwidth) Or
     (OldSECoords.y >= ED_Halfwidth And NewSECoords.y <= -ED_Halfwidth) Or
     (OldCoords.y <= ED_Halfwidth And OldCoords.y >= -ED_Halfwidth) Then
        vector = NewSECoords.distance(OldSECoords) 'find the length of the last
                                                    path

        For j = 0 To Round(vector)
            'check each angstrom of the path to see if it's in the zone
            TrackCoord.x = OldSECoords.x + j * NewSECosines.x
            TrackCoord.y = OldSECoords.y + j * NewSECosines.y
            TrackCoord.z = OldSECoords.z + j * NewSECosines.z
            'if it's in the y-plane, deposit the energy in the correct xz
             coordinate of the array
            If TrackCoord.y <= ED_Halfwidth And TrackCoord.y >= -ED_Halfwidth And
             TrackCoord.z > 0 And TrackCoord.z < Thickness And TrackCoord.x <
             PLOT_WIDTH / 2 And TrackCoord.x > -PLOT_WIDTH / 2 Then

                EDArray(Round(TrackCoord.x / UNIT_CONVERT) + EDArrayX / 2,
                 Round(TrackCoord.z / UNIT_CONVERT)) = EDArray(Round(TrackCoord.x
                 / UNIT_CONVERT) + EDArrayX / 2, Round(TrackCoord.z /
                 UNIT_CONVERT)) + StoppingPower(FSEnergy) * Density *
                 STOP_PWR_MULTIPLIER

            End If
        Next

    End If
End If

'now see if it's still in the solid blah blah blah

If NewSECoords.z > Thickness Then

    ' *** Case #1: it got transmitted ***

    TXCount = TXCount + 1

    ' step 1: figure out exactly where it escaped
    EscapeLength = (Thickness - NewSECoords.z) / NewSECosines.z ' solve the new
     z-coordinate eqn in the main loop for z_new=thickness

    ' find the coordinates of the escape
    NewSECoords.x = OldSECoords.x + EscapeLength * NewSECosines.x
    NewSECoords.y = OldSECoords.y + EscapeLength * NewSECosines.y
    NewSECoords.z = Thickness

    ' since it's gone, calculate the various final ranges
    ThisBetheRange = ThisBetheRange + NewSECoords.distance(OldSECoords) ' scalar
     range
    AxisRange = Sqr(NewSECoords.x ^ 2 + NewSECoords.y ^ 2) ' distance from the
     beam axis (2D)
    EventRange = NewSECoords.distance(InitialSECoords) ' distance from the SE
     generation event (2D)

    ' add ranges to the totals and update the count
    TotalFSEAxis = TotalFSEAxis + AxisRange
    TotalFSEEvent = TotalFSEEvent + EventRange
    TotalFSEBethe = TotalFSEBethe + ThisBetheRange
    TrackedFSECount = TrackedFSECount + 1
```

```
        Exit Do
    ElseIf NewSECoords.z <= 0 Then

        ' *** case #2: it got backscattered ***

        BSCount = BSCount + 1

        EscapeLength = -NewSECoords.z / NewSECosines.z

        ' find the coordinates of the escape and update totals, same as in the
         transmitted case
        NewSECoords.x = OldSECoords.x + EscapeLength * NewSECosines.x
        NewSECoords.y = OldSECoords.y + EscapeLength * NewSECosines.y
        NewSECoords.z = 0

        ThisBetheRange = ThisBetheRange + NewSECoords.distance(OldSECoords)
        AxisRange = Sqr(NewSECoords.x ^ 2 + NewSECoords.y ^ 2)
        EventRange = NewSECoords.distance(InitialSECoords)

        TotalFSEAxis = TotalFSEAxis + AxisRange
        TotalFSEEvent = TotalFSEEvent + EventRange
        TotalFSEBethe = TotalFSEBethe + ThisBetheRange
        TrackedFSECount = TrackedFSECount + 1
        Exit Do
    Else
        '*** Case #3: if it's still around, calculate its new energy ***

        ' new stopping power, new energy
        dFSE = FSEStep * StoppingPower(FSEnergy) * Density * STOP_PWR_MULTIPLIER
        FSEnergy = FSEnergy - dFSE

        ' if it's below the minimum energy we're tracking, get the ranges and exit
        If FSEnergy <= MIN_ENERGY Then

            ' get ranges
            AxisRange = Sqr(NewSECoords.x ^ 2 + NewSECoords.y ^ 2)
            EventRange = NewSECoords.distance(InitialSECoords)
            ThisBetheRange = ThisBetheRange + NewSECoords.distance(OldSECoords)

            ' update totals and count
            TotalFSEAxis = TotalFSEAxis + AxisRange
            TotalFSEEvent = TotalFSEEvent + EventRange
            TotalFSEBethe = TotalFSEBethe + ThisBetheRange
            TrackedFSECount = TrackedFSECount + 1

            ' dump what's left of its energy at the current coordinates
                If TrackSecondaries Then

                    If NewSECoords.y <= ED_Halfwidth And NewSECoords.y >= -
                    ED_Halfwidth And NewSECoords.z > 0 And NewSECoords.z < Thickness
                    Then

                        If NewSECoords.x < PLOT_WIDTH / 2 And NewSECoords.x > -
                        PLOT_WIDTH / 2 Then 'fix the x dimensions at 0.5um in each
                        direction

                            If FSEnergy > 0 Then

                                EDArray(Round(NewSECoords.x / UNIT_CONVERT) +
                               EDArrayX / 2, Round(NewSECoords.z / UNIT_CONVERT)) =
                               EDArray(Round(NewSECoords.x / UNIT_CONVERT) + EDArrayX
                               / 2, Round(NewSECoords.z / UNIT_CONVERT)) + FSEnergy
```

```
                            End If
                        End If
                    End If
                End If

                Exit Do

            End If

            ' calculate the distance it travelled during this step and add it to the
               Bethe range
            ThisBetheRange = ThisBetheRange + NewSECoords.distance(OldSECoords)

            ' reset the coords and get new scatter angles

            Call OldSECoords.SetCoordinates(NewSECoords)
            Call OldSECosines.SetCoordinates(NewSECosines)
            sa1 = a1_a / FSEnergy
            scp = 1 - ((2 * sa1 * Rnd) / (1 + sa1 - Rnd))
            ssp = Sqr(1 - scp ^ 2)

        End If

    Loop

End If

' now that we're done with the secondary, calculate the inelastic scatter angles for the
' primary that started all this.
SP = (2 * epsilon) / (2 + (PrimaryEnergy / 511) - (PrimaryEnergy * epsilon / 511))
cp = Sqr(1 - SP)
SP = Sqr(SP)
ga = TWO_PI * Rnd

' Go back to tracking the primary, returning the primary's new energy.
FSETrack = loss

End Function

Private Function getFSEMFP(Energy As Double) As Double

    ' get the mean free path of a FSE. We could measure inelastic collisions
    ' of the FSE and follow tertiary electrons and stuff but that's kind of a mess
    ' and probably doesn't affect the total deposited energy much.
    ' We're only going to use the elastic MFP here


    ' Rutherford cross-section used here, same as for elastic primary scattering
    Dim QK, QL, QG As Double

    QL = AtomicNumber ^ 0.67 * (0.0034 / Energy)
    QK = QL * (1 + QL)
    QG = (AtomicNumber ^ 2) * 9842.7 / (Energy ^ 2 * QK)

    ' calculate the MFP using the cross-section
    getFSEMFP = (AtomicWeight * 100000000#) / (Density * QG)

End Function
```

References

[1] G.E. Moore, "Cramming more components onto integrated circuits," Electronics **38** (8) (1965).

[2] H.N.G. King, "Electron beam lithography," Microelectronics **1** (1), 28-30 (1967).

[3] R.F.M. Thornley and T. Sun, "Electron Beam Exposure of Photoresists," J. Electrochem. Soc. **112** (1965).

[4] R.D. Heidenreich, L.F. Thompson, E.D. Feit et al., "Fundamental aspects of electron beam lithography. I. Depth-dose response of polymeric electron beam resists," J. Appl. Phys **44** (9), 4039-4047 (1973).

[5] L.F. Thompson, E.D. Feit, C.M. Melliar-Smith et al., "Fundamental aspects of electron beam lithography. II. Low-voltage exposure of negative resists," J. Appl. Phys **44** (9), 4048-4051 (1973).

[6] R.J. Hawryluk and H.I. Smith, presented at the Electron and Ion Beam Science and Technology 5th Annual Conference, Houston, TX, 1972 (unpublished).

[7] R.F. Herzog, J.S. Greeneich, T.E. Everhart et al., "Computer-Controlled Resist Exposure in a Scanning Electron Microscope," IEEE Transations on Electron Devices **19** (5), 635-641 (1971).

[8] S. Miyuauchi, K. Tanaka, and J.C. Russ, "Automatic Pattern Positioning of a Scanning Electron Microscope," IEEE Transations on Electron Devices **17**, 450-457 (1970).

[9] H.Y. Ku and L.C. Scala, "Polymeric Electron Beam Resists," J. Electrochem. Soc. **116** (7), 980 (1969).

[10] I. Haller, M. Hatzakis, and R. Srinivasan, "High Resolution Positive Resists for Electron Beam Exposure," IBM. J. Res. Develop. **12**, 251-256 (1969).

[11] W. Chen and H. Ahmed, "Fabrication of sub-10-nm structures by liftoff and by etching after electron beam exposure of poly(methylmethacrylate) resist on solid substrates," J. vac. Sci. Technol. B **11** (6), 2519-2523 (1993).

[12] B. Cord, J. Lutkenhaus, and K.K. Berggren, "Optimal Temperature for Development of PMMA," J. Vac. Sci. Technol. B **(in review)** (2008).

[13] A.E. Grigorescu, M.C. van der Krogt, and C.W. Hagen, "Sub-10-nm structures written in ultrathin HSQ resist layers using electron-beam lithography," Proc. SPIE **6519**, 65194A (2007).

[14] J.K.W. Yang and K.K. Berggren, "Using high-contrast salty development of hydrogen silsesquioxane for sub-10-nm half-pitch lithography," J. Vac. Sci. Technol. B **25** (6), 2025-2029 (2007).

[15] W. Hu, K. Sarveswaran, M. Lieberman et al., "Sub-10-nm electron beam lithography using cold development of poly(methymethacrylate)," J. Vac. Sci. Technol. B **22** (4), 1711-1716
(2004).

[16] F. Lehmann, G. Richter, T. Borzenko et al., "Fabrication of sub-10-nm Au-Pd structures using 30 KeV electron beam lithography and liftoff," Microelectronic Eng. **65**, 327-333 (2003).

[17] T.H. Newman, R.F.W. Pease, and W. DeVore, "Dot matrix electron beam lithography," J. Vac. Sci. Technol. B **1** (4), 999-1002 (1983).

[18] R.F.W. Pease, "Electron beam lithography," Contemporary Physics **22** (3), 265-290 (1981).

[19] L.H. Lin and H.L. Beauchamp, "High speed beam deflection and blanking for electron lithography," J. Vac. Sci. Technol. **10** (6), 987-990 (1973).

[20] B. Cord, J. Yang, D.C. Joy et al., "Optimum Exposure Parameters for High-Resolution Electron Beam Lithography," Appl. Phys. Lett. **in review** (2008).

[21] J.S. Greeneich and T. Van Duzer, "Model for Exposure of Electron Sensitive Resists," J. Vac. Sci. Technol. **10** (6), 1056-1059 (1973).

[22] J.S. Greeneich and T. Van Duzer, "An exposure model for electron-sensitive resists," IEEE Transations on Electron Devices **ED-21** (5), 286-299 (1974).

[23] R.J. Hawryluk, H.I. Smith, and A.M. Hawryluk, "Energy dissipation in a thin polymer film by electron beam scattering," J. Appl. Phys **45** (6), 2551-2566 (1974).

[24] A. Uhl, J. Bendig, J. Leistner et al., "E-beam and deep UV exposure of PMMA based resists - identical or different chemical behavior?" SPIE **3333**, 1452-1457 (1998).

[25] J.S. Greeneich, "Developer characteristics of poly(methylmethacrylate) electron resist," J. Electrochem. Soc. **122** (7), 970-976 (1975).

[26] J.S. Greeneich, "Solubility rate of poly(methylmethacrylate), PMMA, electron-resist," J. Electrochem. Soc. **121** (12), 1669-1671 (1974).

[27] M. Aktary, M. Stepanova, and S.K. Dew, "Simulation of the spatial distribution and molecular weight of poly(methylmethacrylate) fragments in electron beam lithography exposures," J. Vac. Sci. Technol. B **24** (2), 768-779 (2006).

[28] A. Uhl, J. Bendig, J. Leistner et al., "Nonstatistical degradation and development characteristics of poly(methylmethacrylate) based resists during electron beam exposure," J. Vac. Sci. Technol. B **16** (6), 2968-2973 (1998).

[29] M. Khoury and D.K. Ferry, "Effect of molecular weight on poly(methylmethacrylate) resolution," J. Vac. Sci. Technol. B **14** (1), 75-79 (1996).

[30] G.H. Bernstein, D.A. Hill, and W. Liu, "New high-contrast developers for poly(methylmethacrylate) resist," J. Appl. Phys. **71** (8), 4066-4075 (1992).

[31] S.A. Rishton, S.P. Beaumont, and C.D.W. Wilkinson, presented at the 10th Electron and Ion Beam Sci. Technol. Conf., Montreal, 1982 (unpublished).

[32] A.N. Broers, "Resolution limits of PMMA resist for exposure with 50 KeV electrons," J. Electrochem. Soc. **128** (1), 166-170 (1981).

[33] R.A. Harris, "Polymethyl methacrylate as an electron sensitive resist," J. Electrochem. Soc. **120** (2), 270-274 (1973).

[34] M. Bolorizadeh and D.C. Joy, "Effects of Fast Secondary Electrons to Low-Voltage Electron Beam Lithography," J. Micro/Nanolith. MEMS **6** (2) (2007).

[35] Erik H. Anderson, Dierdre L. Olynick, Weilun Chao et al., "Influence of Sub-100 nm Scattering on High-Energy Electron Beam Lithography," J. Vac. Sci. Technol. B **19** (6), 2504-2507 (2001).

[36] B. Wu and A.R. Neureuther, "Energy deposition and transfer in electron-beam lithography," J. Vac. Sci. Technol. B **19** (6), 2508u-2511 (2001).

[37] J.S. Greeneich, "Impact of electron scattering on linewidth control in electron-beam lithography," J. Vac. Sci. Technol. **16** (6), 1749-1753 (1979).

[38] T.H.P. Chang, "Proximity effect in electron-beam lithography," J. Vac. Sci. Technol. **12** (6), 1271-1275 (1975).

[39] R.J. Hawryluk, H.I. Smith, A. Soares et al., "Energy dissipation in a thin polymer film by electron beam scattering: Experiment," J. Appl. Phys **46** (6), 2528-2537 (1975).

[40] R.J. Hawryluk, A. Soares, H.I. Smith et al., "Experimental evaluation of electron scattering models," J. Electrochem. Soc. **121** (3), 106C (1974).

[41] R.E. Jewett, T. Van Duzer, and J.S. Greeneich, "Electron-resist exposure contours for various patterns," J. Electrochem. Soc. **121** (3), 107C (1974).

[42] A.N. Broers, "Resolution limits for electron-beam lithography," IBM. J. Res. Develop. **32** (4), 502-513 (1988).

[43] D.C. Joy, "The spatial resolution limit of electron lithography," Microelectron. Eng. **1**, 103-119 (1983).

[44] (ASTM International, 2004), Vol. E986-04.

[45] F.S. Bates and G.H. Fredrickson, "Block copolymer thermodynamics - theory and experiment," Ann. Rev. Phys. Chem. **41**, 525-557 (1990).

[46] C.T. Black, R. Ruiz, G. Breyta et al., "Polymer self-assembly in semiconductor microelectronics," IBM. J. Res. Develop. **51** (5), 605-633 (2007).

[47] S.B. Darling, "Directing the self-assembly of block copolymers," Progr. Poly. Sci. **32** (10), 1152-1204 (2007).

[48] J.K.W. Yang, "Superconducting nanowire single-photon detectors and sub-10-nm lithography," Massachusetts Institute of Technology, 2009.

[49] D.J. Norris, A.L. Efros, M. Rosen et al., "Size dependence of exciton fine structure in CdSe quantum dots," Phys. Rev. B **53**, 16347-16355 (1996).

[50] B. Cord, C. Dames, J. Aumentado et al., "Robust Shadow-Mask Evaporation via Lithographically-Controlled Undercut," J. Vac. Sci. Technol. B **24** (6), 3139-3143 (2006).

[51] M.J. Rooks, E. Kratschmer, R. Viswanathan et al., "Low stress development of poly(methylmethacrylate) for high aspect ratio structures," J. Vac. Sci. Technol. B **20** (6), 2937 (2002).

[52] J.K.W. Yang and K.K. Berggren, "Using high-contrast salty development of HSQ for sub-10-nm half-pitch lithography," J. Vac. Sci. Technol. B **25** (6), 2025-2029 (2007).

[53] L.E. Ocola and A. Stein, "Effect of cold development on improvement in electron-beam nanopatterning resolution and line roughness," J. Vac. Sci. Technol. B **24** (6), 3061-3065 (2006).

[54] F.J. Pantenburg, S. Achenbach, and J. Mohr, "Influence of developer temperature and resist material on the structure quality in deep x-ray lithography," J. Vac. Sci. Technol. B **16** (6), 3547-3551 (1998).

[55] P.J. Flory, *Principles of Polymer Chemistry*. (Cornell University Press, Utica, NY, 1953), p.688.

[56] R.J. Hawryluk, "Exposure and Development Models Used in Electron Beam Lithography," J. Vac. Sci. Technol. **19** (1), 1-17 (1981).

[57] S. Yasin, D.G. Hasko, M.N. Khalid et al., "Influence of polymer phase separation on roughness of resist features," J. Vac. Sci. Technol. B **22** (2), 574-578 (2004).

[58] J. Yang, Z. Sun, W. Jiang et al., "Statistical thermodynamics of polydisperse polymer systems
in the framework of lattice fluid model: Effect of molecular weight
and its distribution on the spinodal in polymer solution," J. Chem. Phys. **116** (13), 5892-5900 (2002).

[59] D.G. Hasko, S. Yasin, and A. Mumtaz, "Influence of developer and development conditions on the behavior of high
molecular weight electron beam resists," J. Vac. Sci. Technol. B **18** (6), 3441-3444 (2000).

[60] S. Borini, "Cross-linked PMMA on porous silicon: an effective nanomask for selective silicon etching," J. Electrochem. Soc. **152** (6), 482-486 (2005).

[61] W.H. Teh, C. Liang, M. Graham et al., "Cross-linked PMMA as a low-dimensional dielectric sacrificial layer," J. Microelectromechanical Sys. **12** (5), 641-648 (2003).

[62] A. Chapiro, *Radiation Chemistry of Polymeric Systems*, 1st ed. (Wiley, New York, 1962).

[63] P. Alexander, R.M. Black, and A. Charlesby, Proc. Royal Soc. (London) **A320**, 136 (1955).

[64] P. Alexander, A. Charlesby, and M. Ross, Proc. Royal Soc. (London) **A223**, 392 (1954).

[65] A.R. Shultz, P.I. Roth, and G.B. Rathmann, J. Polymer Sci. **22**, 495 (1956).

[66] A.A. Miller, E.J. Lawton, and J.S. Balwit, J. Polymer Sci. **17**, 141 (1954).

[67] A. Chapiro, J. Chem. Phys. **53**, 295 (1956).

[68] J.C. Bevington and A. Charlesby, presented at the International Symposium on Macromolecular Chemistry, Milan-Turin, 1954 (unpublished).

[69] E. Rutherford and J. Chadwick, "Scattering of alpha particles by atomic nuclei and the law of force," Philosophical Magazine **50**, 889-913 (1925).

[70] P. Hovington, D. Drouin, and R. Gauvin, "CASINO: A New Monte Carlo Code in C Language for Electron Beam Interaction," Scanning **19** (1), 1-14 (1997).

[71] G. Han, M. Khan, Y. Fang et al., "Comprehensive model of electron energy deposition," J. Vac. Sci. Technol. B **20** (6), 2666-2671 (2002).

[72] D.C. Joy, *Monte Carlo Modeling for Electron Microscopy and Microanalysis.* (Oxford University Press, New York, 1995).

[73] H.A. Bethe, "Theory of Passage of Swift Corpuscular Bodies Through Matter," Annalen der Physik **5** (10), 325-400 (1930).

[74] D.C. Joy and S. Luo, "An empirical stopping power relationship for low-energy electrons," Scanning **11**, 176-180 (1989).

[75] R.L. Myklebust, D.E. Newbury, and H. Yakowitz, Report No. 460, 1976.

[76] H.E. Bishop, Report No. 460, 1976.

[77] R.D. Evans, *The Atomic Nucleus.* (McGraw-Hill, New York, 1955).

[78] C. Stebler, M. Despont, U. Staufer et al., "Microcolumn based low energy e-beam writing," Microelectron. Eng. **30** (1-4), 45-48 (1996).

[79] K.J. Polasko, Y.W. Yau, and R.F.W. Pease, "Low energy electron beam lithography," Proc. SPIE **333**, 76-82 (1982).

[80] C.W. Lo, M.J. Rooks, W.K. Lo et al., "Resists and processes for 1 kV electron beam microcolumn lithography," J. Vac. Sci. Technol. B **13** (3), 812-820 (1983).

[81] F.P. Incropera and D.P. DeWitt, *Fundamentals of Heat and Mass Transfer*, 5th ed. (Wiley, 2002).

[82] Y.F. Chen, H.F. Yang, and Z. Cui, "Effects of developing conditions on the contrast and sensitivity of hydrogen silsesquioxane," Microelectron. Eng. **83**, 1119-1123 (2006).

[83] G.J. Dolan, "Offset Masks for Lift-Off Photoprocessing," Appl. Phys. Lett. **31** (5), 337-339 (1977).

[84] L.E.M deGroot, K.L. Hagemans, J. Kortlandt et al., presented at the Microcircuit Engineering 84, Berlin, West Germany, 1985 (unpublished).

[85] H. Scherer, A.B. Zorin, and J. Niemeyer, "Single-Charge Devices with Ultrasmall Nb/AlOx/Nb Trilayer Josephson Junctions," J. Appl. Phys. **97** (5), 54501 (2005).

[86] Yifang Chen, Kaiwu Peng, and Zheng Cui, "A Lift-Off Process for High-Resolution Patterns Using PMMA/LOR Resist Stack," Microelectronic Eng. **73-74**, 278-281 (2004).

[87] G.J. Dolan and J.H. Dunsmuir, "Very small (<20 nm) lithographic wires, dots, rings, and tunnel junctions," Physica B **152** (1-2), 7-13 (1988).

[88] P. Joyez, "The single cooper-pair transistor: a macroscopic quantum system," University of Paris, 1995.

[89] L.E. Ocola and A. Stein, "From microchannels to nanochannels in a bilayer resist," Proc. SPIE **5592**, 421-426 (2005).

[90] L.E. Ocola, D.M. Tennant, and P.D. Ye, "Bilayer process for T-gates and sigma-gates using 100 kV e-beam lithography," Microelectron. Eng. **67-68**, 104-108 (2003).

[91] T. Wada, S. Haraichi, K. Ishii et al., "SiO2/poly-Si electron beam resist process for nanofabrication," J. Vac. Sci. Technol. A **14** (3), 1850-1854 (1996).

[92] A. Potts, G.J. Parker, J.J. Baumberg et al., "CMOS-compatible fabrication methods for submicron josepshon junctions," IEEE Proc. Sci. Meas. Technol. **148** (5), 225-228 (2001).

[93] A. Potts, P.R. Routley, G.J. Parker et al., "Novel fabrication methods for submicrometer josephson junction qubits," Journal of Materials Science: Materials in Electronics **12**, 289-293 (2001).

[94] D. Berman, "Ph.D Thesis," Massachusetts Institute of Technology, 1998.